UNIVERSITÁ DEGLI STUDI DI BERGAMO
Dipartimento di Ingegneria e Scienze Applicate

DOTTORATO DI RICERCA
IN
TECNOLOGIE PER L'ENERGIA E L'AMBIENTE

XXVIII ciclo

Anno 2016

DESIGN OF PULSATING HEAT PIPES

A novel non-equilibrium lumped parameter model for transient gravity levels

Doctoral thesis:
Miriam Manzoni

Supervisor:
Prof. Marco Marengo

Science is the sum of a great multitude of mysteries.

It is an unending argument between a great multitude of voices.

Dyson J. Freeman

Abstract

As relatively new and promising members of the wickless heat pipe family, Pulsating Heat Pipes (PHPs), with high effective thermal conductivity and construction simplicity, may answer to the present industrial demand of efficient thermal control, flexibility and low costs. In the last twenty years, many experimental and numerical works focused on PHPs, but despite the great efforts, their non linear, two-phase, internal flow remains essentially an unknown and, thus, none of the existing models is actually able to simulate it.

One of the most important unsolved questions regards the influence that gravity may have on the device thermal-hydraulic behavior. Literature, indeed, reports very poor and contradictory data, even if modified gravity conditions arise in various applications from automotive to aerospace, from chemistry to material synthesis. This work aims to fill this serious lack of knowledge. Thus, a capillary, closed loop PHP made of a copper tube bended into 32 parallel channels and filled with FC-72 has been investigated both on the ESA

ESTEC Large Diameter Centrifuge (ESA Educational project Spin Your Thesis! 2013), and on board of the ESA-NoveSpace Airbus A300 Zero-G flying parabolic trajectories (58th and 59th ESA Parabolic Flight Campaigns). For the first time, a planar PHP with circular cross section channels, equipped with 14 thermocouples and a pressure transducer has been fully, thermally characterized in several operative conditions from 0.01g to 20g.

In addition, in order to provide a numerical tool able to help and support the experimental research in enlarging the present knowhow and spreading PHPs industrial application, the results of these experimental campaigns have been used to develop and validate a novel lumped parameters model. It uses an advanced numerical technique to allow fast simulations, extending sensitivity analysis and device designs. Lumped parameter models are not a novelty for PHPs per se: however, for the first time this kind of numerical tools has been applied to simulate transient operative conditions removing physical simplified assumptions and embedding directly phase changes processes. The resulting code showed very good prediction capability, being able to reproduce with high accuracy the experimental recorded data both in steady and transient conditions.

KEY WORDS: Pulsating Heat Pipe, hyper-gravity, micro-gravity, lumped parameter model, transient and steady simulations.

Contents

Abstract

Contents

Contents

Chapter 1

1. Introduction: Pulsating Heat Pipes a novel technology

Heat transfer systems are somewhat ubiquitous: they can be found in electronic devices, energy management components, in transportation, cooling and in households in general. In the last decades, the more and more stringent demand for higher performances, efficient thermal control and low costs has pushed researchers to develop a new generation of two-phase flow systems, mainly based on the phase change of a working fluid. The latent heat

associated to this phenomenon is indeed a very efficient mean of absorbing or releasing heat, counting on very high heat transfer coefficients and associated small temperature differences. However, numerous related physical intertwined mechanisms regulate the operations of such devices; therefore the development of yet higher performance, though reliable systems, calls for a thorough understanding on fundamental principles and their modeling to support new designs.

An every-day life example of the need for improving heat transfer efficiency is the more and more stringent request of effective and reliable heat removal from electronic components. In the past decades, indeed, the net thermal power output per surface unit of a chip has reached limits which cannot be satisfied using sensible heat only. In order to maximize performances, assure reliability and prevent premature failures, a precise temperature and temperature gradient control is requested: uneven heat flux distributions on the chip surface, indeed, may lead to the appearance of hot spots which, in turn, may deteriorate, or worst damage, the chip itself. A heat transfer system, able to satisfy micro-electronics requests, can also be useful in various other micro-scale problems such as laser diodes, photovoltaic cells, infrared detectors or nonsurgical treatment of cancerous tissue in order to level the temperature of critical elements. In the area of space applications, on the other hand, with the increasing size of space platforms and satellites or for future exploration missions, big amounts of heat need to be dissipated or collected by large space radiators; moreover, efficient thermal control in space and reduction of moving mechanical elements become of crucial importance in order to increase devices lifetime and simplicity. Two-phase closed loop systems can meet all these requirements.

As a matter of fact, complex two phase devices, such as sintered heat pipes and loop heat pipes, are already successfully implemented in many ground and space applications. However the principal drawback of such systems is the high production costs. In order to surpass this inconvenience, in the past decades, novel, two-phase passive systems without wick structure, like Pulsating Heat Pipes (PHPs), have been developed and, at the present, such technologies already play an important role in a variety of engineering fields. PHPs, for example, can be found in thermal management (electronics cooling, polymeric heat exchangers), heat recovery (thermal solar panels, hybrid TPV panels), and cooling of engines and batteries in automotive and aerospace applications. However, they still suffer a degree of criticism, because of the too narrow working regimes, difficult specific/custom designs or the not yet known dependence on gravity, operational and constructive parameters (e.g. diameter, filling ratio, working fluid properties, number of turns, condenser/evaporator extension, inclination, etc.) [1].

1.1 Pulsating Heat Pipes

Patented in its most common assessment by Akachi [2] [3] in the early '90, a closed loop PHP[1] usually consists of a meandering, capillary tube closed end-to-end, evacuated and partially filled with a working fluid, which results as an alternation of vapor bubbles and liquid slugs (Figure 1.1). Even if many different flow paths have been observed during PHPs operation (e.g. anular, semi-anular, stratified) [4], confined slug flow is the most common. The device performance and operation primarily depend on the continuous maintenance of non-equilibrium conditions within the system [5] [6] which means

---

[1] Another layout of PHPs actually exists: the open loop PHP which ends are not connected to each other. However, this thesis will focus only on closed loop PHPs.

that a PHP can be described only considering local different thermodynamic states associated to different physical zones.
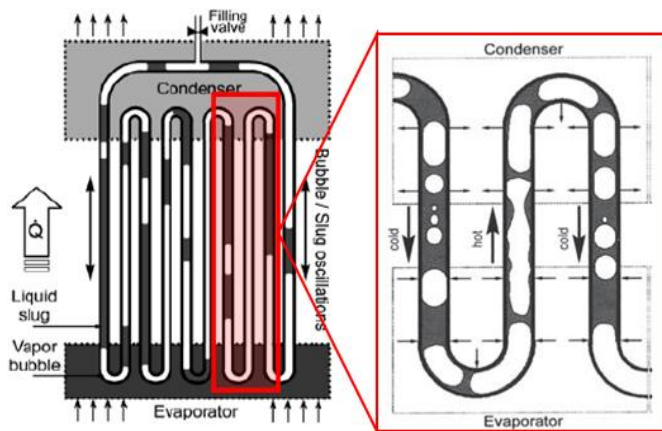
Figure 1.1: Basic scheme of a closed loop PHP; on the right, zoom of the internal flow patterns.

When heat power is provided to the evaporator section, the thin liquid film, which surrounds each vapor plug, evaporates; bubbles expand and try to reach higher pressures and temperatures as well as larger qualities (Figure 1.2 point A → point B). By this process, vapor pushes the adjacent fluid towards the condenser zone. There heat is rejected to a cold source and condensation occurs within the vapor plugs nearby the wall surface forcing point A to reach point C at a lower pressures, temperatures as well as smaller qualities.

This is the principal mechanism[2] which promotes fluidic motion within the channel: liquid and vapor both oscillate and circulate driven by pressure disequilibrium and phase change phenomena (film evaporation, flow boiling, film condensation), but also capillary forces and gravity still play an important role. Besides, the global

---

[2] The system is thermally driven, which means that there is no need of external mechanical/electrical power.

thermal hydraulic behavior of a PHP strictly depends on all these intertwined factors.
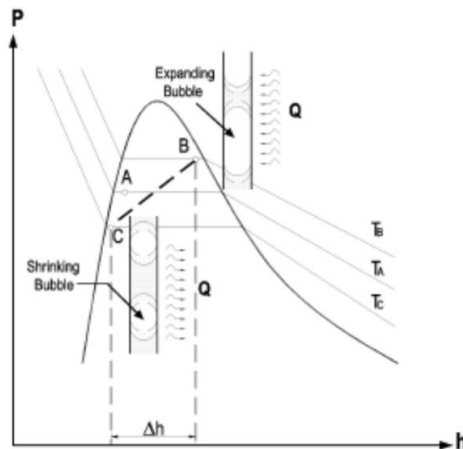
Figure 1.2: Pressure vs. enthalpy diagram of a working fluid control volume in non equilibrium conditions [5].

Contrary to other types of heat pipes, PHPs fluid motion is inherently non-stationary and, in some occasions, chaotic, thus more difficult to understand and to model. Up to now, there are scarce means to reliably predict PHPs performance; even if in the last years advances have been made, numerous fundamental problems are still need to be solved to predict the overall heat transfer, start-up criteria and functioning limits.

1.1.1 PHPs vs. classical heat transfer systems

In order to understand the real potential of PHPs with respect other classical heat transfer systems which do not account on external pumps[3], like conductive solid materials, a comparison

---

[3] In order to compare to systems which use mechanical or electrical pumps, one should consider also costs, masses and complexities associated to these additional apparatus.

exercise may be worthwhile; for a given power and geometrical dimension one can compare, for example, the temperature difference between the evaporator and the condenser zone assuming equal heat transfer with the external environment for all the systems.

Let's take a lab-scale, planar, copper PHP 190x200mm bended in 32 parallel channels of 2.0/1.1mm external/internal diameter and filled with 50% volumetric filling ratio of FC-72. The equivalent axial thermal resistance associated to such a device is, on average, of about 0.6K/W, which means that the temperature difference between the evaporator and the condenser zone is of about 30K if 50W are provided at the evaporator section[4].

On the other hand, a block of solid copper with the same dimensions (190x200x2mm) transfers 50W with an axial thermal resistance of $\frac{0.2}{390\times0.19\times0.002}$ K/W $= \sim1.4$K/W corresponding to a temperature difference of about 70K which means 2.5 times the temperature gap achieved with the equivalent lab-scale PHP.

In addition one should consider the weights of the two apparatus: if the PHP has an equivalent specific mass of 1700kg/m^3, the copper block has a density of 8900kg/m^3, 5 times higher! Thus the choice of PHPs is beneficial for all the applications which require large, weightless and passive devices, such as aerospace systems.

PHPs are also a promising alternative to standard sintered heat pipes and two-phase systems, such as thermosyphons or grooved heat pipes. Such technologies, however, differently from PHPs have already reach TRL 9 (Technological Readiness Level), which means that the systems have already been tested in operational environments; PHPs are TRL 3 meaning that, up to now, there are only experimental proofs of concept. A comparison between the different devices is shown in Table 1.1.

---

[4] Much lower resistances can be achieved with real PHPs as shown in Table 1.1.

	Sintered Heat Pipes	PHPs	Grooved Heat Pipes	Thermosyphons
Radial heat flux	Very high: up to $250W/cm^2$	Medium: up to $30W/cm^2$	Medium: up to $20W/cm^2$	High: up to $100W/cm^2$
Axial heat flux	High: up to $600W/cm^2$	High: up to $1200W/cm^2$	High: up to $200W/cm^2$	-
Total power	Medium: up to 200W per unit	High: up to 5000W	Medium-high: up to 600W per unit	High: up to 10kW per unit
Thermal resistance	Very low: <0.01K/W	Very low: <0.02K/W	Very low: <0.01K/W	Very low: <0.01K/W
Equivalent thermal conductivity	Very high: up to 40kW/(mK)	Medium: up to 10W/(m K)	Very high: up to 200kW/(mK)	Very high: up to 200kW/(mK)
Start-up time	Fast: few seconds	Medium: 2-3 minutes	Fast: few seconds	Medium: 2-3 minutes
Effect of inclination angle	Medium: sintered HPs suffer in top heating mode. Efficient in bottom heating mode	Critical: a proper design may avoid strong effects, but top heating mode is difficult	Critical: a proper design may avoid strong effects, but top heating mode is difficult	Critical: evaporator above, only for complex systems (e.g. valves or active control)
3D space adaptability	Low	High (highly foldable)	Medium (flexible bended)	Medium/high (gravity limit)
Thermally controlled surface	Medium	Large	Medium	High
Cost	Medium (wick structure)	Low (capillary tube)	Low (extrusion)	Low/Medium

Table 1.1: Standard heat pipe vs. wickless heat pipes.

7

1.2 Motivations and thesis layout

PHPs represent the last frontier of the two-phase passive heat transfer devices and could be a new alternative to cooling systems in the near future. The unique features of such devices, like the construction simplicity, low costs, high thermal flux capacity and the self-driven heat exchange, could make such technology suitable for future thermal control systems.

In addition, due to the low specific weight, PHPs could be the preferable candidates for the thermal management during planetary exploration or for applications in micro-gravity environments (e.g. ultra-light folding radiator panels).

However, in order to spread their industrial applications, many questions need to be answered and the complex thermo-fluid dynamics governing PHPs internal two-phase oscillating flow need to be fully understood. In this prospective, numerical analyses appear essential to help and support the experimental research. Thus, the aim of this thesis is the development of a robust, but simple numerical model able to simulate the dynamic as well as the global thermal performance of a closed loop PHP in both transient and quasi-steady state operations. In addition, since the effect of gravity on PHPs has never been studied in detail, modified-gravity experiments will be performed in several operative conditions to fully thermally characterize a PHP from micro to hyper-gravity. The results of these analyses will be accounted for in the modeling phase and will represent a step forward in the present knowhow, solving a still open crucial issue especially if one considers the fact that PHPs are favorite candidates for aerospace applications. In addition, the resulting validated model can be useful to study the dependence of PHPs thermal-hydraulic behavior on several constructive and

operative parameters, as well as it can be applied to investigate novel and breakthrough methods to enhance the present achievable thermal performance.

Having these goals in mind, the thesis layout will be the following:

- *Chapter 2. PHP in modified gravity: state of the art*, a review of the experimental studies already performed in micro and hyper-gravity conditions;
- *Chapter 3. PHP in hyper-gravity: ESA Large Diameter Centrifuge*, a report of the results of the experimental campaign performed in augmented-gravity conditions;
- *Chapter 4. PHP in micro-gravity: ESA parabolic flight campaigns*, a report of the results of the experimental analyses performed in reduced-gravity conditions;
- *Chapter 5. Numerical modelling of PHPs: state of the art*, a review of the numerical studies performed on PHPs in the last 20 years;
- *Chapter 6. A novel lumped parameter numerical model*, where the developed, innovative, mathematical model will be presented and explained;
- *Chapter 7. Numerical model validation*, a comparison between the numerical and experimental results obtained during the previous experimental campaigns;
- *Chapter 8. Sensitivity analysis: influence of the tube features*, a report of the results achieved by means of several simulations performed changing PHPs constructive and operative parameters;
- *Chapter 9. Conclusions and future works*, where the principal results of the entire work will be summarized and possible improvements will be proposed.

PART I

EXPERIMENTAL ASSESSMENT

Chapter 2

2. PHP in modified gravity: state of the art

The physical phenomena related to heat and mass transfer are greatly affected by gravitational conditions.

The inner fluidynamics of PHPs mainly depends on the interplay between phase changes, capillary forces and gravity. Being somewhat a recent technology, however, very few studies were devoted to methodologically test PHPs in modified gravity (see Table 2.1); beside, the conclusions are contradictory and cannot be generalized.

Principal Investigator	Year	Experimental or Numerical?	Adopted Facility	PHP Layout	Conclusions
BEFORE EXPERIMENTS PROPOSED in CHAPTER 3 and 4					
Kiseev et al. [7]	1999	Experimental	Centrifuge	Non-looped PHP	Applied accelerations influence pressure and temperature trends. Hyper-gravity worsens the PHP performance only for anti-gravity configuration.
Delil [8]	1999	Theoretical	-	-	Scaling of two-phase devices from normal to micro-gravity is complicated and only distorted scaling offers some possibilities, when not the entire loop but only sections are involved.
Delil [9] [10]	2000	Theoretical	-	-	Scaling of two-phase devices from normal to micro or hyper-gravity is complicated and only distorted scaling offers some possibilities.
van Es et al. [11]	2000	Experimental	Centrifuge	3D Flat Swinging Heat Pipe	Different prototypes show increasing or constant evaporator temperatures when tested in hyper-gravity.
Delil [12]	2001	Theoretical	-	-	Basing on the developed scaling model, the author proposed, but did not build, a test rig for modified gravity experiments.

continue

Kawaji [13]	2003	Experimental	Parabolic Flight	One straight and one bended PHP	All the configurations tested, especially the top heating mode PHPs, show better operating characteristics and improved heat transfer under reduced gravity.
Gu et al. [14]	2004	Experimental	Parabolic Flight	One straight and one bended PHP	All the configurations tested for both the heat pipes show better operating characteristics and improved heat transfer under reduced gravity than under normal or hyper-gravity.
Gu et al. [15]	2005	Experimental	Parabolic Flight	Transparent Bottom Heated Mode PHP + One straight and one bended PHP	Steady pulsating flows could be achieved under reduced gravity, while hyper-gravity weakens the pulsating motion. Best performance of the tested devices under micro-gravity.
de Paiva et al. [16]	2010	Experimental	Sounding rocket	PHP	The test rig has been built and tested in normal gravity. Sounding rocket has been postponed.
Maeda et al. [17]	2011	Experimental	Satellite	3D PHP with check valves	The prototype has been build and tested in normal gravity. Experiments on satellite are scheduled.
Ma et al. [18] [19]	2011	Experimental	Centrifuge	3D Oscillating Heat Pipe	The performances of the device tested in top heating mode are quite independent on gravity levels.

continue

15

Mameli et al. [20]	2012	Numerical	-	PHP	Reduced gravity worsens the performance of the device. A horizontal PHP behaves as a PHP at 0g.
Ayel et al. [21]	2013	Experimental	Parabolic Flight	Transparent Flat Plate PHP	Dry out occurs during micro-gravity; an improvement of the thermal performance during hyper-gravity is assisted. Results suffered from leakage between parallel channels.
AFTER EXPERIMENTS PROPOSED in CHAPTER 3 and 4					
Ayel et al. [22]	2015	Experimental	Parabolic Flight	Flat Plate PHP	The device in vertical position is influenced by variations in the applied gravity field. Micro-gravity lowers the while performance of the device, even if the PHP continues working. No important effects are detected in horizontal position.
Mangini et al. [23]	2015	Experimental	Parabolic Flight	Non capillary PHP	In bottom heated mode, the device works as thermosyphon in normal and hyper-gravity conditions, as PHP in reduced gravity. No important effects are detected in horizontal position.

Table 2.1: Summary of the experimental or numerical works proposed on PHP in modified gravity conditions.

This chapter will provide an overview of the principal works in the field which review has yielded to the experiments described in Chapter 3 and 4. The two works proposed in 2015 (Ayel et al. [22] and Mangini et al. [23]) being more recent are not taken into account.

Note that information regarding PHPs in reduced gravity could also be achieved conducting experiments with inclined devices. However, even if the performance could be similar to the ones in reduced gravity (this still should be proved), the dynamic could be different being the body force still present even if the components along the fluidic paths is lowered. For example, a non capillary PHP, as the one tested by Mangini et al. [23], works on ground as thermosyphon independently on the chosen inclination because of the ratio between gravity, that is still present on a tilted device, and buoyancy; in reduced gravity environment, on the other hand, this device works as a PHP capable of slug and plug flow. Therefore, in the following experiments on inclined PHPs are not accounted for.

2.1 Parabolic flight experiments

Parabolic flights allow testing a device for few seconds in both micro and hyper-gravity conditions. The level of gravity sensed by the test rig depends on the plane characteristics and on the followed parabolic trajectory.

The first experiment on PHPs performed on board a parabolic flight date back to ten years ago. The results are described by Gu et al. in three different papers [13] [14] [15]. They tested two different aluminum prototypes of a flat plate PHP, one straight and one bended, on board of a Falcon 20 aircraft exposing the test rig to $\pm 0.02g$ in micro-gravity and 2.5g in hyper-gravity. Both the prototypes had rectangular cross section channels (1mm of hydraulic diameter) and were charged with R-114. The evaporator zone was

warmed up by electrical heaters, while the cooling section made use of air fans. Three different configurations have been tested as reported in Figure 2.1: two vertical antigravity (A and B) and one vertical gravity assisted (C)[5].
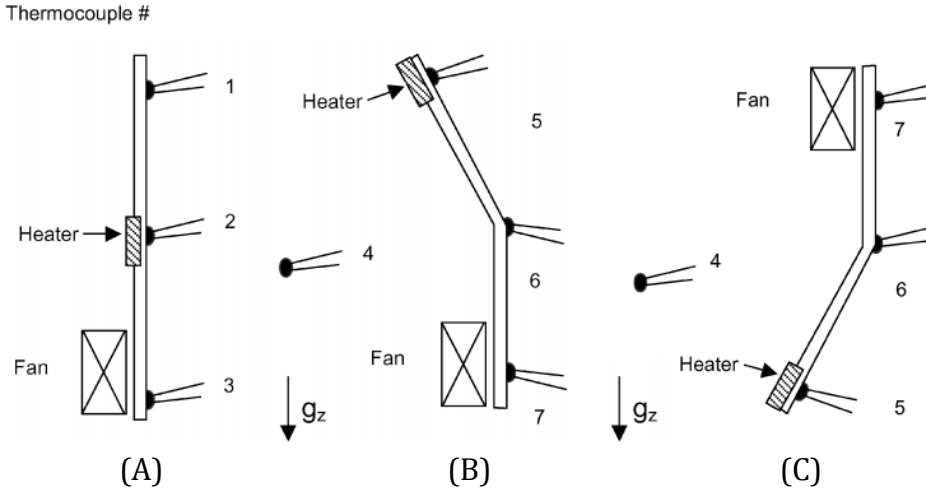

Figure 2.1: PHP configurations tested by Gu et al. [14] [15].

They concluded that under normal and hyper-gravity conditions, the orientation affected the PHP performance: the bottom heating case (C) yielded to smaller temperature difference between the evaporator and the condenser, followed by the middle heating (A) and, finally, the top heating cases (B). In addition, they observed that the placement of the evaporator section at the PHP bottom prevented unstable operations and temperature fluctuations because gravity helped the liquid motion. Under reduced gravity, instead, the authors stated that all the tested configurations showed better operating and heat transport performance than when under normal or hyper-gravity conditions. However, looking better at the temperature

---

[5] Antigravity means vertical top heated mode, gravity assisted means vertical bottom heated mode.

profiles reported in the papers, this is evident only for the antigravity cases, while the gravity assisted one does not show a sensible temperature reduction during the parabolas. In addition they analyzed the fluidic motion of slugs and plugs by means of a micro Teflon PHP (1.6mm internal diameter) filled with R-114 in vertical bottom heated mode position. They concluded that steady pulsating flows could be achieved under reduced gravity conditions, while hyper-gravity weakened the pulsating motion inducing working mechanisms of conventional thermosyphons. However, one should note that the chosen internal diameter overcame the capillary limit [24] when 2.5g are applied; thus, confined motion was not assure anymore.

Few years later, a new parabolic flight was performed by Ayel et al. [21] making use of the ESA Novespace A300 Zero-G testing a transparent flat plate PHP in gravity assisted configuration. The glass device, with a hydraulic diameter of 2mm, has been charged with water, heated up by means of electrical heaters and cooled using an external liquid circuit. The results of the work, unfortunately, are not conclusive since leakage between parallel channels affected the device operation. Nevertheless, the authors observed that micro-gravity was, generally, accompanied by dry-out phenomena at the evaporator section, while hyper-gravity helped the liquid to reflow in the hot zone rewetting the channel and, thus, bettering the thermal performance of the device. Note that an improved similar apparatus has been tested again in 2015 [22] yielding to much successful results.

2.2 Centrifugal experiments

Devoted experiments in hype-gravity conditions have usually been performed on large diameter centrifuges or centrifuge tables

taking advantage of the additional and controllable force produced by the rotational motion.

In 1999, Kiseev et al. [7] experimentally investigated the effects of accelerations and vibrations on the performance of a non-looped stainless steel PHP making use of a 4.5m diameter centrifuge table. The 23 turns device with an internal diameter of 1.1mm was charged with acetone and tested for inclinations of -90° (antigravity), 0°, and +90° (gravity assisted) with respect to the tangential direction. The so obtained data confirmed that the acceleration influences the pressure and the corresponding temperature trends: the PHP operated successfully by various accelerations and there was an increase in the evaporator temperature passing from 6g to -12g; dry-out was not observed. In addition, the performed tests have shown that PHPs are not sensitive for vibrations (frequency form 0 to 16kHz, amplitude from 0 to 7mm).

One year later, van Es et al. [11] tested, under hyper-gravity loads, a flat swinging PHP with two different working fluids: acetone and ethanol. The device was heated by powering dissipating elements and cooled with Peltier cells. The whole system has been placed on a rotating table with a radial distance to the rotational axis of approximately 50cm. According to the authors, several different experiments were performed, but only two of them are discussed in the published work: one with a stainless steel prototype using ethanol as working fluid; the other with an aluminum prototype using acetone as working fluid. The experiments were started at normal gravity and then the speed of the rotating table was increased until the oscillating behavior of the PHP breaks down. The recorded data of the device charged with ethanol showed an evaporator temperature first order increase to a stepwise boost in the acceleration level after few minutes of spinning at 4.4g. On the other hand, the prototype charged with acetone performed better: it was subjected to a high-g

test, where the acceleration has been increased up to 8.4g (limit of the rotating table). The maximum temperature difference between the evaporator and the condenser was approximately 22.5°C and it remained constant with the acceleration enhancement underlining a stable operation of the system for all the tested loads. Unfortunately, the authors did not report the actual orientation of the device on the rotational table (it can be guessed from the reported picture), thus further information can hardly been inferred from this work.

Finally, in 2011 Ma et al. [18] [19] investigated a miniature 3D flat plate oscillating heat pipe with non-favorable evaporator position from 0g (horizontal position) to 12g on a spin-table centrifuge (0.5m radius, 20g maximum acceleration). The chosen working fluid was acetone, while the tube, with a hydraulic diameter of 0.76mm, was manufactured from electronic-grade copper. The device has been heated up with electrical resistances, while the cooling process made use of a cooling bath. The experiments started in horizontal position (0g) and then in vertical top heated mode the gravitational level was enhanced by following steps corresponding to 1g, 5g and 10g. It was found that performances were near-independent on the investigated hyper-gravity loads: results showed that the thermal conductivity of the investigated device remained near independent on gravity and slightly increased at 10g. Clearly, these findings prove that a 3D device can operate in any orientation with respect to gravity and this demonstrate a robust thermal performance as previously suggested by Charoensawan et al. [25] .

2.3 Other experimental facilities: sub-orbital rockets and satellites.

There are other possibilities to performed experiments in modified gravity environment. Long term micro-gravity, for

examples, can be sensed on board of satellites, while minutes of it can be reproduced on suborbital rockets. However, performing experiments on such kind of platforms is expensive, complicated, because of the high number of strictly technical requirements, and, unfortunately, some times the launch could be postponed resulting in a loss of time and resources. This was the case of the two works reviewed in this section.

In 2010 de Paiva et al. [16] proposed an experimental analysis of four two-phase technologies for the thermal management and heat dissipation of electronics in micro-gravity conditions. These devices (one mini heat pipe, one heat spreader, one copper/acetone PHP and one device based on phase change materials) showed, on ground, a thermal resistance small enough to make them possible candidates for electronic equipment heat management in normal, and hopefully, in reduced gravity. Unfortunately, the launch of the testing suborbital rocket which was scheduled for the same year, was postponed and therefore the results in micro-gravity are missing in the present paper. In addition, no further publications have been produced.

The following year, Maeda et al. [17] developed a flat plate oscillating heat pipe with check valves to be placed on a Small Demonstrate Satellite-4 (SDS-4) built by JAXA. The device, made of stainless steel and charged with HFC-134a, was thermally characterized on ground showing thermal conductivity 250-350 times higher than the wall material alone. They prepared the test rig to be place on the satellite and checked if the system was able to operate without problems under a micro-gravity environment. The launch was scheduled for the beginning of 2012, but no further publications can be found in literature.

2.4 Theoretical and numerical studies

Finally, few theoretical studies have been performed on PHPs in modified gravity. Even if they do not provide any further information are here reported for sake of completeness.

In four different works Delil [8] [9] [10] [12] discussed the thermal-gravitational scaling from micro to super-gravity conditions of two-phase heat transport systems for spacecraft applications and planetary exploration. The research was done for a better understanding of the impact of gravity on two-phase flow and heat transfer phenomena, to provide means for comparison and generalization of data, and to develop useful tools to design space-oriented two-phase systems and components based on the outcomes of terrestrial tests, saving money and reducing costs. He concluded that scaling of two-phase heat transport systems is very complicated; only distorted scaling offers some possibilities, when not the entire loop but only sections of it are involved. No comparison with experimental results was shown.

Mameli et al. [20] numerically studied the behavior a 9 turns PHP charged with ethanol and with a tube thermal conductivity of 400W/mK. A validated lumped parameter numerical model has been adopted and different heat fluxes have been provided at the evaporator region. They concluded that for all the tested cases, the reduction of gravity lowers the device efficiency; in addition it makes the best performance occurring at lower heat input. Finally, they reported that the temperature trends obtained by decreasing the gravity level are comparable to ones of a tilted PHP. However, they admitted that this should be confirmed experimentally.

Chapter 3

3. PHP in hyper-gravity: ESA Large Diameter Centrifuge

The experimental review reported in Chapter 2 has shown that methodological studies on PHPs under modified gravity conditions are still missing. The lack of a full range characterization with respect to hyper-gravity leads to a series of interesting questions: how hyper-gravity affects PHPs thermal hydraulic behaviour? Could hyper-gravity be beneficial for the PHPs performance and in what ranges? Is

it possible to develop a numerical model able to simulate a PHP under hyper-gravity conditions?

In order to answer to all these issues, experiments must be performed; thus a stable hyper-gravity field should be established.

One possible solution is the use of parabolic flights. During a parabolic manoeuvre, both micro and hyper-gravity conditions can, indeed, be experienced; however there are three important limitations:

1. the level of hyper-gravity is unstable, which leads to wide scatter of data;
2. a narrow range of hyper-gravity (1-1.8g) is available;
3. the hyper-gravity period is too short to reach steady state.

Another possible solution is the use of centrifuges with large diameters which provide the unique opportunity to perform long term experiments in a stable and controlled modified gravity environment.

3.1 The ESA Large Diameter Centrifuge

The experimental campaign in hyper-gravity conditions [26] [27] has been conducted making use of the European Space Agency (ESA) Large Diameter Centrifuge (LDC) of the ESA ESTEC center in Noordwijk (Figure 3.1) [28] [29]. This device allows reproducing extreme hyper-gravity fields, up to 20 times the normal conditions on Earth.

The LDC system comprehends four large rotating arms where swing gondolas can be located. The rotational movement of the arms and the gondolas creates an artificial acceleration field at the equipment positioned inside the gondolas. In order to achieve high levels of hyper-gravity, the rotational speed or the arm length should be sufficiently elevated. However, the LDC represents a rotational

reference frame and in these cases the Coriolis forces are present and must be taken into account. In order to keep the Coriolis acceleration small enough, the use of high arms length instead of high rotational speed is desired. Thus, the LDC has a maximum of 4m radius distance, which is enough to consider the Coriolis force as a secondary effect, with less than 0.05% perturbation in comparison with the centripetal acceleration produced.

In addition, the system has been designed to limit any possible vibration although these are inherent to all the rotating devices.

Figure 3.1: ESA LDC: rotating arms and gondolas.

The ESA LDC can accommodate a maximum of six gondolas per run: each gondola has a free volume of 60x60x80cm and a maximum capacity of 80kg. The gondola are passive swing out system; thus during the LDC run they orient such that the gravity vector is perpendicular to their floor. Several utilities are available on the gondolas, such as communication lines based on various protocols or temperature and gravity sensors.

3.2 The experimental apparatus

The geometrical characteristics of the PHP tested on the ESA LDC are briefly described in Figure 3.2.

The basic PHP structure consists of a copper tube with an internal diameter of 1.1mm and an external diameter of 2.0mm. It is folded so as to obtain thirty-two parallel channels and sixteen U-bends in the evaporator zone; finally it is closed end to end by means of two T-joints tin soldered.

While evacuating the PHP by means of an ultra-high vacuum system (Varian® DS42 and TV81-T) down to 0.3mPa, the working fluid, FC-72, is degassed in a secondary loop by continuous boiling and vacuuming cycles. Finally the PHP is filled with a volumetric ratio 0.50 ± 0.03 and permanently sealed by means of tin soldering. The incondensable gas content, less than 6PPM, is estimated by measuring the difference between the actual fluid pressure inside the PHP and its saturation pressure at environmental temperature [30].
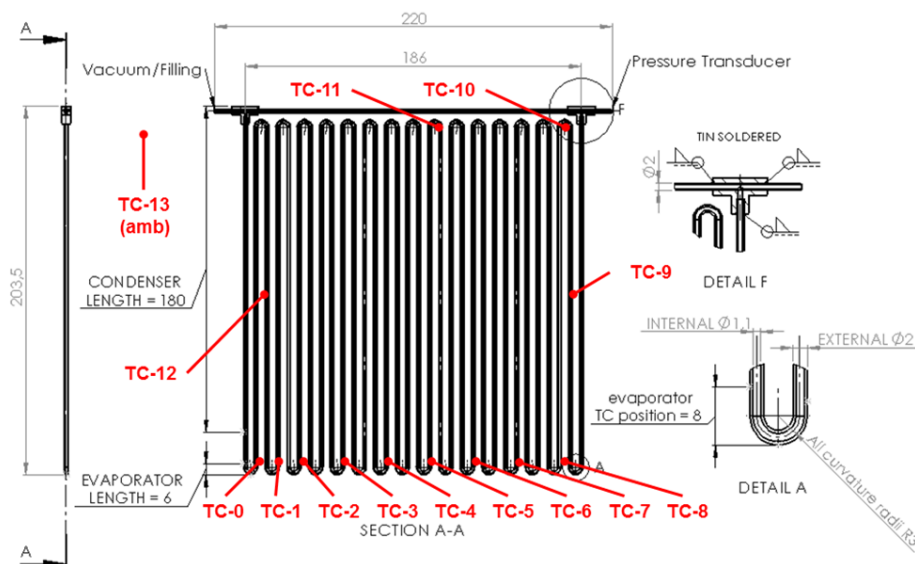
Figure 3.2: Technical sketch of the PHP.

The PHP heater consists of four electric resistors connected in parallel (Thermocoax® Single core 1 Nc Ac) with a total length of 3m, 0.5mm external diameter, and total electrical resistance of 36Ω. The wire is wrapped around the evaporator bends, as shown in Figure 3.3. Thermal contact is obtained by heat sink compound. The heaters are equipped with two thermos-fuses (DMP 11MP 150H 046E) so that the power supply is stopped whenever their temperature rise above 150°C. Thus, all the components in direct contact with the PHP are designed to withstand this maximum temperature.

The electric power, up to 100W, is provided by a power supply (GWInstek® 3610A) corresponding to a radial heat flux up to $12.0W/cm^2\pm0.3$.

The PHP evaporator and the heater are protected by a Polyetheretherketone (PEEK) cover in order to reduce radiation to the external environment.
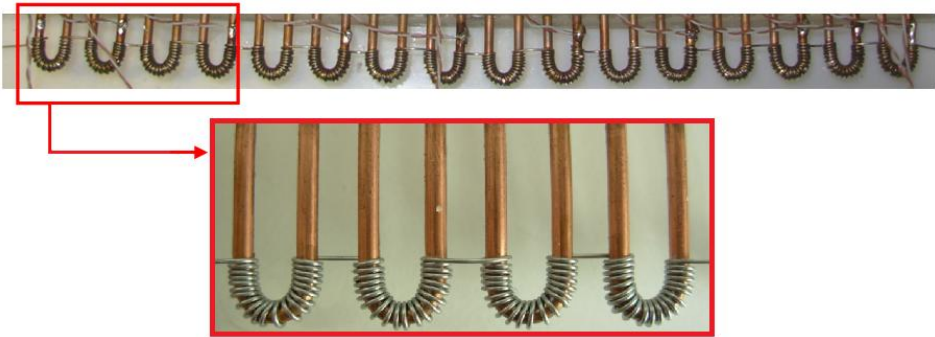
Figure 3.3: Heating wire wrapped on the evaporator section.

The condenser section is 180mm long and it is cooled by means of air fan system. Circular cross section channels are milled on the surface of an aluminum plate so as to host the copper tubes. Then, the PHP condenser is embedded into the heat sink (Figure 3.4 A) and fixed with a finned aluminum back plate (Figure 3.4 B). Thermal contact is obtained by heat sink compound. Four air fans

(ebmpapst.co.uk® 8412N/2GH-214) are located on the heat sink fins in suction mode (Figure 3.4 C).
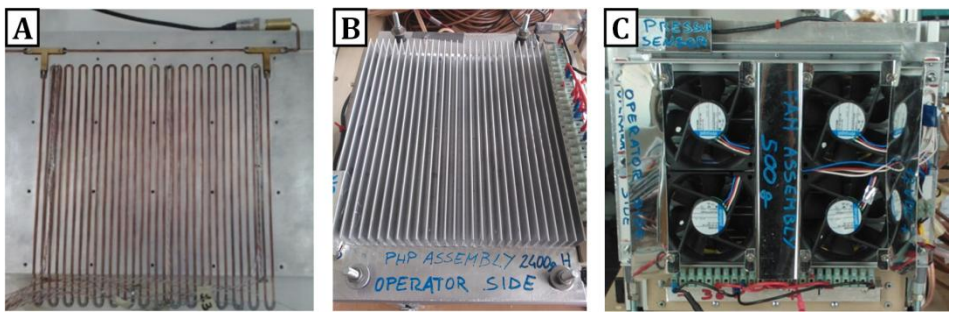
Figure 3.4: PHP condenser section embedded into the aluminum heat sink (A); aluminum back plate (B); air fan system (C).

The effects of the hyper-gravity conditions on the fans rotation speed is shown in Figure 3.5.
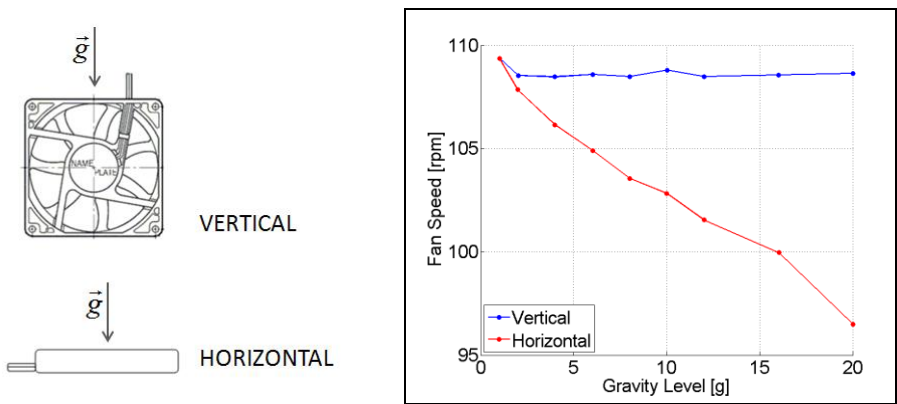
Figure 3.5: Effect of different gravity levels on the air fan speed.

The PHP in vertical position undergoes a negligible fan speed reduction for the whole gravity range, while in the horizontal position this reduction increases with the acceleration level: at 20g the

reduction (~12%) is critical for the cooling characteristics. Thus, horizontal tests have been performed up to 10g (fans speed drop <6%): this kind of decrement is not significant and thus it is assumed that the impact on the experimental results in terms of temperature is negligible.

The experimental set-up is equipped with several sensors:

1. A pressure transducer (Kulite®, ETL/T 312, 1.2bar A) is plugged outside the condenser section (Figure 3.2);
2. Fourteen T type thermocouples (wire diameter 0.127mm, accuracy of ±0.2°C after calibration) are tin soldered on the external tube surface in order to maximize the thermal contact; nine of them are located 6mm above the evaporator section, because of the heating wire, and four in the condenser region. The last one measures the environmental temperature;
3. A three axis accelerometer (Analog Devices® ADXL326) is located on one side of the heat sink.

All the sensors and the power supply are connected to a data acquisition system (NI-cRIO-9073, NI-9214®); signals are recorded at 16Hz.
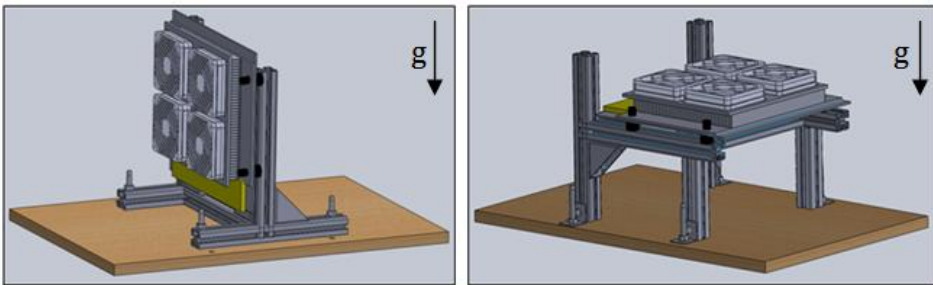
Figure 3.6: PHP position with respect to the gravity direction. On the left, vertical bottom heated mode configuration, on the right horizontal device.

The test-cell (PHP, thermocouples, pressure transducer, g sensor, heating and cooling system) is positioned on a beam structure by means of four anti-vibration bushes. Two different orientations are allowed: the vertical bottom heated mode configuration (heater on the bottom, condenser on the top) and the horizontal one (Figure 3.6).

When located on the LDC, only this cell is accommodated in the gondola (Figure 3.7); all the peripheral facilities (power supply, DAQ system) are located in the hub in order to avoid hyper-gravity on the electronic equipment. Shielded wires (6.5m long) pass through the LDC branch and connect the test cell to the hardware in the hub. Finally, the DAQ system is remotely controlled from an external control room.
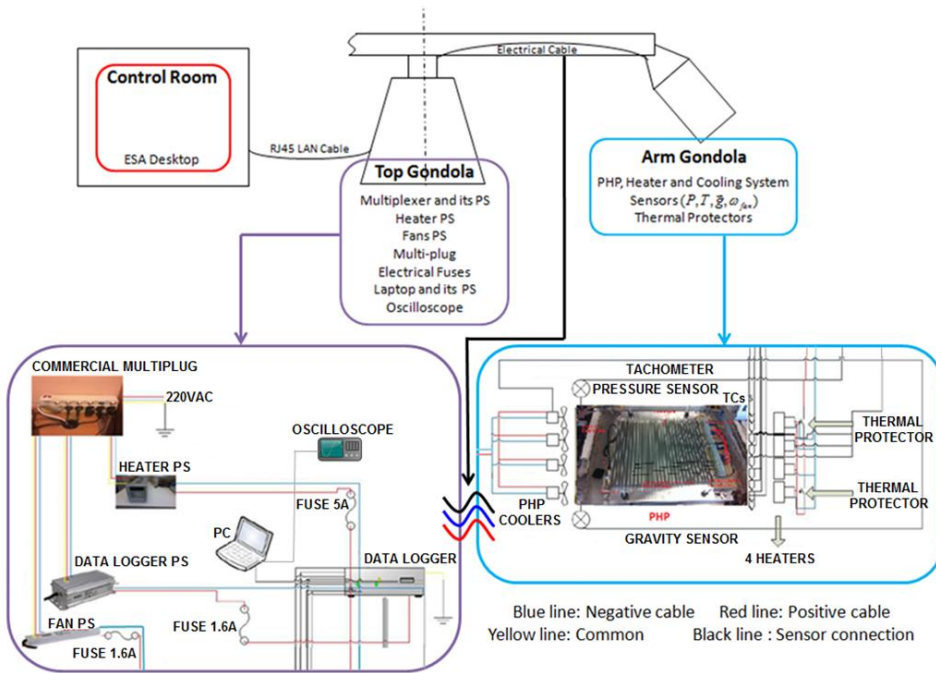
Figure 3.7: General schematic of the connections; location of the various instruments.

There are no mechanical connections between the gondola floor and the PHP support since the test rig is kept still and stable thanks to the gravity modified acceleration; the LDC is, indeed, a passive swing out system and each gondola will orient such that the gravity vector is always perpendicular to its floor.

3.3   Experimental procedure

The list of the performed experiments is shown in Table 3.1. The device has been tested in two configurations (vertical bottom heated mode and horizontal) under different heating powers (50, 70 and 100W) and gravity levels (1g - 20g). Ground tests have been used for comparison. It is worth to note that this is the first time that a tube PHP has been tested in horizontal and vertical position at such high acceleration levels.

Every experiment has been carried out with the following procedure: first, the PHP test rig is arranged in vertical (bottom heated mode) or horizontal configuration and, if hyper-gravity is required, the PHP is placed inside an LDC gondola. Then the gondola is closed and the gravity vs. time profile is set. Afterwards, the initial heat input level is set and the experiment is powered up at normal gravity to warm-up the PHP for at least 8 minutes[6]; then, even if every test is performed with a peculiar gravity and heat power history, each heat input or gravity level is kept for 8 minutes. Finally the heating power supply is switched off and a cool down phase of 15 minutes is performed at normal gravity so that all the temperatures reach equilibrium at the room conditions.

Repeatability test have been performed for almost every testing condition.

---

[6] The system is, indeed, able to reach a pseudo steady state, which means all the temperature signals show an average value constant in time, in about 180s.

Test	Location	Mode	Heat Input [W]	Gravity Level [g]	Repeated?
1	Ground	Horizontal	50→70→100	1	Yes
2	Ground	Vertical	50→70→100	1	Yes
3	LDC	Horizontal	2x(50→70→100→70→50)	2→4→6→10	Yes
4	LDC	Horizontal	100	1→2→4→6→8→10	Yes
5	LDC	Horizontal	70	1→4→8→10	No
6	LDC	Horizontal	50	1→4→6→8→10	No
7	LDC	Vertical	50→70→100	2	Yes
8	LDC	Vertical	50→70→100	4	Yes
9	LDC	Vertical	50→70→100	6	Yes
10	LDC	Vertical	50→70→100	10	Yes
11	LDC	Vertical	100	1→4→8→10→12→16→20	Yes
12	LDC	Vertical	70	1→4→5→6→7→8→10→12	No
13	LDC	Vertical	50	1→2→3→4→5→6→8→10	No

Table 3.1: List of the performed experiments.

3.4   Results

Results are presented mainly in terms of temperature and pressure time evolutions.

The tube wall temperature trends, both near the evaporator zone[7] (reddish colors), in the condenser section (bluish colors), and of the environment (green) are shown together with the heat input level on the secondary y-axis. In case of centrifugal test, the gravity acceleration is reported directly over the plot line.

The pressure signal recorded just outside the condenser section is presented both in term of raw (light blue region) and filtered data (solid blue line). As for the temperatures, the heat input level is shown on the secondary y-axis, while, in the case of centrifugal test, the gravity acceleration is reported directly over the plot line.

3.4.1   Ground tests

Ground tests have been performed in the vertical and horizontal position increasing the heat input from 50W to 100W with an intermediate step at 70W. The starting heat input level is kept for 16 minutes while the following are kept for 8 minutes each.

Vertical and horizontal orientations show very different behaviors confirming that, in a perfect 2D layout with a relatively high number of channels, gravity still plays an important effect on the PHP thermal behavior (Figure 3.8). Indeed, in the horizontal working mode, the fluid motion is not assisted by gravity; oscillations are less frequent (Figure 3.9) and the heat transfer rate is less efficient too; consequently temperatures near the evaporator set to a higher level with respect to the vertical position.

---

[7] The evaporator thermocouples are actually located 6mm above the heater in the adiabatic zone.
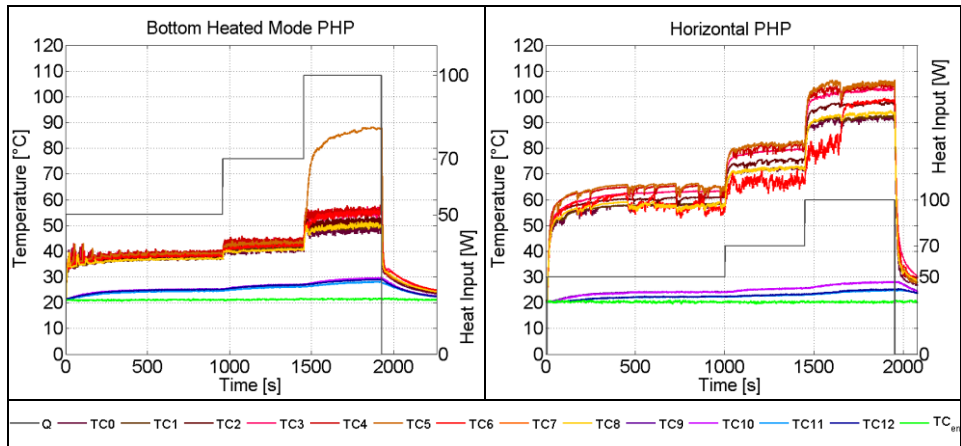
Figure 3.8: Ground experiments, tube wall temperatures. On the left, bottom heated mode configuration, on the right, horizontal PHP. For thermocouples positions refer to Figure 3.2.
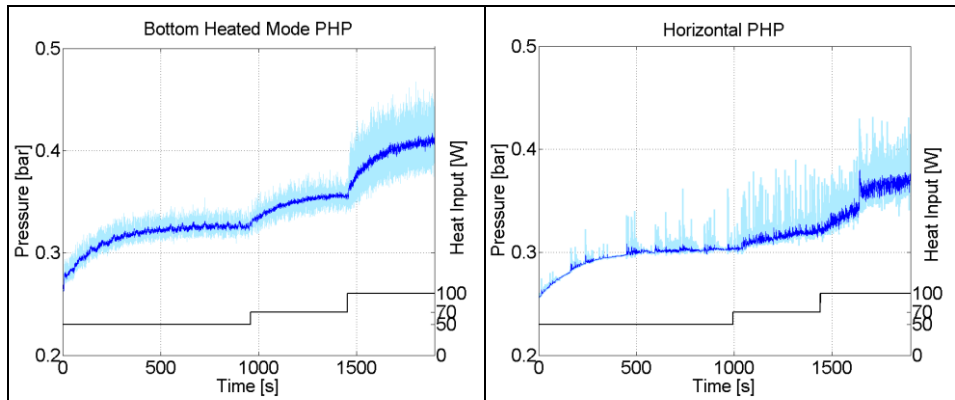
Figure 3.9: Ground experiments, pressure signal. On the left, bottom heated mode configuration, on the right, horizontal PHP. Solid lines represent the filtered data; colored ranges the non filtered pressure.

In both the tested configurations, after a start-up period of about 180s, temperatures and pressure are able to reach a regular oscillating regime. In the vertical case, however, the evaporator

temperatures set in a 10°C range, while the horizontal temperatures space up in a 30°C range. Thus it is evident that gravity helps to stabilize the performance of the device.

In addition, the vertical operation shows an interesting feature at the higher heat input level (100W): some channels (only one in this case) undergo a sudden thermal crisis probably due to fluid motion dampening or local dry-out[8]; its temperature is, indeed, more than 30°C higher than all the other measured near the evaporator zone meaning that the PHP is reaching its operative limit.

3.4.2 Large Diameter Centrifuge tests

The alternation of the gravity field can affect the PHP in two different ways: it might influence directly the flow motion, if the gravity vector has components along the flow path; at the same time, it can alters the ratio between the buoyancy force and the surface tension acting on the liquid and, thus, the internal flow pattern.

In order to have an initial slug/plug distribution, the static fluid confinement criterion [24] should be satisfied:

$$Bo = \frac{g(\rho_l - \rho_v)d_{in}^2}{\sigma} \leq 4 \qquad (3.1)$$

g is the gravity acceleration, $\rho_l - \rho_v$ is the difference between liquid and vapor densities at saturated conditions, d_{in} is the tube internal diameter and σ is the surface tension.

---

[8] Local dry out occurs when at least one temperature near the evaporator side rises evidently with respect to the others. Probably the vapor quality in this zone is very close or equal to one.
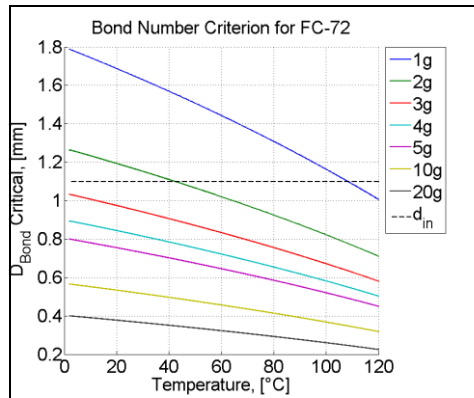
Figure 3.10: Critical internal diameter $(Bo(d_{cr}) = 4)$ as function of temperature at different acceleration levels for the FC-72.

The critical diameter obtained by the previous criterion is reported in Figure 3.10 as function of temperature at different acceleration levels. The real PHP internal tube diameter is also plotted in dashed line: if the critical diameter is less than the actual diameter, the fluid may not be in a confined region anymore and stratification may occur. For the tested device, theoretically, this transition should occur between 2g and 3g.

Since the tested PHP does not allow any fluid visualization, it is possible to argue about the flow transition only in terms of thermal response and local fluid pressure fluctuations. Indeed, it is here assumed that the flow regime is altered when all the temperatures near the evaporator together with the local pressure in the condenser react instantaneously to a change in the acceleration level.

Horizontal configuration

In the case of a horizontal PHP, the gravity vector is perpendicular to the flow path, thus the flow motion is not directly affected by the increasing acceleration.
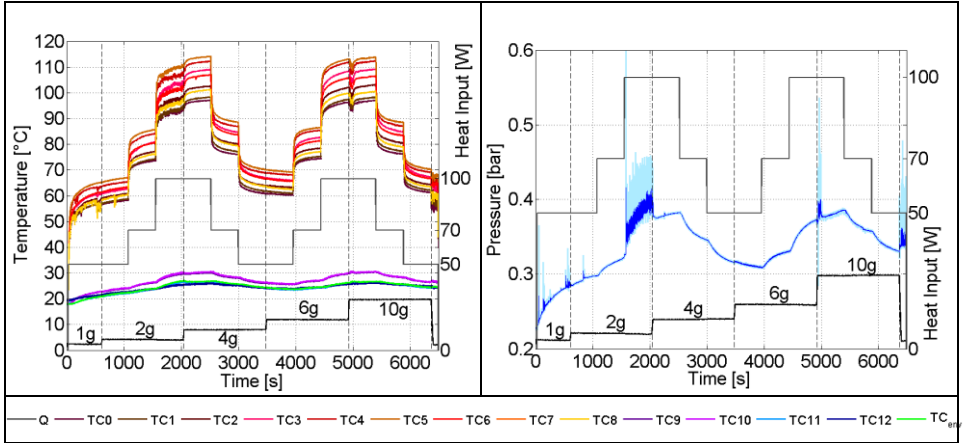
Figure 3.11: LDC experiments, horizontal position, different heat inputs and gravity levels. On the left, wall temperatures; on the right, local fluid pressure. Solid lines represent the filtered data, colored ranges the non filtered pressure. For thermocouples positions refer to Figure 3.2.

The first test in the horizontal position has been carried out by changing both the heat input and the gravity level. At 50W and 1g the device is operating in a start-stop mode and this is clearly visible from the very poor pressure and temperature fluctuation in Figure 3.11. When the gravity level is increased to 2g, only one oscillating event is recognizable at 50W. Keeping the spin at 2g, the heat input level is increased to 70W and the fluid motion seems completely damped out: there are no signal oscillations both in the fluid pressure and in the wall temperatures. Only when the heat input is set to 100W, the fluid pressure shows a higher peek, oscillation is reactivated and kept stable till the next increment of the gravity level. When the spin is increased to 4g the device stops working in a few seconds: fluid pressure as well as the wall temperatures do not oscillate and thermal performance slightly decreases as shown in the

zoom of Figure 3.12. Afterwards, the heat input level is decreased to 70W and then 50W at 4g but no reactivation occurred, as expected.
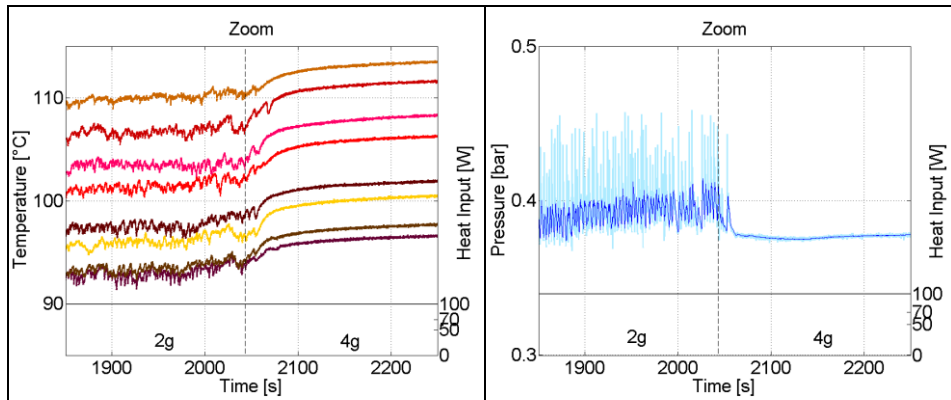
Figure 3.12: LDC experiments, horizontal position. Zoom of the transition between 2g and 4g at 100W. On the left, near evaporator temperatures; on the right, local fluid pressure. Solid lines represent the filtered data, colored ranges the non filtered pressure. For thermocouples positions refer to Figure 3.2.

For the next duty cycle, gravity is increased to 6g and, again, the heat input level is enhanced from 50W to 100W. Only a sudden pressure peek is recorded at 100W during the transition from 6g to 10g but, contrary to the 2g case, it is only a local event, not sufficient to restart the device operation. No operation is detected afterwards in hyper-gravity but, when the LDC stops and the gravity level gets back to 1g, the PHP recovers a vigorous temperature and pressure oscillation. The experiment has been repeated and no substantial differences arose.

In order to verify the hysteresis effects linked to the heating/gravity history, tests are performed at increasing acceleration levels keeping constant the heat input at the evaporator.
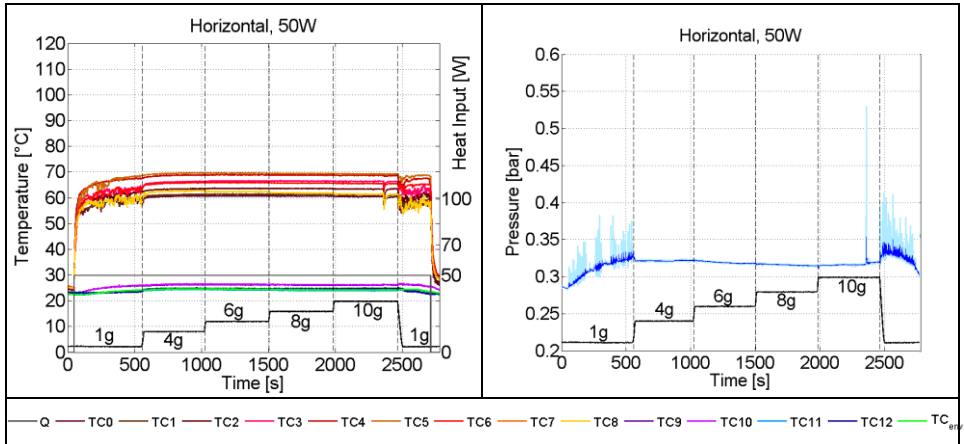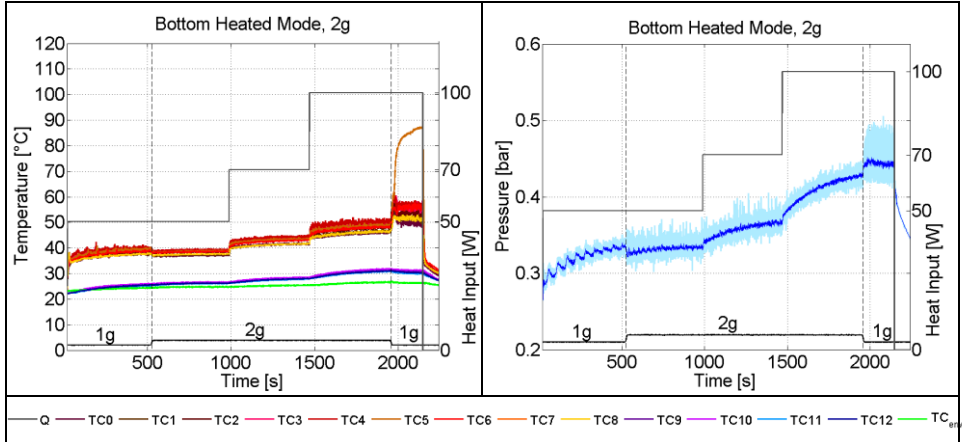
Figure 3.13: LDC tests, vertical position, 50W and various g-levels. On the left, wall temperatures; on the right, local fluid pressure. Solid lines represent the filtered data, colored ranges the non filtered pressure. For thermocouples positions refer to Figure 3.2.
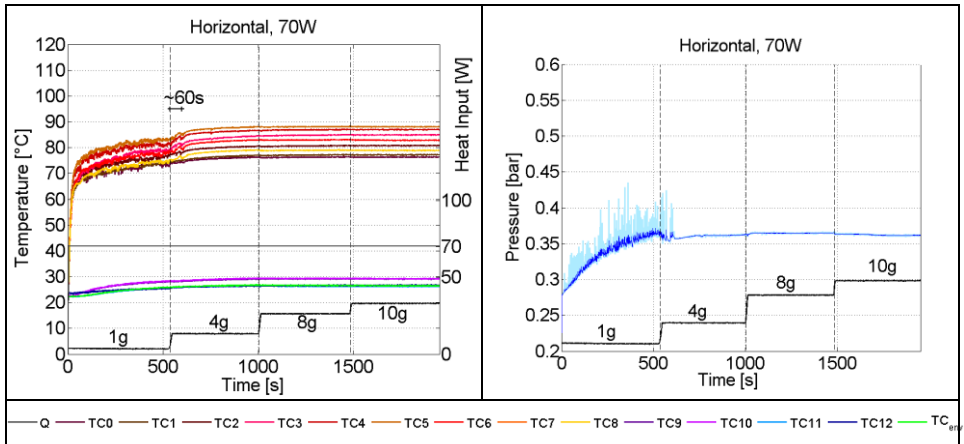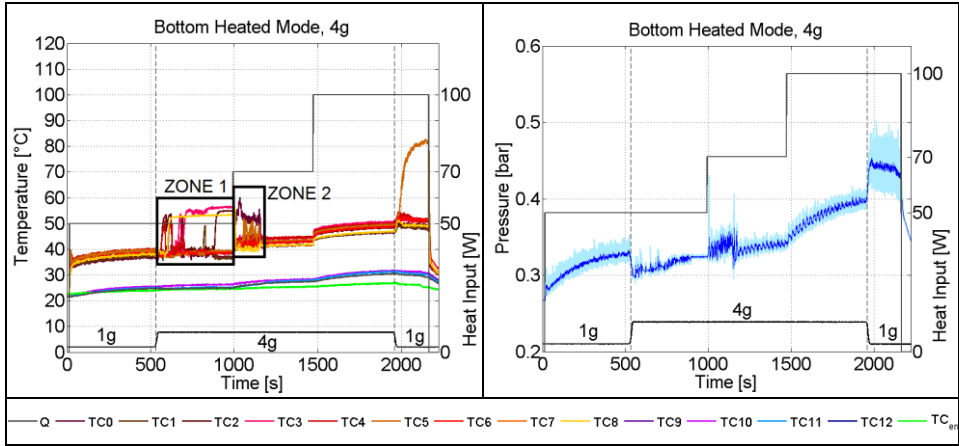

Figure 3.14: LDC tests, vertical position, 70W and various g-levels. On the left, wall temperatures; on the right, local fluid pressure. Solid lines represent the filtered data, colored ranges the non filtered pressure. For thermocouples positions refer to Figure 3.2.
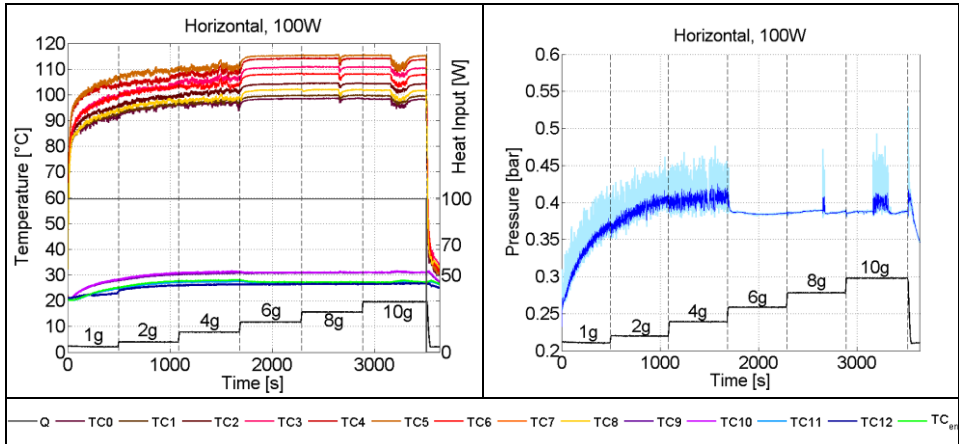
Figure 3.15: LDC tests, vertical position, 100W, various g-levels. On the left, wall temperatures; on the right, local fluid pressure. Solid lines represent the filtered data, colored ranges the non filtered pressure. For thermocouples positions refer to Figure 3.2.

As expected from the previous results shown in Figure 3.11, both test at 50W and 70W show that the PHP stops working when gravity changes from 1g to 4g but the switching off is almost instantaneous at 50W (Figure 3.13) while almost one minute is needed at 70W (Figure 3.14). Differently, if the heat input level is kept at 100W since the very beginning (Figure 3.15), the PHP is able to maintain a stable operation up to 4g showing, by comparison with Figure 3.11, a dependence on the heating/gravity history. Local fluid settlements occur at 8g and at 10g but, as in the previous experiments, these local events are not sufficient to restart the device operations.

Vertical configuration

When the PHP is oriented in a vertical bottom heated position, the acceleration vector is parallel to the flow path direction. The vertical experiments have been carried out in order to understand to what extent gravity may assist or inhibit the flow motion.

For the first tests, the device is started up at 50W in normal gravity conditions till steady state is reached, then the heating cycle 50 - 70 - 100W of the ground experiments is performed at constant gravity level.
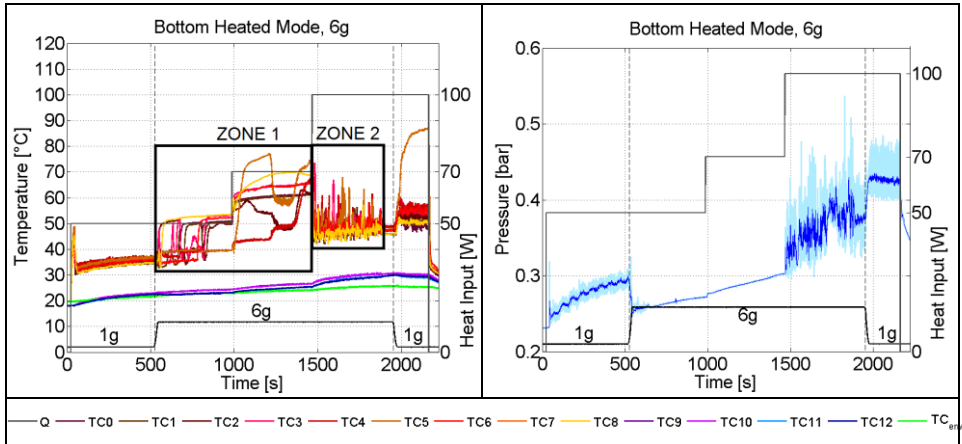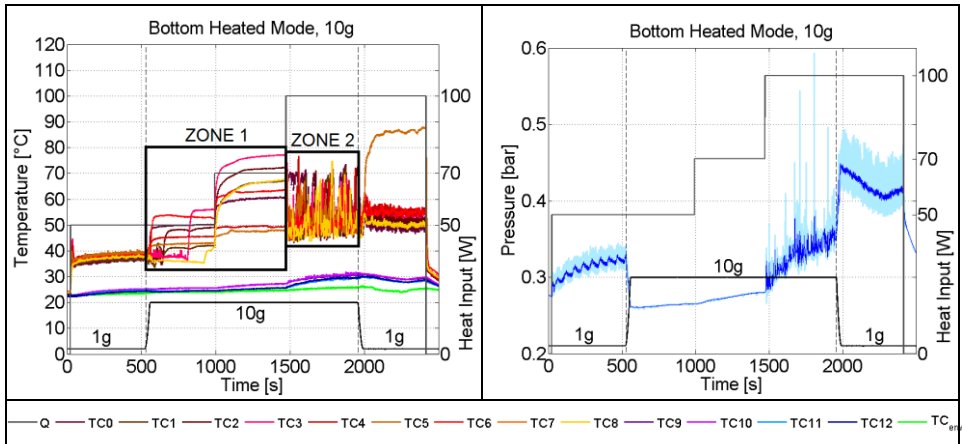

Figure 3.16: LDC tests, vertical position, 2g and various power levels. On the left, wall temperatures; on the right, local fluid pressure. Solid lines represent the filtered data, colored ranges the non filtered pressure. For thermocouples positions refer to Figure 3.2.

Figure 3.16 shows that the PHP is working with slightly better thermal performance at 2g: the average temperature near the evaporator zone can be directly compared between 1g and 2g for 50W and 100W and in both cases it is evidently lower.

Furthermore the 2g acceleration prevents the occurrence of local dry-outs at 100W: in hyper-gravity all the evaporator temperatures are within a narrow range till the LDC stops; then, at 1g, the ochre temperature signal rises identically to the ground test enlightening the occurrence of the thermal crisis. These results are comparable

with the ones achieved on the same apparatus during the 58th ESA Parabolic Flight campaign[9] (see chapter 4) [31].
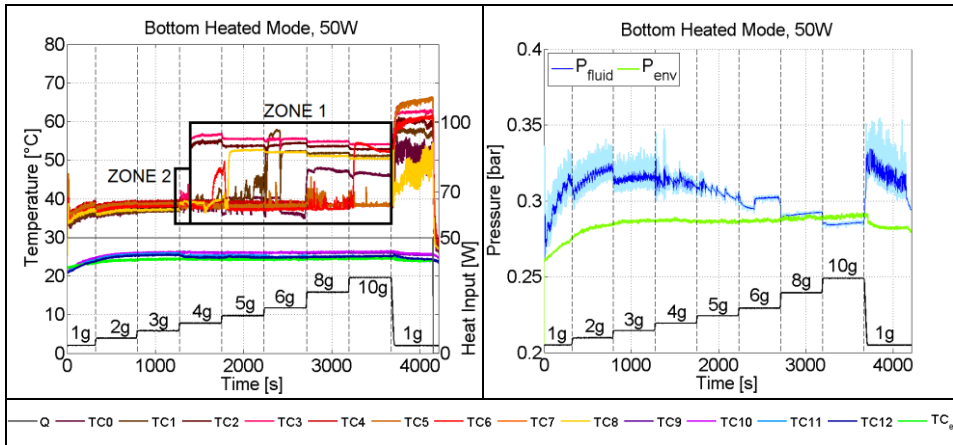

Figure 3.17: LDC tests, vertical position, 4g and various power levels. On the left, wall temperatures; on the right, local fluid pressure. Solid lines represent the filtered data, colored ranges the non filtered pressure. For thermocouples positions refer to Figure 3.2.

Figure 3.17 shows that at 4g, the acceleration strongly inhibits the fluid motion (see the pressure diagram) at 50W and many location in the evaporator undergo local fluid dry-outs with temperature increment (Thermal Crisis - zone 1). At 70W another kind of thermal instability, characterized by more frequent stopover phenomena, resulting in large amplitude and less regular temperature and pressure oscillations, occurs (Transient Thermal Instability - zone 2). Nevertheless the system is able to resettle, after about 120s, and afterwards it kept a stable and efficient operation. No local thermal instabilities are detected at 100W too.

---

[9] During parabolic flights, 1.8g arises when the plane enters or exits from each parabola.

Figure 3.18: LDC tests, vertical position, 6g and various power levels. On the left, wall temperatures; on the right, local fluid pressure. Solid lines represent the filtered data, colored ranges the non filtered pressure. For thermocouples positions refer to Figure 3.2.

Figure 3.19: LDC tests, vertical position, 10g, various power levels. On the left, wall temperatures; on the right, local fluid pressure. Solid lines represent the filtered data, colored ranges the non filtered pressure. For thermocouples positions refer to Figure 3.2.

At 6g (Figure 3.18) the first unstable zone 1 covers a wider heat input range: neither the 50W nor the 70W heat input levels provide enough thermal diving force to promote a stable fluid oscillation. Only at 100W the vapor expansion is strong enough to compete with the gravity acceleration, indeed after a long settlement period characterized by frequent stopovers phenomena and large amplitude temperature and pressure oscillations (zone 2), a stable behavior is finally reached.

At 10g (Figure 3.19) zone 1 covers the 50W and 70W period as for the 6g test but, at 100W, the device is not able anymore to recover from the second transient thermal instability which persists till normal gravity is restored..

As done for the horizontal configuration, additional tests have been performed increasing the acceleration level and keeping the heat input constant (Figure 3.20 - Figure 3.22).

Figure 3.20: LDC tests, vertical position, 50W, various g-levels. On the left, wall temperatures; on the right, local fluid pressure. Solid lines represent the filtered data, colored ranges the non filtered pressure. For thermocouples positions refer to Figure 3.2.
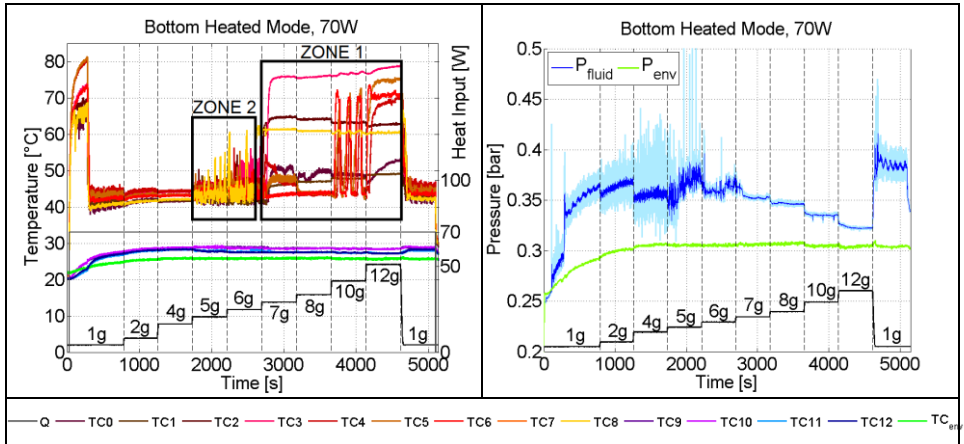
Figure 3.21: LDC tests, vertical position, 70W, various g-levels. On the left, wall temperatures; on the right, local fluid pressure. Solid lines represent the filtered data, colored ranges the non filtered pressure. For thermocouples positions refer to Figure 3.2.
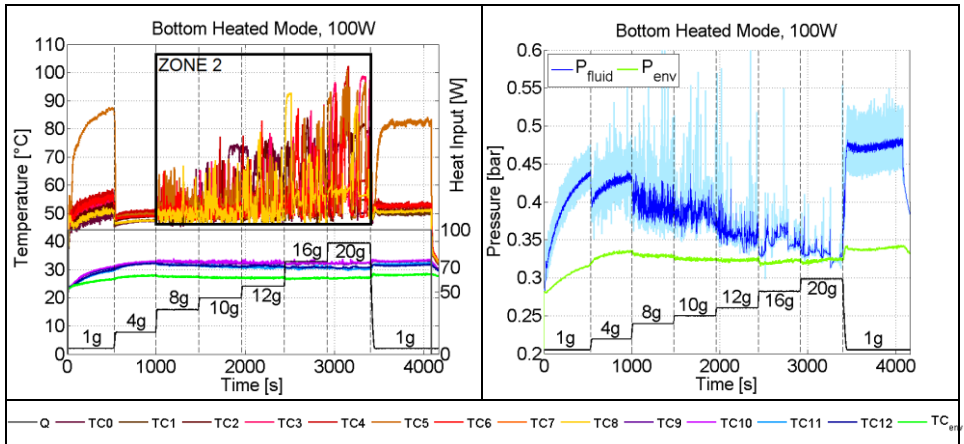
Figure 3.22: LDC tests, vertical position, 100W, various g-levels. On the left, wall temperatures; on the right, local fluid pressure. Solid lines represent the filtered data, colored ranges the non filtered pressure. For thermocouples positions refer to Figure 3.2.

As expected, the two different thermal instabilities detected in the previous tests (zones 1 and 2) occur in these experiments too. Moreover, like the horizontal mode, the performances of the PHP seem to be slightly dependent on the heating/gravity history. For example the two tests performed at the same heat input level, 70W, but coming from different heating/gravity paths (Figure 3.18 and Figure 3.21), show that the PHP respectively undergoes two different thermal instabilities at 6g.

A peculiar behavior can be observed for the PHP powered with 50W (Figure 3.20): at 4g, after a very small period of transient thermal instability (zone 2), the device undergoes a very long thermal crisis (zone 1) and the number of dried-out channel increases with the acceleration level but, interestingly, their temperature level slightly decreases. Furthermore when the LDC stops spinning, the PHP is not able to recover the stable operation.

At 70W, as expected, the transition between 1g, 2g, and 4g enhances the performances of the PHP. Then at 5g and 6g a transient thermal instability occurs driving the PHP to a complete thermal crisis regime. This is comparable with what has been previously observed for 50W. Therefore, it seems that the transient thermal instability is, actually, a transition between a stable mode, where performances are also enhanced by the hyper-gravity, and a thermal crisis regime.

Notice that at 100W (Figure 3.22), the transition between zone 2 and zone 1 is not so evident at least for the tested gravity levels.

In addition, the reported figures show, on the right, the theoretical fluid saturation pressure calculated as a function of the environmental temperature (green line). If the fluid is not moving inside the condenser, its temperature will approach the cooling medium temperature. In other terms, this means that the local fluid pressure approaches the saturation value at room temperature (since

the sensor is plugged outside the condenser) and the PHP is going towards worse working conditions. This is indeed what happens at increasing accelerations after the thermal crisis.

Despite internal flow visualizations could not be performed during the present experimental campaign a possible physical explanation of the observed phenomena may be deduced on the basis of the fluid local pressure. When the PHP is working in the vertical bottom heated mode, the gravity force helps the liquid phase to flow from the condenser section to the evaporator zone (Figure 3.23 A). This alternation of evaporation and condensation assists the motion of the fluid inside the capillary tube and, at normal gravity, an alternation of liquid slug and vapor plugs could be achieved. A small increase of the gravity improves the performances of the PHP while, if gravity increases too much, the liquid phase is forced to flow in the evaporator section but the heating power is not any more sufficient to push it up in the condenser. This leads to the formation of a liquid storage in the bottom of the device and a vapor amass in the top section. Since heating power is provided in the evaporator, bubbles may be still generated within the liquid storage causing a local and more disorderly fluid motion; consequently, the pressure signal is oscillating in a less regular way with respect to the stable operation (Figure 3.23 B). Temperature near the evaporator section also undergoes unstable and incoherent oscillations (zones 2, Transient Thermal Instability). The bubbles generated by the boiling process, however, are inhibited by a further increment of the gravity acceleration (Figure 3.23 C) until the system reaches the overall thermal crisis (zones 1). In this case pressure oscillations are damped and moreover, when gravity increases, the pressure signal shows a step reduction comparable with the gravity step enhancement. Finally, it is assumed that at very high gravity levels bubbles collapse as soon as they are formed because of the very high hydraulic

pressure (Figure 3.23 D). In this condition, the system reaches an equilibrium state, and saturation pressure can be measured in the top vapor.
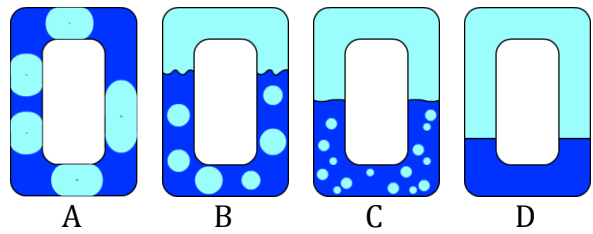
Figure 3.23: Schematic visualization of what possibly happens in a bottom heated mode PHP at increasing g-levels.

4. PHP in micro-gravity: ESA parabolic flight campaigns

In order to provide an overall characterization of the lab-scale PHP in various gravity fields, after the hyper-gravity experiments, which results have been reported in Chapter 3, micro-gravity campaigns have also been conducted on the same experimental set-up making use of the ESA parabolic flights.

Specifically, the research team has participated at two different parabolic flight campaigns, the 58th [31] and the 59th [32], testing the same PHP with two different volumetric filling ratios (50% and 70%).

4.1   Parabolic flights

A long term, controlled, no-gravity environment can be guarantee exclusively performing experiments in orbit (e.g. International Space Station, recoverable satellites and capsules). On Earth, unfortunately, only few seconds of micro-gravity can be reproduced. (e.g. drop tower, parabolic flight, sounding rockets).

Parabolic flights was first introduced for astronaut training; today they are mainly used for testing of space technology and for short duration scientific experiments mainly because of their short turnaround time, low cost, flexible experiment approach and direct on-board intervention possibilities [33].
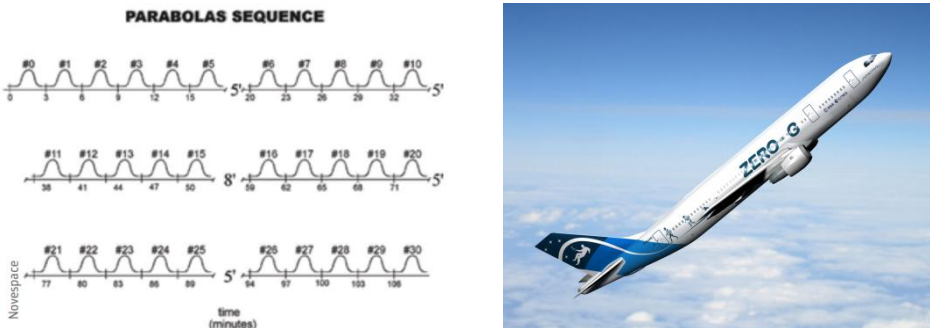
Figure 4.1: On the left, time schedule of the parabolas performed during each parabolic flight; on the right, the Airbus A300 Zero-G during a pull-up phase.

During the ESA parabolic flight campaigns, a reduced gravity environment is obtained by flying a specially modified Airbus A300,

called Zero-G, through a series of parabolic maneuvers which result in approximately 22s periods of 0.01g acceleration. During each campaign, there are typically three flights: a normal mission lasts two or three hours and consists of thirty-one parabolic maneuvers (Figure 4.1).
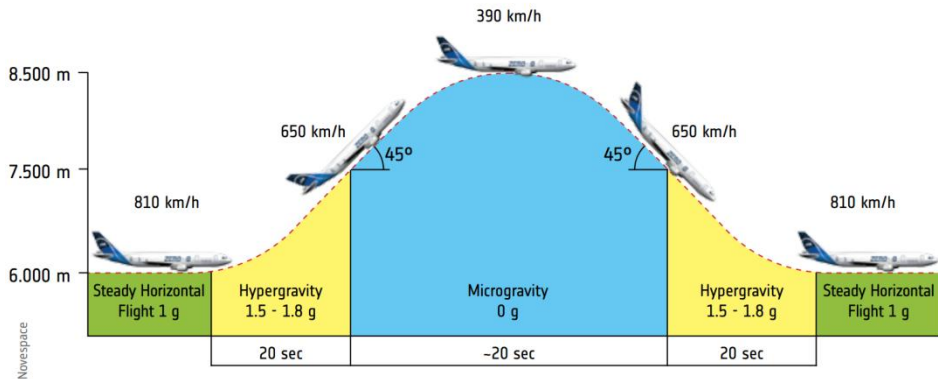
Figure 4.2: Parabolic flight maneuver profile.

Each maneuver begins with the aircraft flying a steady horizontal attitude, with an approximate altitude and speed of 6000m and 810km/h respectively (Figure 4.2). During this steady phase, the gravity level is approximately 1g. At a set point, the pilot gradually pulls up the nose of the aircraft and it starts climbing. This phase lasts for about 20s, during which the aircraft experiences acceleration between 1.5 and 1.8 times the Earth gravity level. At an altitude of 7500m, with an angle of around 45° to the horizontal and with an air speed of 650km/h, the engine thrust is reduced to the minimum required to compensate for the air drag. At this point the aircraft follows a free fall ballistic trajectory (i.e. a parabola) lasting approximately 20s, during which weightlessness is achieved. The peak of the parabola is around 8500m, at which point the speed has dropped to about 390km/h. A symmetrical 1.8g pullout phase is then

executed on the down side of the parabola to bring the aircraft back to its steady horizontal flight in about 20s. There is an interval of two minutes between two subsequent parabolas. Parabolas are executed in sets of five. At the end of each set, a longer time (i.e. 5 or 8 minutes) is elapsed to allow experimenters enough time to carry out modifications to their set-up.

4.2   Experimental apparatus

The same experimental apparatus characterized on ground and in hyper-gravity conditions (see chapter 3), has been used to perform both the two parabolic flight campaigns. Thus, for detailed technical information one should refer to section 3.2.

Briefly, the PHP structure consists of a planar, copper tube (DI/DO 1.1mm/ 2.0mm) folded so as to obtain 32 parallel branches. The tube is evacuated and partially filled of degassed FC-72. The PHP is heated up making use of electric resistors wrapped around the evaporator bends, while the condenser section is embedded into a heat sink and cooled by forced convection. A pressure transducer is plugged outside the condenser section; an accelerometer[10] tracks the gravity load during the flight maneuvers; in addition, the PHP is equipped with calibrated T thermocouples, nine located 6mm above the evaporator zone, four in the condenser region and one is measuring the external temperature. Both horizontal and vertical bottom heated mode configurations are allowed.

Instead of being placed on the LDC gondola, for these experimental campaigns, the whole system (test cell and DAQ) is located on a test-rig plate which respects the ESA/Novespace

---

[10] In the case of micro-gravity experiments the adopted g-sensor is the Dimension Engineering® DE-ACCM3D.

standards [33] (Figure 4.3). Then the device is fixed to the aircraft floor and plugged to the internal electric line of the plane.

Figure 4.3: Test cell and DAQ sistem located on the test ring plate.

4.3   Experimental procedure

The PHP has been investigated on ground and in flight, in horizontal and bottom heated mode position, from 50W to 100W.

In the case of the flight experiments, the device is warm-up during the parabola zero; then the desired heat input level is set and kept constant for the next five parabolas. The heat input level is changed during the five minutes pause at normal g between each parabolic sequence in such a way that the steady state is reached at the beginning of each parabolic trajectory. The above strategy allows exploiting all the parabolas and show that data are repeatable.

In addition, in order to evaluate how much the PHP performances in micro-gravity differ from the behavior of the device at 1g in horizontal position, dynamic investigations have been performed on ground. These tests have the following procedure: from a steady state bottom headed mode configuration, the device is tilted in horizontal for 22s and then back again in vertical position for 2 minutes. The dynamic sequence is repeated five times before changing to another

heat input level. In this way, the more similar gravity head variation with respect to a parabolic maneuver is reproduced.

4.4   Results

Results are presented mainly in terms of temperature and pressure time evolutions. Reddish colors stand for near evaporator temperatures[11], bluish colors characterize the condenser section while the green line represent the environmental data. The pressure signal is reported both in term of raw (light blue region) and filtered data (solid blue line).

In case of ground tests the secondary y-axis reports the change in the orientation (0.01 = horizontal position; 1 = vertical bottom heated mode configuration); in case of flight tests the secondary y-axis reports the gravity acceleration.

4.4.1   58th parabolic flight campaign

During the 58th parabolic flights campaign, the device has been tested with a 0.50 ± 0.03 filling ratio [31].

Vertical position

In the vertical position with the evaporator on the bottom in gravity conditions the acceleration field is directed as the flow path, thus it gives a net contribution to the fluid momentum. For this reason both occurring of the hyper and the micro-gravity conditions are expected to affect the PHP thermal response.

Since the recorded data show perfect repeatability over the five parabolas at the same heat input level, the temperature temporal trend of only one single parabola is shown. In order to compare the

---

[11] The evaporator thermocouples are actually located 6mm above the heater in the adiabatic zone.

dynamic response of the PHP in-flight configuration and the PHP on ground during the Vertical to Horizontal to Vertical maneuver, also a single tilting operation is shown at the same heat input level.

Looking at Figure 4.4 - Figure 4.9, the effect of micro-gravity is evident for all the heat input levels: temperatures near the evaporator section increase because the fluid motion is no more assisted by gravity, pressure oscillations are less frequent and consequently the heat transfer rate is less efficient. Pressure results are shown only for the 50W tests; similar trends have been achieved for the other heat inputs. It is worth to stress the fact that the PHP fluid motion does not stop during micro-gravity nor during the 20s of horizontal tilting maneuver. However, it is plausible that the fluid is oscillating instead of circulating.

The occurring of the second hyper-gravity period, in last part of the parabolic trajectory, assists the fluid motion bringing back the device to its previous thermal regime. Note that, as reported in the previous chapter, hyper-gravity slightly enhances the performance of the device since it favorites the fluid motion improving the global heat transfer. In addition, as already seen in the LDC experiments, hyper-gravity is strong enough to avoid or, at least, weak[12] the occurrence of dry-outs, which might appear on ground.

The thermal response to the absence of acceleration looks very similar to the thermal response to the ground tilting maneuver. Note that during the ground tests, hyper-gravity is of course absent and the device is not able to recover the previous thermal regime as faster as during the flight experiments. The maximum temperatures reached by the evaporator during micro-gravity and during the horizontal period on ground, however, are the same for all the heat

---

[12] At 100W, for example, the augmented acceleration is not enough to avoid the occurrence of the thermal crunch, but still has a positive effect in recovering the previous thermal regime.

input levels; the maximum difference is around 3K: the presence of the first hyper-gravity period on flight, indeed, retards the performance reduction at 0.01g, and thus the temperature are a little bit lower with respect the ones achieved on ground, but, as said, the variation is negligible. This proves that the thermal regime of a planar PHP subjected to 20s of micro-gravity environment is evolving to the same regime of a PHP operating on ground in horizontal position.
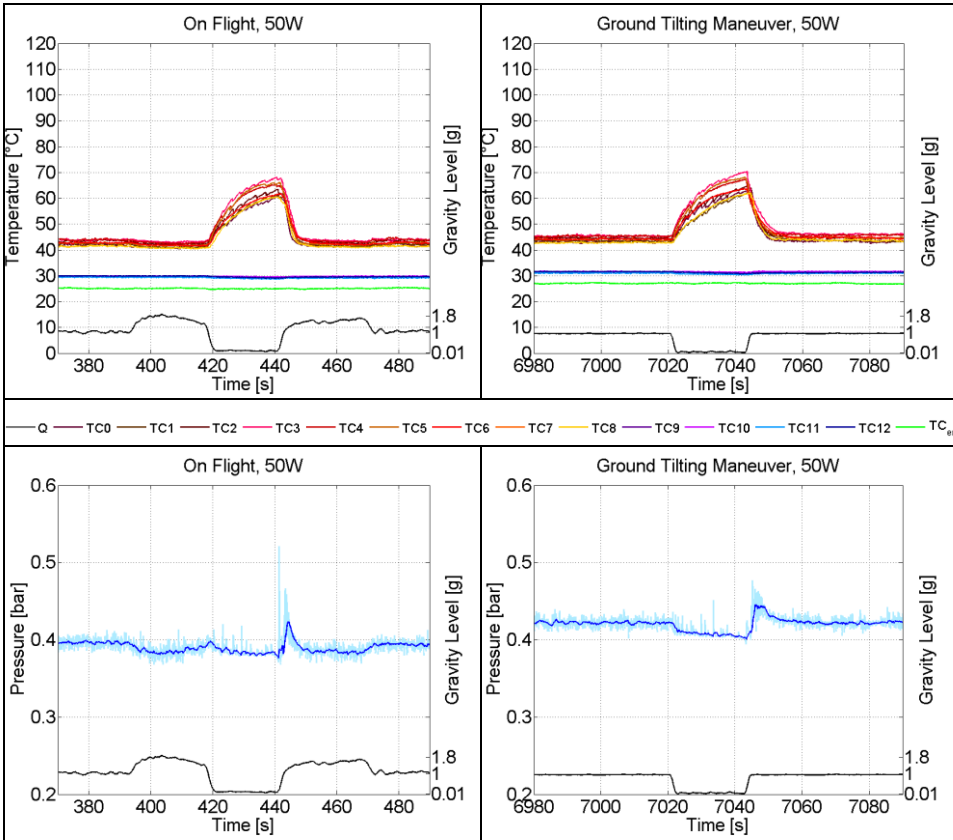
Figure 4.4: Vertical PHP, 50W. On the left, flight test; on the right ground test; on the top, wall temperatures; on the bottom, local fluid pressure. Solid lines represent the filtered data, colored ranges the non filtered pressure. For thermocouples positions see Figure 3.2.
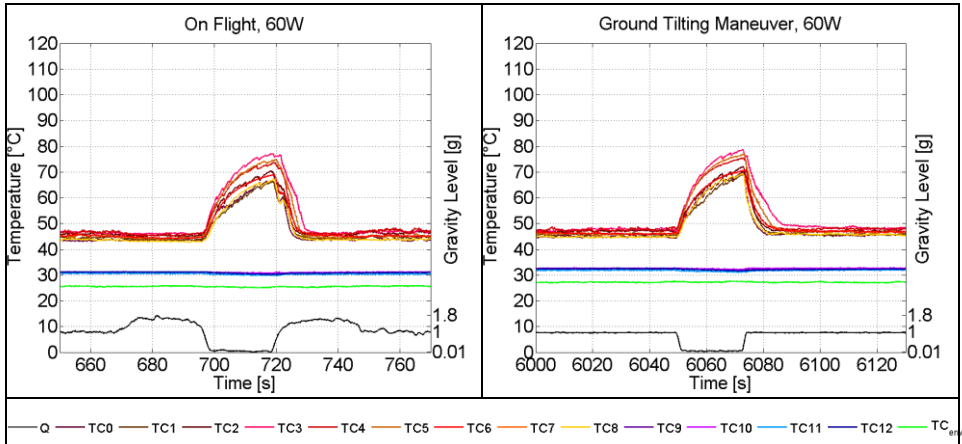
Figure 4.5: Vertical PHP, 60W, wall temperatures. On the left, flight test; on the right ground dynamic test. For thermocouples positions refer to Figure 3.2.
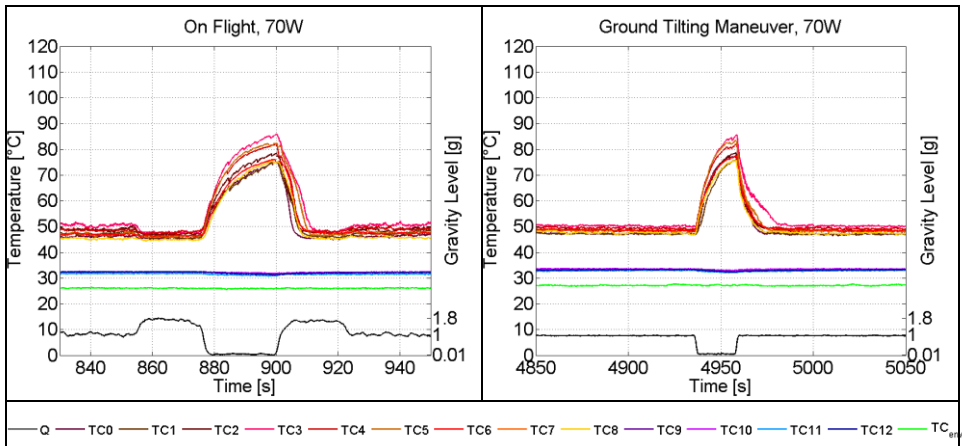
Figure 4.6: Vertical PHP, 70W, wall temperatures. On the left, flight test; on the right ground dynamic test. For thermocouples positions refer to Figure 3.2.
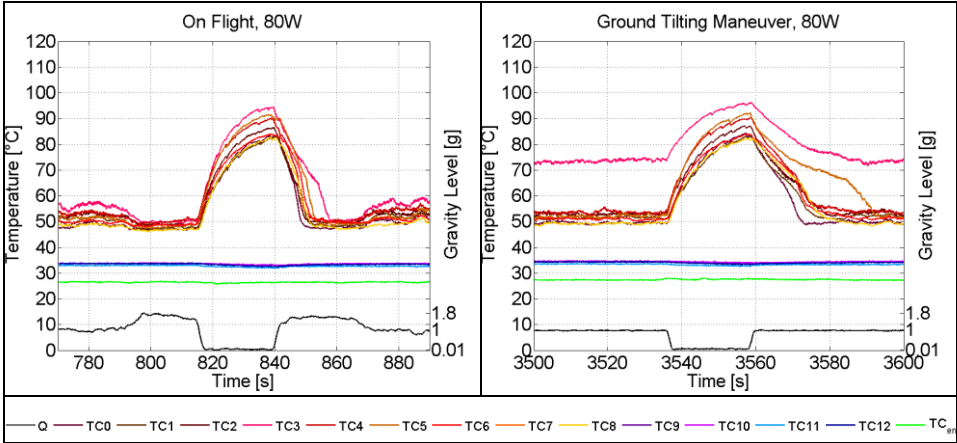
Figure 4.7: Vertical PHP, 80W, wall temperatures. On the left, flight test; on the right ground dynamic test. For thermocouples positions refer to Figure 3.2.
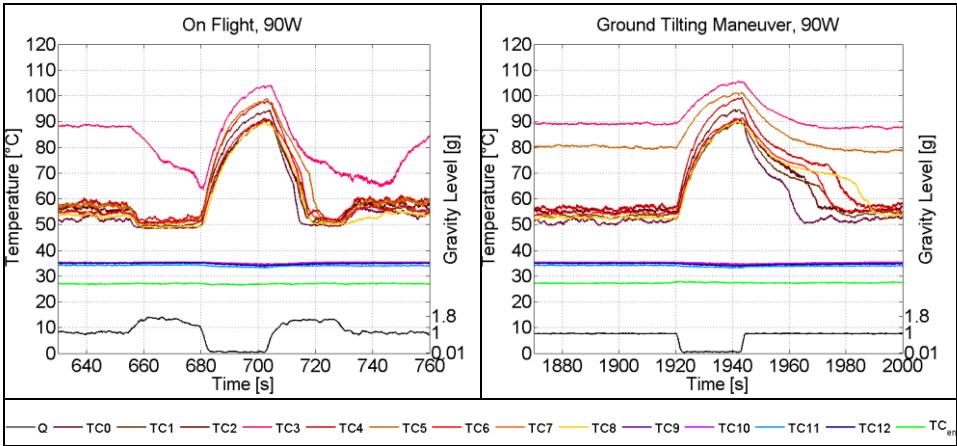
Figure 4.8: Vertical PHP, 90W, wall temperatures. On the left, flight test; on the right ground dynamic test. For thermocouples positions refer to Figure 3.2.
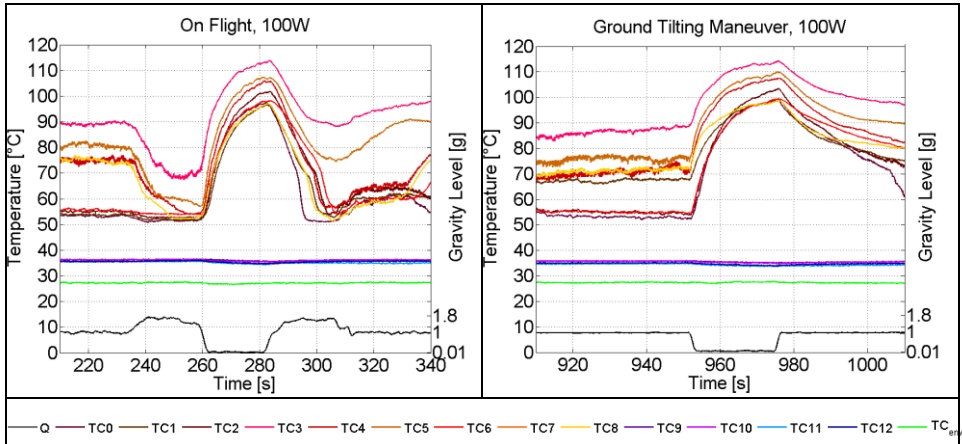
Figure 4.9: Vertical PHP, 100W, wall temperatures. On the left, flight test; on the right ground dynamic test. For thermocouples positions refer to Figure 3.2.

Horizontal position

In the horizontal position the acceleration field is normal to the flow path direction. For this reason both hyper and micro-gravity conditions are not giving a net contribution to the fluid momentum along the channels and are not expected to greatly affect the PHP thermal response.

The direct comparison between the flight data with ground experiments confirms that the variation of the acceleration field has no measurable effect on the PHP in the horizontal position.
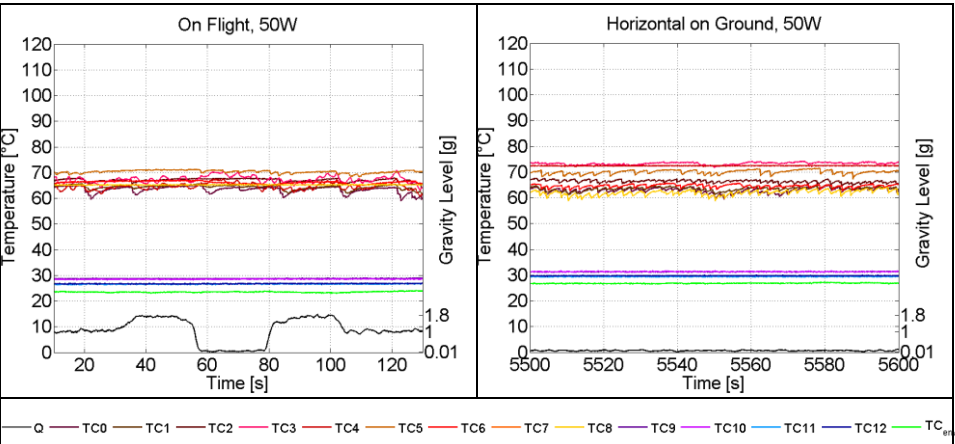
Figure 4.10: Horizontal PHP on flight tested at 50W (on the left); comparison with ground dynamic tests (on the right). For thermocouples positions refer to Figure 3.2.
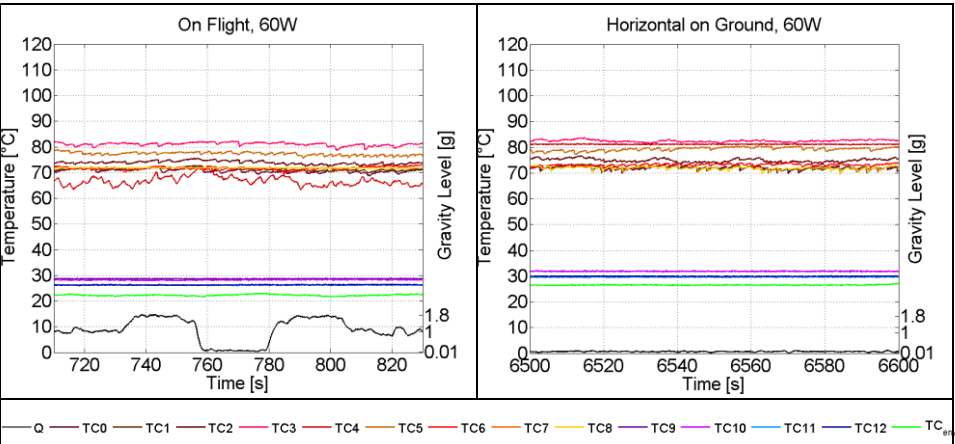
Figure 4.11: Horizontal PHP on flight tested at 60W (on the left); comparison with ground dynamic tests (on the right). For thermocouples positions refer to Figure 3.2.
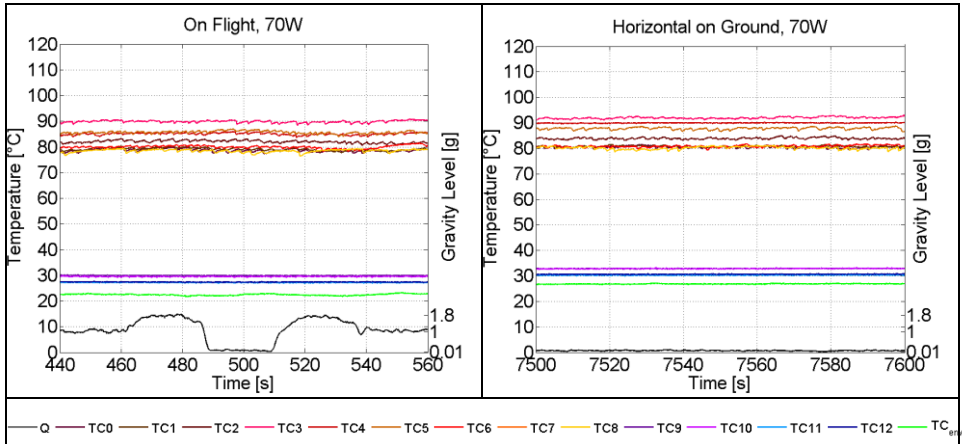
Figure 4.12: Horizontal PHP on flight tested at 70W (on the left); comparison with ground dynamic tests (on the right). For thermocouples positions refer to Figure 3.2.
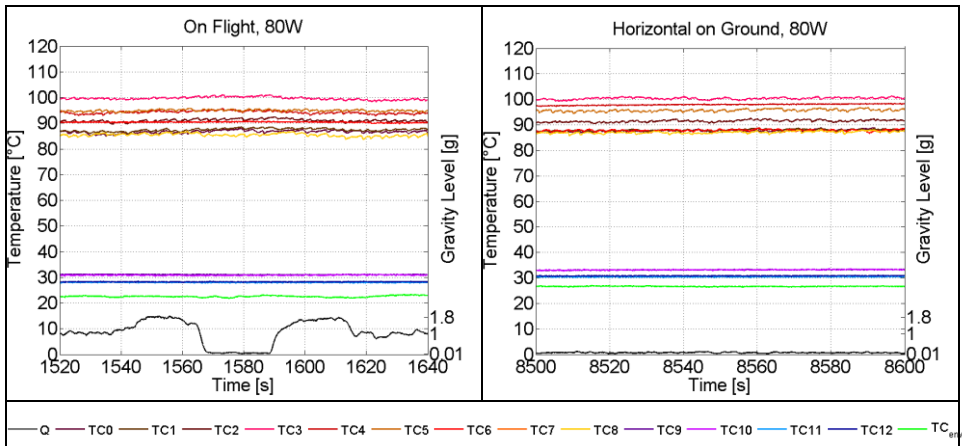
Figure 4.13: Horizontal PHP on flight tested at 80W (on the left); comparison with ground dynamic tests (on the right). For thermocouples positions refer to Figure 3.2.
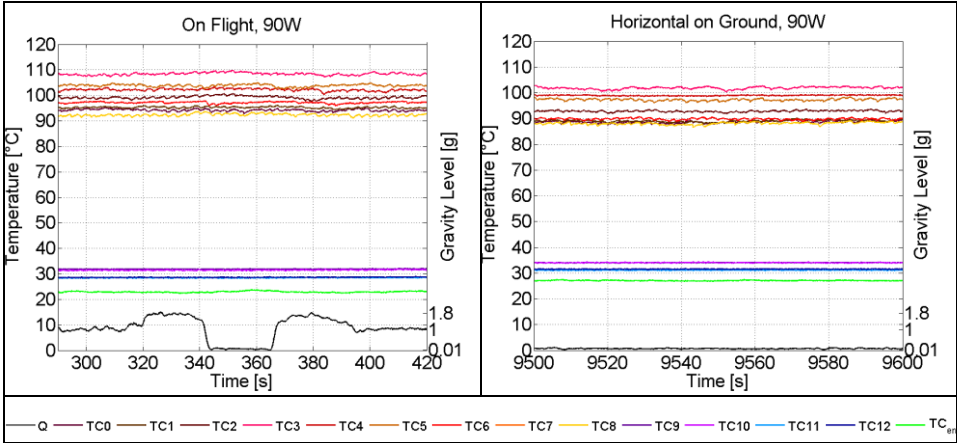
Figure 4.14: Horizontal PHP on flight tested at 90W (on the left); comparison with ground dynamic tests (on the right). For thermocouples positions refer to Figure 3.2.
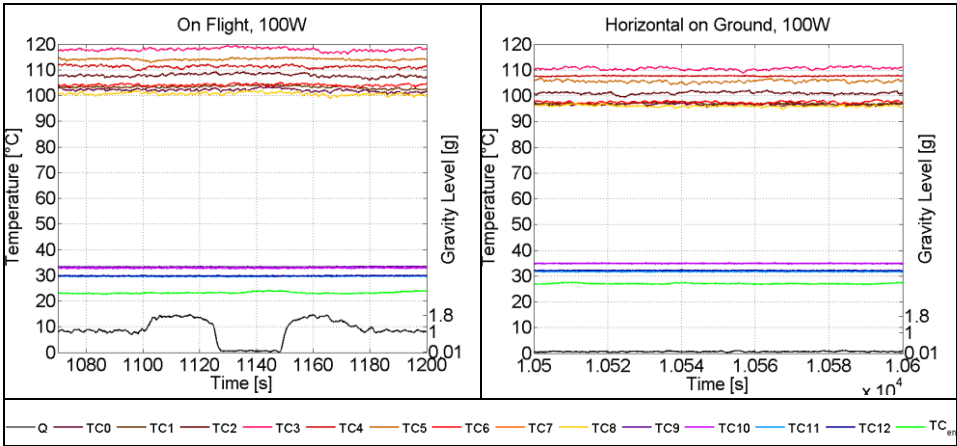
Figure 4.15: Horizontal PHP on flight tested at 100W (on the left); comparison with ground dynamic tests (on the right). For thermocouples positions refer to Figure 3.2.

4.4.2 59th parabolic flight campaign

During the 59th parabolic flights campaign, the device has been tested with a 0.70 ± 0.03 filling ratio [32].

The device has been investigated only in vertical bottom heated mode configuration and results confirm that, during a parabolic flight, the PHP operation is strongly affected by the gravity field variation: hyper-gravity slightly assists the flow motion while during micro-gravity the PHP undergoes sudden temperature increment in the evaporator zone. The second hyper-gravity period is able to bring the PHP back to the previous thermal regime.

However, the 70% PHP has shown an interesting feature with respect to the 50% PHP tested during the 58th parabolic flight campaign (see section 4.4.1). In micro-gravity, indeed, instead of having a high sharp increment of temperatures, the thermal level of each branch reaches a sort of plateau characterized by oscillating temperatures. Thus, the PHP is actually still working even if the absence of gravity reduces its global performance.

The same thing can be inferred from the pressure signal. During micro-gravity, the 50% PHP shows pressure oscillations less frequent with respect normal gravity; moreover the associated mean value tends to decrease approaching equilibrium conditions at the local temperature (remember that the pressure transducer is plug just outside the condenser section). For the 70% PHP on the other hand, not only the mean pressure value is stable or even increases with respect normal gravity, but also the oscillations remain unchanged. These evidences prove that the fluid within the PHP is still moving both oscillating and circulating.

Finally, it can be observed that the higher quantity of liquid retards of 10/20W the appearance of dry-out in the evaporator channels.
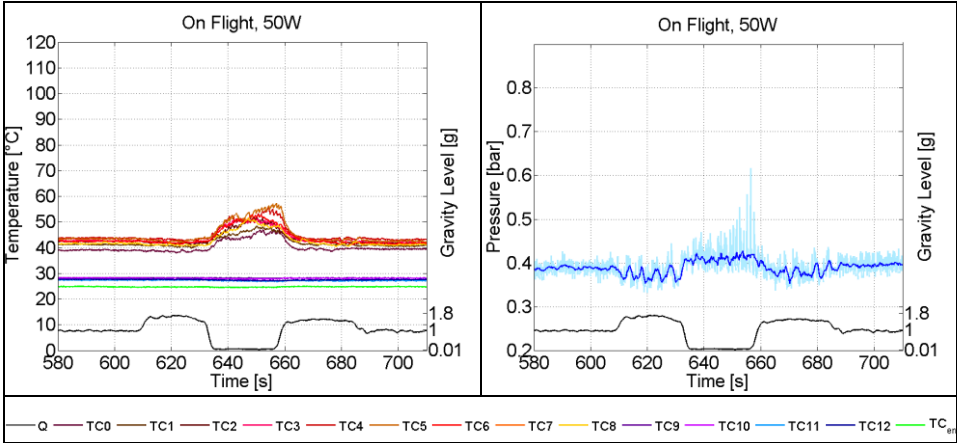
Figure 4.16: Flight experiments, vertical configuration at 50W. On the left, tube wall temperatures; on the right, local fluid pressure. Solid lines represent the filtered data, colored ranges the non filtered pressure. For thermocouples positions refer to Figure 3.2.
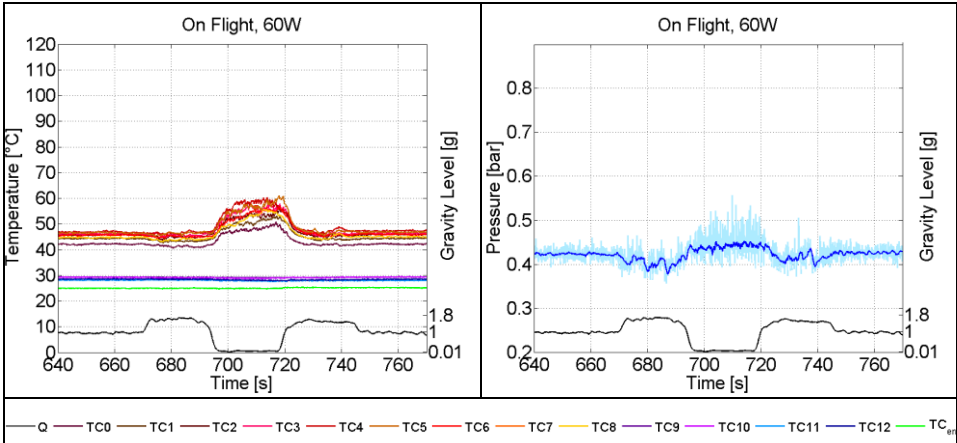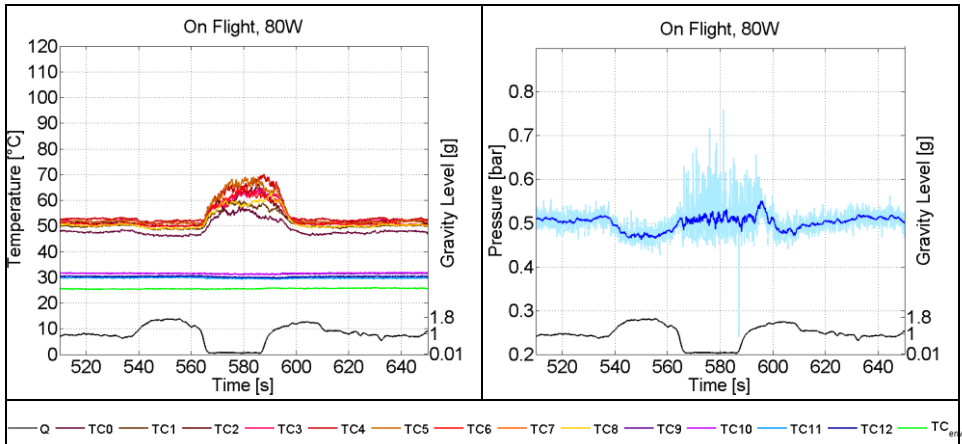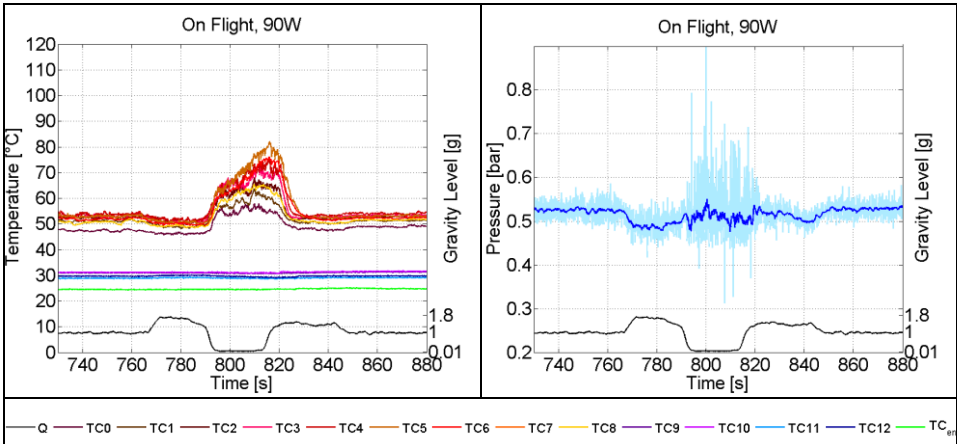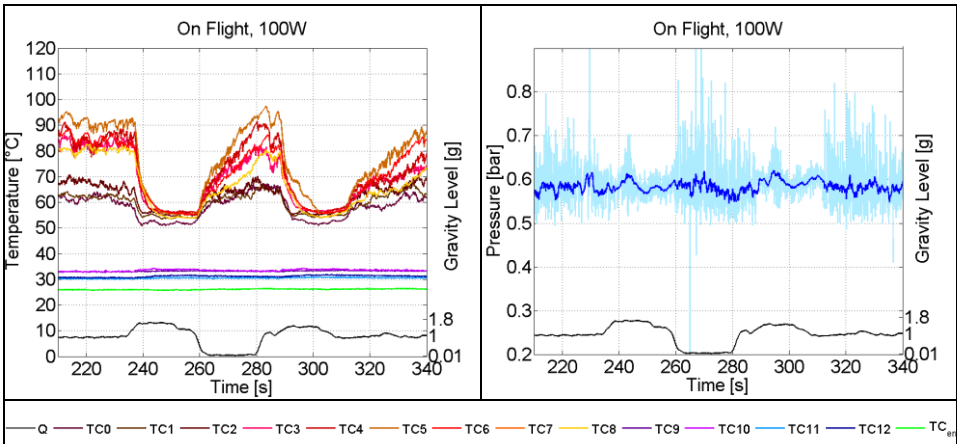

Figure 4.17: Flight experiments, vertical configuration at 60W. On the left, tube wall temperatures; on the right, local fluid pressure. Solid lines represent the filtered data, colored ranges the non filtered pressure. For thermocouples positions refer to Figure 3.2.
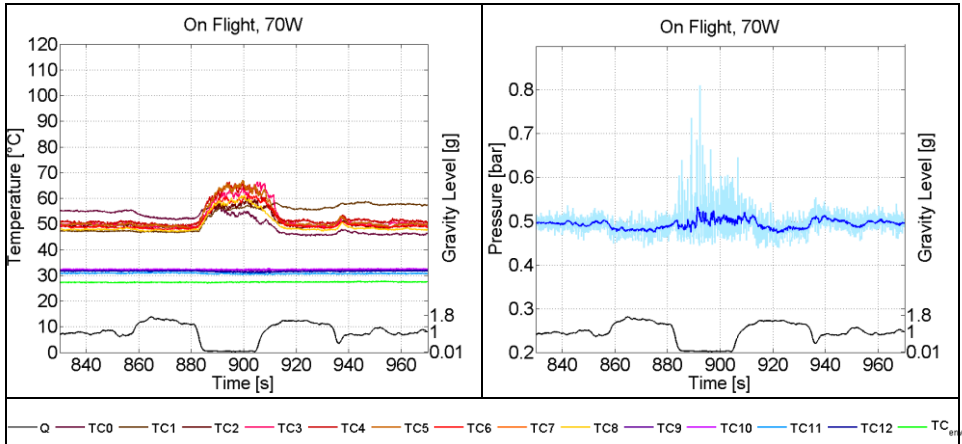
Figure 4.18: Flight experiments, vertical configuration at 70W. On the left, tube wall temperatures; on the right, local fluid pressure. Solid lines represent the filtered data, colored ranges the non filtered pressure. For thermocouples positions refer to Figure 3.2.

Figure 4.19: Flight experiments, vertical configuration at 80W. On the left, tube wall temperatures; on the right, local fluid pressure. Solid lines represent the filtered data, colored ranges the non filtered pressure. For thermocouples positions refer to Figure 3.2.

Figure 4.20: Flight experiments, vertical configuration at 90W. On the left, tube wall temperatures; on the right, local fluid pressure. Solid lines represent the filtered data, colored ranges the non filtered pressure. For thermocouples positions refer to Figure 3.2.

Figure 4.21: Flight experiments, vertical configuration at 100W. On the left, tube wall temperatures; on the right, local fluid pressure. Solid lines represent the filtered data, colored ranges the non filtered pressure. For thermocouples positions refer to Figure 3.2.

Probably, all these phenomena happen because, statistically, it is easier for the 70% PHP to have liquid in the evaporator turns. Thus dry-out requires higher powers, while generation of new vapor elements is never damped even when the lack of gravity does not help the flowing of the liquid phase from the condenser downward the evaporator zone. The disequilibrium linked to evaporation processes guarantees the global fluidic motion.

PART II

THEORETICAL MODELLING
and
NUMERICAL SIMULATIONS

5. Numerical modelling of PHPs: state of the art

In spite of the significant efforts of the last two decades, at the present no comprehensive tools exist to aid engineers in designing PHPs. Indeed, many numerical works has been proposed by researchers from all over the word, but only few of them are capable of complete thermal-hydraulic simulations and even less are partially validated against experimental data [1] [34] [35]. In addition, none of

the existing models is validated for transient operations or for various gravity levels, even if modified gravity conditions commonly arise in several applications, from automotive to aerospace, from material synthesis to chemistry.

Most of the models appeared so far in the literature (see Table 5.1) can be categorized in five different classes accordingly to the adopted simplification scheme:

1. Continuum wave propagation approach, which assumes pressure oscillations as fundamental to induce vapor-liquid circulation.

2. Spring - mass - damper approach: the PHP is compared to single or multiple spring - mass - damper systems. Such kind of models may either describe only the kinematics of the fluidic elements without considering any heat transfer characteristics, or, either, they may define the properties of the equivalent mechanical elements as influenced by heat transfer.

3. Lumped parameters approach: the PHP is described using the first principles by applying fundamental equations of mass, momentum and energy to specified control volumes. This is largely the most adopted approach.

4. Artificial Neural Networks (ANN), which is an example of nonlinear, statistical data modelling inspired by the structure, functional aspects and learning capability of human brains.

5. 2D or 3D Volume Of Fluid (VOF) approach, which is one of the most popular interface capturing technique among the Computational Fluid Dynamics (CFD) methods.

With the exception of the last two groups, usually all the works focused on slug flow since this is the primary flow pattern in PHPs.

Principal Investigator	Year	Type of Approach	PHP Layout	Validation	Conclusions
Miyazaki et al. [36]	1996	Wave propagation	Closed tube PHP	Fairly good	Optimized filling ratio for bottom and top heat modes are 70% and 35%, respectively. A symmetrical wave is obtained at proper charge ratio.
Miyazaki et al. [37]	1998	Wave propagation	Closed loop PHP and closed ends PHP	Fairly good	The progressive wave for a closed-loop channel and the standing wave for a closed-end channel can be obtained from the wave equation.
Hosoda et al. [38]	1999	Lumped parameters	Closed tube PHP	Poor	Liquid and vapor flow is simulated as 1D. Numerical results for pressure are higher than the experimental data, but oscillations are reproduced.
Zuo et al. [39]	1999	Spring-mass-damper	Closed flat plate sintered PHP	Poor	The wick structure distributes liquid evenly, and reduces local temperature fluctuations.
Wong et al. [40]	1999	Spring-mass-damper	Open-ends PHP	-	The pressure pulse induces oscillations but is damped out by friction between the liquid and pipe wall.
Dobson et al. [41]	1999	Lumped parameters	Unlooped with open ends PHP	Poor	Evaluation of the thrust produced by the system.

Swanepoel et al. [42]	2000	Lumped parameters	Open and closed tube PHP	Qualitative	The model revises Dobson's approach. he initial length of the plug, the thickness of the liquid film and the interfacial mass flux have a strong influence on the final results and need to be better modelled to obtain more reasonable predictions.
Maezawa et al. [43]	2000	Chaos analysis	Single loop PHP	-	Chaotic dynamics governs the flow over a wide range of heat transfer rates
Zuo et al. [44]	2001	Spring-mass-damper	Closed flat plate sintered PHP	-	Experiments show that performance of a PHP is sensitive to the filling ratio. Numerical results were not reported.
Shafii et al. [45]	2001	Lumped parameters	Open and closed PHP	-	Heat is transferred principally by sensible heat. Latent heat serves only to drive oscillating flow. Negligible effect of gravity.
Shafii et al. [46]	2002	Lumped parameters	Open and closed PHP	-	Heat transfer is due mainly to the exchange of sensible heat. Higher surface tension results in a slight increase in the total heat transfer. No operation for high charge ratio.
Zhang et al. [47]	2002	Lumped parameters	U-shape miniature channels	-	Overall heat transfer is dominated by sensible heat. Frequency and amplitude are not affected by surface tension.
Khandekar et al. [48]	2002	ANN	Closed tube PHP	Good	ANN is trained by experiments. Effects of diameters, number of turns, length, inclination angle, and fluid properties are not accounted for in the model.

Ma et al. [49]	2002	Spring-mass-damper	Open tube PHP	Poor	Various ranges of operational temperature are studied. The model under-predicts temperature drops.
Zhang et al. [50]	2002	Lumped parameters	Closed PHP	-	The amplitude and frequency of oscillation are correlated to the heat transfer coefficients and temperature difference.
Dobson [51]	2003	Lumped parameters	Unlooped open ends	Poor	The numerical model drastically over-predicts the mass fluxes.
Zhang et al. [52]	2003	Lumped parameters	Open PHP	-	Amplitude and circular frequency decrease with heating and cooling lengths reduction. Higher filling ratios enhance circular frequency while decrease amplitude.
Sakulchang-satjatai et al. [53]	2004	Lumped parameters	Open and closed tube PHP	Good	Model is same as [45] and [47] [50]. The predicted heat transfer rate is compared to experimental results in literature.
Dobson [54]	2004	Lumped parameters	Unlooped with open ends PHP	-	The dominating forces for liquid plug motion are vapor pressure difference, friction and gravity.
Liang et al. [55]	2004	Spring-mass-damper	-	-	Isentropic bulk modulus generates stronger oscillations than isothermal bulk modulus.
Dobson [56]	2005	Lumped parameters	Unlooped with open ends PHP	-	The theoretical model is able to reflect the complex non-linear behaviour of the system. A water pump which makes use of open oscillatory heat pipe is not suitable for pumping water for agricultural purposes.

continue

Holley et al. [57]	2005	Lumped parameters	Close, wicked, tube PHP	-	Varying diameter between parallel channels induces flow circulation and may increase heat transfer capacity. Bottom heat mode performed better than top heat mode. Sensitivity to gravity decreases when increasing the number of channels.
Kim et al. [58]	2005	Lumped parameters	Open PHP	-	The model is the same as [45] with different evaporation/condensation correlations. Diameters, filling ratios and surface tension have strong effects of the PHP performance.
Ma et al. [59]	2006	Spring-mass-damper	-	-	Oscillating motion depends on the filling ratio, the PHP length and diameter, the evaporator/condenser temperature difference, the working fluid, and the operating temperature.
Ma et al. [60]	2006	Similar to ANN	Close tube PHP	-	Results indicated that the effect of the inclination angle on the heat transfer rate was the most significant, followed by the effects of the heat input and the charging ratio. Many other issues have not been considered in their model.
Khandekar et al. [61]	2007	CFD	Embedded Flat Plate PHP	-	Embedded PHP can be beneficial only if the conductivity of the plate is low.

Qu et al. [62]	2007	Start-up models	Open ends PHP	-	The cavity sizes on the capillary inner surface strongly affect PHPs start-up performance, which can be also improved by selecting appropriate working fluids.
Sakulchang-satjatai et al. [63]	2008	Lumped parameters	Open and closed tube PHP	Good	Probably the first model that has been validated both qualitatively and quantitatively.
Khandekar et al. [64]	2008	Lumped parameters	Closed loop PHP	-	The effective thermal resistance can be achieved adopting correlations for convective boiling and condensation in the respective PHP sections.
Givler et al. [65]	2009	VOF	Tube PHP	-	Some qualitative trend and image is shown but the model validation is absent.
Song et al. [66]	2009	Auto-correlations approach	Closed tube PHP	-	PHP are deterministic chaotic, non periodic or random systems.
Lee et al. [67]	2009	ANN	Closed tube PHP	Good	The trained model should be tested with other experimental data to check the its consistency.
Chen et al. [68]	2009	ANN	Closed tube PHP	Good	Although the predicted results follow the measured data well, the physical interpretability of the model is lost.
Liu et al. [69]	2009	VOF	Close tube PHP	-	Under various working conditions, the proposed model can simulate the initial distribution of the working fluids as well as different flow patterns including bubbly-, slug-and annular-flow.

continue

Yuan et al. [70]	2010	Lumped parameters	Tube PHP	-	The gravity effect could be reasonably demonstrated by a forced vibration on a single degree of the freedom system with viscous damping.
Das et al. [71]	2010	Lumped parameters	Single tube	-	Evaporation/condensation models explain the large amplitude oscillations observed experimentally.
Nikolayev [72]	2011	Lumped parameters	Fluid only	-	The model reproduced some of the experimentally observed functional regimes of PHPs, but equations for the tube wall were missing.
Hemadri et al. [73]	2011	CFD	Embedded PHP	-	The advantage of any enhanced thermal conductivity device embedded in a radiator plate decreases if the thermal conductivity of this device surpass a particular value.
Mameli et al. [20] [74] [75]	2012	Lumped parameters	Close tube PHP	Good	Predicted liquid momentum, maximum tube temperature and equivalent thermal resistances were in good qualitative and quantitative accordance with the experimental data given in literature.
Xu et al. [76]	2012	VOF	Flat plate PHP	-	Micro-grooves embedded in the evaporator section improve the heat transfer of a PHP.
Chiang et al. [77]	2012	Spring-mass-damper	Closed loop PHP	-	PHPs with non-symmetrical structure, low filling ratio, high operating temperature and evaporator/condenser temperature difference can achieve good performance due to large oscillatory motions.

Nikolayev [78] [79]	2013	Lumped parameters	Single branch PHP	-	Both evaporation and condensation are vital for the oscillation start-up which is controlled by the temperature difference between the evaporator and the condenser.
Dilawar et al. [80]	2013	Lumped parameters	Capillary U-shaped channel	Poor	Pressure losses at the bends result in a marginal reduction in the amplitude of oscillation; gravity and inclination have no effects on the amplitude and frequency of liquid slug oscillations.
Rao et al. [81]	2013	Thermal transport in liquid film	Oscillating meniscus	-	There is a high probability of existence of metastable states, which essentially point towards considering non-equilibrium evaporation and condensation models for predicting the film thermal transport for an oscillating meniscus.
Sarangi et al. [82]	2013	Lumped parameters	U-shape channel	-	Sensible and latent heat transfer rates were 93% and 7% of the total heat respectively. Spatial and temporal film thickness variation is small (1-3%).
Senjaya et al. [83]	2013	Lumped parameters	Closed loop PHP	-	The overall performance of the oscillating heat pipe increases significantly due to bubble generation and growth.
Lin et al. [84]	2013	VOF + Mixture Model	Miniature PHP	Poor	Fluent unsteady mixture model is more suitable for the two-phase flow simulations of PHPs being able to reproduce even bubbles generation and oscillations caused by the pressure difference.

Nagwase et al. [85]	2013	VOF	Close loop PHP	Fairly good	The unsteady Star CCM+ VOF model is able to reproduce vapor generation in the evaporator region. The PHP heat transfer is caused by fluidic oscillations.
Kim et al. [86]	2013	Lumped parameters	U-shaped channel	-	Amplitude and frequency of operative temperature fluctuations acts on liquid position, vapor temperatures/pressures, and heat transfer performance.
Kim et al. [87]	2014	Lumped parameters	Single turn PHP	Fairly good	Dual-diameter tubes help to promote a circulating flow in the PHPs.
Rudresha et al. [88]	2014	CFD	Close tube PHP	Poor	The thermal resistance of a PHP charged with water and nano-particles decreases when the additive concentration increases.
Senjaya et al. [89]	2014	Lumped parameters	Closed loop PHP	-	Non-condensable gasses disturbed condensation phenomena in PHPs, reducing the performance of the device.
Yin et al. [90]	2014	Wave propagation	Single loop PHP	Good	Depending on the working fluid and on the operation temperature, PHPs have different best filling ratios.
Yang et al. [91]	2014	Meta-heuristic	PHP	Good	During optimization, the least-squares approach is not sufficient to obtain accurate results and extra proper constraints should be imposed.

Table 5.1: Summary of the principal theoretical and numerical works proposed on PHPs in the last 20 years [1] [92].

In the following, the principal works will be summarized to point out their strengths and weaknesses.

5.1 Continuum wave propagation approach

The first attempts to model PHPs arose few years after the patent registration in the early '90. Basing on experimental observations, Miyazaki and Akachi [36] [37] proposed a simple analytical model of self-exciting sinusoidal waves to explain the importance of pressure oscillations on sustaining the fluidic motion. They derived the wave equation assuming a reciprocal excitation of void fraction, representative of the oscillatory flow, and pressure. In addition they concluded that an optimal filling ratio exists for each PHP: proper charging will generate a symmetrical pressure wave, while if the filling ratio is too high, the PHP will experience a gradual pressure increase followed by a sudden drop; on the other hand, scarce charging will cause chaotic pressure fluctuations. One year later Miyazaki and Arikawa [93] experimentally investigated the oscillatory flow in PHPs measuring the wave velocity, which resulted in fairly agreement with the previous predictions.

Following the same approach, recently Yin et al. [90] studied the influence of the filling ratio during the PHP start-up. The mathematical model was derived focusing on the pressure-wave speed which varies when passing from liquid to vapor phase. Results showed that the heat input needed to start-up oscillations increases with the filling ratio. Furthermore, there exists an upper limit of the filling ratio which depends on the chosen working fluid.

5.2 Spring - Mass -Damper approach

Zuo et al. [39] [44] developed a detailed model for the temporal displacement of the liquid slugs, lately updated with a heat transfer section. They modelled a PHP by comparing it to an equivalent single spring-mass-damper system which properties are affected by the heat transfer. Even if the viscous damping is forced equal to zero, the solution of the differential equation suggested that the spring stiffness coefficient is increasing in time for the entire range of the tested filling ratios; thus the amplitude of the oscillations were expected to decrease as long as the simulations proceed. Unfortunately, this is in contradiction with steady oscillations experimentally observed in PHPs operations. Furthermore it is not clear how a model describing a smooth tube PHP can be validated against data coming from a flat plate PHP with embedded porous wick.

Wong et al. [40] in the same year modelled an open-loop PHP by considering it as a multiple spring-mass-damper system. Since adiabatic conditions are assumed for the entire PHP, a sudden pressure pulse was applied to simulate local heat input into the vapor plugs and sustain the motion. In addition minor friction losses, gravity and capillary effects have been neglected. The effect of imposed pressure pulses on the system was studied and results of parametric analysis with respect to slug lengths and filling ratios were presented. However, the oversimplifications cannot be ignored and in this light, the model has limited applicability.

The last researchers who have tried to use the spring-mass-damper approach to simulated PHPs were Ma et al. [49] [59] and Liang et al. [55]. They presented a mathematical model to describe the oscillation characteristics of slug flow in a capillary channels. The numerical results, obtained with different techniques, indicated that

the isentropic bulk modulus generates stronger oscillations than the isothermal bulk modulus. In addition the authors demonstrated that the capillary tube diameter and the bubble size are determining the oscillation, while the capillary and gravitational forces, as well as the working fluid initial pressure distribution, significantly affect the frequency and amplitude of the oscillating motion. Unfortunately, the model under-predicted the temperature difference between the evaporator and condenser when compared to experimental results [49]. This model has, recently, been updated by Chiang et al. [77] who developed an analytical model to predict the oscillation motion in horizontal PHPs with and without asymmetrical channels disposition. Results showed that PHPs with non-symmetrical structure, low filling ratio, high operating temperature and evaporator/condenser temperature difference could achieve better performance due to the stronger oscillatory motion established with respect to symmetrical PHPs. However the model was not validated against any experimental work and presented many simplifications (e.g. negligible bend pressure losses, adiabatic conditions, negligible influence of the liquid film and the constant capillary force along the flow path).

5.3 Lumped parameters approach

Hosoda et al. [38] proposed one of the first theoretical approaches based on the resolution of the first principles. The simplified numerical model solved liquid momentum and energy balances neglecting the film presence, as well as the friction between the tube and the working fluid and phase changes; any equations were developed for the vapor phase. Experimental data were used to set both initial and boundary conditions. Even if the model over-

predicted vapor pressure, it showed that propagation of vapor plugs induced fluid flow in the capillary tubes.

Dobson and Harms [41] investigated a PHP with two open ends for boat movements. The fluid inside the tube consisted in central liquid slug surrounded by vapor. The liquid is assumed adiabatic, while a numerical solution of the vapor energy equation and the liquid momentum was presented to predict temperature, position, and velocity. Lately, the study of open ends PHPs in conjunction with check valves was extended to water pumping [51] [54] [56]; however it was concluded that such kind of system is not suitable for agricultural purposes, because of the attainable limited mass fluxes. An improved model for liquid slug oscillations that considered pressure difference, friction, gravity, and surface tension was also presented. Dobson's approach was revised one year later by Swanepoel et al. [42]: the governing equations (mass, momentum and energy) have been applied to both vapor and liquid; also the film has been taken into account. However, the comparison with ad hoc experiments underlined that the theoretical model was able to predict only qualitatively the dynamic of the system. The authors concluded that the initial length of the plug, the thickness of the liquid film and the interfacial mass flux have a strong influence on the final results and need to be better modelled to obtain more reasonable predictions.

Zhang et al. first analytically investigated oscillatory flow in both U-shaped miniature channels [50] and closed-end PHP with an arbitrary number of turns [52]; later they proposed models for heat transfer in the evaporator and condenser sections of PHPs with one open end by analyzing the film evaporation and condensation which drive oscillatory flow in PHPs [52]. It was found that the overall heat transfer is dominated by the exchange of sensible heat, not by the exchange of latent heat.

Similar results have been achieved by Shafii et al. [45] who developed a lagrangian theoretical model to simulate the behaviour of liquid slugs and vapor plugs in both closed- and open-loop PHPs later improved including an analysis of boiling and condensing heat transfer in the thin liquid film separating the liquid and vapor elements [46]. The model computed pressure, temperature, plug position and heat transfer rates. The most significant conclusion, in fact, was that the majority of the heat transfer (~95%) is due to sensible and not to latent heat, which, otherwise, serves only to drive the oscillating flow. In addition the model showed that gravity has no significant effect on PHPs performance and that the total number of vapor plugs always reduced to the total number of heating sections in few seconds: these final observations, however, are in contrast with the experimental evidences.

Few years later, basing on flow visualizations, Sakulchangsatjatai et al. [53] [63] updated the previous works by Shafii et al. [45] and Zhang et al. [47] [50] by adding empirical assumptions to the nucleate boiling frequency, bubble length and liquid film thickness. Qualitative and quantitative validations have been given for evaporator temperatures, inclination angles and input heat fluxes.

However, it was only in 2005 that Holley and Faghri [94] developed one of the most comprehensive numerical models concerning a PHP system. It was a one dimensional lumped parameter model of a water PHP with sintered wick. It assumed a priori, slug flow and saturated conditions. The momentum equation was solved for liquid slugs, while the energy equation was considered for both phases and for the external wall. The model was able to account for liquid elements coalescence and new vapor formation although phase changes are not directly accounted for. The effects of the varying channel diameter, inclination angle, and number of parallel channels were presented: when one channel was of a smaller

diameter, it induced the circulation of the fluid which in turn increased the heat load capability of the PHP; as the number of parallel channels increases, the PHP sensitivity to gravity decreases and its heat load capability increases; the modelled PHP performed better in the bottom heat mode than the top heat mode. Later Mameli et al. [20] [74] [75] improved this model introducing the effects of the tube bends on the liquid slugs dynamic and the calculation of the two-phase heat transfer coefficient for liquid and vapour sections as function of the heating regime. Furthermore, an extended library of possible working fluid was included. Closed loop PHPs have been simulated under different working conditions, such as different working fluids like ethanol, R123 and FC-72, different number of turns, different inclination angles as well as different heat fluxes at the evaporator. Although the simulation results of the liquid momentum, the maximum tube temperature and the equivalent thermal resistances were in good qualitative and quantitative accordance with the experimental data given in literature, further direct experimental validations are still in demand to test the practical application of the numerical models. Nevertheless, Holley and Faghri as well as Mameli's model represent, up to now, the best tools for PHPs modelling available in literature.

Khandekar et al [64] in 2008 suggested a novel lumped parameters model for single loop PHP. The authors concluded that the effective thermal resistance can be simply achieved by implementing correlations for convective boiling and condensation in the respective PHP sections; however, the assumption of homogeneous fog-flow seems more suitable for thermosyphons with respect to PHPs.

In 2010 Yuan et al. [70] proposed a model for the fluid flow and heat transfer characteristics of the liquid slug and the neighbouring vapor plugs in PHPs. A new energy equation for the liquid slug was

proposed by the aid of the Lagrange method and the latent heat was used as the outer heat input in the vapor energy equation. The authors concluded that the gravity effects could be reasonably reproduced by applying a forced vibration on a single degree of the freedom system with viscous damping. However, the following year, Nikolayev [95] showed that the proposed energy equation was wrongly derived by the fundamental principles.

In the same year, basing on Shafii's work [45], Das et al. [71] developed an evaporation/condensation model of single liquid/vapor element able to explain the large amplitude oscillations observed experimentally. Later Nikolayev [72] updated this attempt in order to treat an arbitrary number of bubbles and branches. The author proposed the use of an object oriented method which represented a step forward with respect to previous codes. Several phenomena occurring inside PHPs have been taken into account, such as coalescence of liquid plugs and film junction or rupture; in addition even the liquid film dynamic was account for: the film dynamic has been considered vital to correctly represent the vapor heat exchange. However, even if the model reproduced some of the experimentally observed functional regimes of PHPs, like chaotic or intermittent oscillations of large amplitudes, equations for the tube wall, as well as quantitative validations of the numerical data were missing. Few years later, in two novel works, analyzing the start-up conditions of a single branch PHP with no adiabatic section [78] [95], Nikolayev concluded that both evaporation and condensation are essential for the oscillation start-up which is controlled by the temperature difference between the evaporator and the condenser. The analysis on dried-out sections also revealed that fluids with low gas heat conductivity should be chosen for PHPs. Unfortunately, even this time quantitative validations were missing and the author justify complaining about the scarcity of the experimental data.

Dilawar et al. [80] proposed a non-isothermal model by considering saturation temperature at the liquid vapor interface in calculating the phase change, mass and heat transfer instead of the vapor temperature as usually considered in earlier isothermal models. Pressure losses at the bends and capillary effects at the meniscus were also incorporated. The main conclusions were that bend pressure losses, as well as gravity and orientation, result in a marginal reduction of the oscillation amplitudes. Nevertheless, vertical PHPs perform better then horizontal devices. In addition, thermal performance has been observed to reduce considerably with increasing adiabatic lengths.

Sarangi et al. [82] proposed a mathematical model for the hydrodynamics and heat transfer in a U-shaped PHP heated from the top. Only one liquid slug and two vapor plugs have been taken into account. Unlike most of all the other models, the vapor status has been checked and if the fluid was in superheated conditions pressure is calculated using the ideal law of gas instead of imposing saturation. Moreover, the metastable state of vapor was incorporated by means of a modified latent heat term. The heat transfer coefficient was related to liquid film thickness spatial variation which was calculated considering phase changes across its interface. The authors studied different parameters, such as liquid velocity, vapor pressure, thermal conductivity, etc. They concluded that the film thickness variation is very small, ranging from 1-3% of its initial value; in addition it was stated that the sensible and latent heat transfer rates were 93% and 7% of the total heat respectively. This last result agrees with previous analysis available in literature [46] [52]. Even if the model provides some novelties, it requires a global revision in order to be extended to a complete PHP since only three fluidic elements have been accounted for. In addition no experimental validation has been provided yet.

In the same year, Senjaya et al. [83] proposed simulations of oscillating heat pipe with and without bubble generations to investigate the effects of nucleation on liquid slugs, vapor plugs and liquid films dynamics. Bubbles were generated with constant initial length in fixed nucleation sites. Results showed that bubble generations cause large pressure differences between two neighbouring vapor plugs inducing oscillations of large amplitude and frequency which increase due to continuous nucleation. These phenomena affected the way of heat transfer reducing the sensible heat (74%) and increasing the latent heat (26%). Without bubbles generation, instead, the model was able to reproduce Shafii's results [46]. The same model was later used to show that non-condensable gasses reduce the performance of PHPs [89].

5.4   Artificial Neural Network

An artificial neural network is a mathematical model inspired by the structure and functional aspects of biological neural networks. Although similar to linear regression analysis, neural networks are distinguished for utilizing non-linear mathematics and, therefore, it can be used to model highly complex and non-linear functions unachievable by traditional means. Such kinds of networks are usually used to model complex relationships between inputs and outputs or to find patterns in data. The main disadvantage of using an ANN is that it requires a large diversity of training examples from real-world operation. Another drawback is that the algorithms are not linked to the physical phenomena, hiding the dynamics of the system, and, therefore, it can only give predictions in the range of the training experimental data. In 2002, for the first time, Khandekar et al. [34] [48] proposed the use of ANN models to develop design-oriented tools for PHPs. They used a fully connected feed forward

ANN trained using 52 sets of experimental data from a closed-loop PHP. The ANN is fed the heat input and filling ratio of each data set and calculates the effective thermal resistance of the device. However, many parameters, such as the diameter, the number of turns, the channels length, the inclination angle, the working fluid, etc. have been neglected. After this first attempt, other researchers followed the opened path [67] [68]. However, all the models showed these same basic drawbacks.

5.5   Volume Of Fluid

Recently attempts to model PHPs making use of CFD/VOF commercial or in-house codes, appear in literature [61] [65] [69] [88] [76] [84] [85] [73]. However, even if this approach might achieve high modeling potential in the near future, the work presented up to now are of global low scientific level and generally all of them lack of experimental validation.

Chapter 6

6. A novel lumped parameter numerical model

Chapter 5 has shown that, although PHPs have become a hot topic in the last years, the mechanism of their fluid flow and heat transfer capacity have not yet been well understood and modelled [35]. Nevertheless, numerical analyses appear essential to help and support the experimental research in order to enlarge the present knowhow, level up the current TRL and encourage a larger industrial use.

Thus, following the route opened by Holley and Faghri [94] and Mameli et al. [75] [74] [20], an advanced, novel, non-equilibrium, lumped parameter numerical model able to simulate PHPs thermal-hydraulic behaviour has been developed. It revises and improves the above mentioned works, aiming to represent a step forward in the present modelling ability. Besides, even if lumped parameter models are not a novelty, for the first time this kind of numerical tools has been applied to simulate transient operative conditions removing physical simplified assumptions and embedding directly phase changes processes. In addition, an advanced numerical technique has been implemented to allow fast simulations and, consequently, extended sensitivity analysis and device designs.

The code has two main blocks: an Eulerian model for the external tube and a Lagrangian model for the internal two-phase flow. A dedicate matrix allows communication between fix and moving domains. The final mathematical models results in an ODE (Ordinary Differential Equations) system which is solved numerically by means of a blocked algorithm consisting of a combination of Adams Bashforth methods of order one and two with the Störmer-Verlet method. The use of the latter method for the discretization of the system block descending from the momentum equation was driven by its well known properties in capturing the long term dynamics of second order ODE systems in an accurate and stable way. Such choice, which represents a novelty with respect to the previous simulation tools, has been shown to be extremely effective in preventing unphysical phenomena such as the overlapping of adjacent fluidic domains.

For the implementation of the numerical method an interpreted code written in GNU Octave was chosen in order to allow for agile development of model modifications and extension; by suitably optimizations, its efficiency has been already enhanced to reduce

global simulation time to a level comparable with more complex tools.

The numerical method and the implemented code have finally been validated against experimental data in several operative conditions and transient gravity levels: the results have a very good matching with the actual thermo-physical behaviour of the system.

6.1 Theoretical model

The proposed numerical tool is a lumped parameters one-dimensional model applicable to a confined operating regime (i.e. slug flow) for a PHP of constant diameter and for a negligible liquid film thickness around the vapor plugs (Figure 6.1).
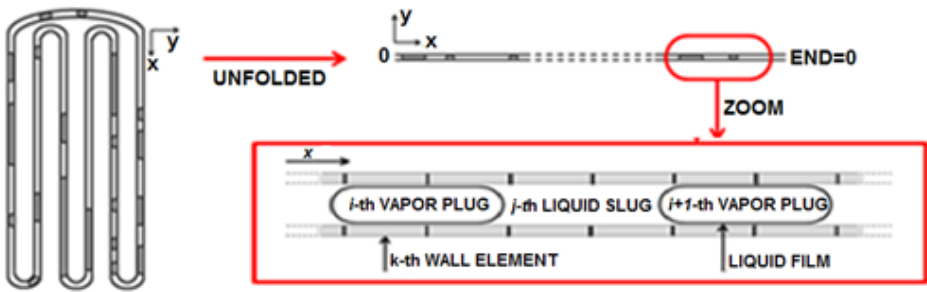
Figure 6.1: Schematic of the numerical domains. The bended PHP has been unfolded in a single straight channel and subdivided into solid and fluidics regions. The liquid slugs sub-domains are not explicitly indicated. The walls are considered completely wettable.

The principal assumptions are:
1. The model is one-dimensional. Mass, momentum and heat transfer are calculated along the axial direction, which follows the PHP tube. Heat transfer in radial direction is lumped.
2. All the fluid thermo-physical properties, apart from vapor pressure and density, are calculated as function of the

temperature only [96]. Wall thermal properties are kept constant. Liquid is assumed incompressible.

3. The momentum equation for each liquid slug is lumped and friction between vapor plugs and wall elements is neglected.
4. Liquid menisci maintain hemi-spherical shape with zero contact angles at the wall[13].
5. Vapor is treated as real gas (Van der Waals equation) except in case of phase changes. Density is calculated by definition (mass over volume).
6. Vapor may exist in saturated, super-heated and sub-cooled conditions.
7. Heterogeneous phase changes are isothermal and isobaric; phase changes through the interface are isobaric but non-isothermal. Phase changes are always followed by isothermal compressions or expansions of the vapor elements in order to re-adjust the total volume.
8. The thin liquid film around each vapor plug is neglected. It is only used to define the real volume occupied by fluidic elements within the tube inner channel, considering it constant in space and time.
9. The temperature jump through the interface is neglected.

6.1.1   The solid model

The solid model describes the thermal behaviour of the PHP external wall. The capillary tube is sub-divided into N_w smaller domains with constant length (Figure 6.1) which are treated with an Eulerian approach, since the mass of the tube and the positions of the wall domains are not time dependent. A set of N_w differential equations, describing the temperature evolution of each solid

---

[13] Even though the pressure drop due to the contact angle hysteresis may be orders of magnitude lower with respect to the other terms in the momentum equation, in any case it may affect the fluid motion and the PHP start-up because it introduces local instabilities in the systems and should be further investigated.

element, has been implemented and solved making use of the 1st Adams–Bashforth integration scheme [97].

Accounting for assumption 2, the wall balances can be defined as:

$$\begin{cases} dm_w = 0 \\ m_w dw_w = 0 \\ m_w c_{V,w} \dfrac{dT_w}{dt} = \left(k_w A_w \left. \dfrac{\partial T_w}{\partial x} \right|_k^{k-1} - k_w A_w \left. \dfrac{\partial T_w}{\partial x} \right|_{k+1}^{k} \right) - q_{wf,w} A_{wf} + q_{ex} A_{ex} \end{cases} \tag{6.1}$$

where m, w, U and T are respectively mass, velocity, internal energy and temperature of each domain, k_w is the thermal conductivity of the wall material, A_{wf} and A_{ex} are relatively the internal tube surface in contact with the fluid and the external tube surface exposed to the environment, while $q_{wf,w}$ and q_{ex} represents the heat exchanged with fluidic elements and with the external environment; A_w is the tube cross section area, as shown in Figure 6.2.
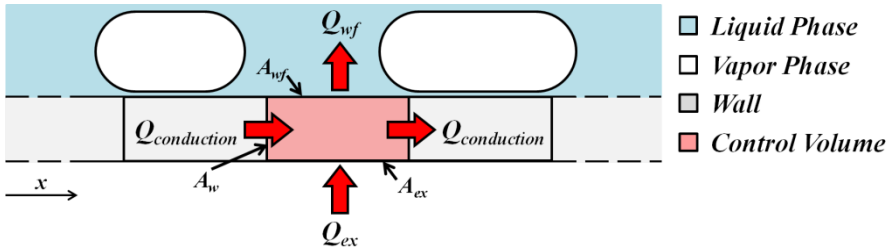
Figure 6.2: Schematic of the wall energy balance for the k-th domain.

The third row of Equation (6.1) represents the energy balance. The first term on the right side accounts for the heat conduction within the wall; the second term is the heat exchanged between the wall and the fluidic elements (section 6.1.3); the last term represents the heat exchanged between the wall and the external environment. Constant heat input power Q_{ex} is supplied to the evaporator zone,

forced convection is applied at the condenser, while no heat exchange occurs in the adiabatic region:

$$q_{ex} = \begin{cases} Q_{ex}/A_{ex} & \textit{evaporator zone} \\ 0 & \textit{adiabatic zone} \\ htc_\infty(T_\infty - T_w) & \textit{condenser zone} \end{cases} \tag{6.2}$$

where htc_∞ is the external heat transfer coefficient and T_∞ the environmental temperature.

Radiation has been neglected since it is estimated less than 0.5% of the total dissipated heat in the worst case for the considered experimental conditions.

6.1.2   The fluidic model

The PHP internal dynamics depends on the interplay between vapor and liquid. Since a confined flow is assumed a priori, the fluidic elements are an alternation of N_j liquid slugs and N_i vapor plugs. (Figure 6.1); the number and the dimensions of these fluidic batches are allowed to vary during the simulation time as long as the total mass and length of the system are conserved. The associated thermo-dynamic behaviour is described by means of the fluidic model; the most critical hypothesis of the simulation is that a negligible liquid film thickness has been introduced, thus the liquid film (which is observed in the experiments, [98] [99]) is not accounted in the following mathematical calculations (Assumption 8).

Since only slug flow is considered, when a Lagrangian approach is applied, liquid slugs and vapor plugs constitute physical control volumes; thus, each fluidic element is characterized by a proper mass, temperature and velocity and its oscillating position in the capillary channel can be tracked during the whole simulation time. Moreover liquid slugs are subdivided into smaller sub-domains (liquid slices with equal length), having the same velocity, but different

temperatures accounting for the axial heat conduction within the liquid phase.

Mass, momentum and energy balances are solved for liquid and vapor through a novel hierarchical method: for each time step, first the heterogeneous phase changes are solved, then the homogenous evaporation/condensation phenomena through the interface are accounted for, finally all the other phenomena (e.g. sensible heat exchange with the wall, axial conduction, etc.) are computed. The next sections will explain these three different steps.

The 1st Adams–Bashforth integration scheme has been adopted to integrate mass and energy balances if not differently indicated.

Heterogeneous Phase Changes

Although the whole mass and volume of the system remains obviously constant during the simulation time, the mass and the volume of each liquid and vapor element varies due to phase changes.

Heterogeneous condensation/evaporation occurs when a vapor/liquid comes into contact with a non-fluidic object at lower/higher temperature and, at the same time, vapor/liquid pressure is greater/smaller than the saturation point accordingly to the phase changes diagram (Figure 6.3). This involves heat transfer to/from the solid wall. Thus a proper condition must be satisfied to allow heterogeneous phase changes:

$$\begin{cases} P_v > P_{sat} & \& \quad T_w \leq T_{v,sat} - \Delta T_{cooling} & for\ condensation \\ P_l < P_{sat} & \& \quad T_w \geq T_{l,sat} + \Delta T_{super-heating} & for\ evaporation \end{cases} \quad (6.3)$$

$\Delta T_{cooling}$ and $\Delta T_{super-heating}$ are the temperature difference linked respectively to the nucleation onset and boiling nucleation.

In a vertical bottom-heated mode PHP, for example, heterogeneous condensation usually occurs in the condenser region, where, reasonably, the wall temperature is lower than the vapor one,

while heterogeneous evaporation likely appears in the evaporator region where the wall elements can provide energy to the colder liquid slugs.
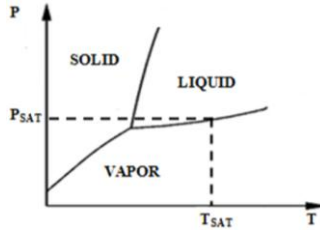
Figure 6.3: Example of a phase change diagram.

Condensation. Figure 6.4 shows in red the global control volume CV adopted to solve mass and energy balances during heterogeneous condensation: it is closed, isochoric and diabatic with respect to the pipe walls. It contains three closed sub-systems, the i-th vapor plug (VP) and two liquid slices (LS), respectively the last and first of the j-th and of the $j+1$-th liquid slug. The closed single vapor sub-domain allows a two-phase change and it is diabatic; the closed liquid sub-domains are mono-phase and adiabatic. The heterogeneous condensation will eventually occur in the vapor plug.
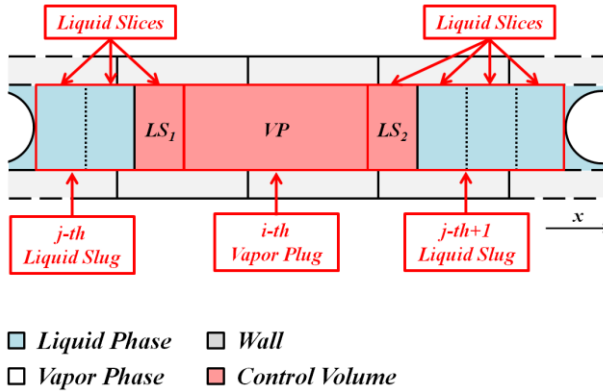
Figure 6.4: Schematic of the fluidic control volumes CV (in red) adopted in case of heterogeneous condensation.

The mass and the energy balances written for the global control volume CV are:

$$\begin{cases} dm_{CV} = 0 \\ dU_{CV} = q_{wf,VP}A_{wf,VP}dt \\ dV_{CV} = 0 \end{cases} \quad (6.4)$$

where V stands for volume.

Since it has been assumed that condensation is isothermal and isobaric (assumption 7), it cannot be isochoric at the same time. Thus, in order to satisfy Equation (6.4), after condensation the vapor element will follow an isothermal expansion to occupy the volume freed by the part of vapor that has become liquid.

The mass and energy balance written for the vapor plug only are:

$$\begin{cases} dm_{VP} = 0 \\ dU_{VP} = q_{wf,VP}A_{wf,VP}dt - PdV_{VP} \end{cases} \quad (6.5)$$

where P stands for vapour pressure.

Since the vapor sub-domain is considered a two-phase system:

$$dm_{VP} = d(m_l + m_v) = dm_l + dm_v = 0 \rightarrow dm_l = -dm_v \quad (6.6)$$

where the subscripts l and v refer respectively to vapor and liquid.

The integration of this last equation in time defined the mass m_{LV} that will change phase in the time step; since vapor undergoes condensation, m_{LV} will be negative:

$$\int_{t_i}^{t_{i+1}} dm_v = m_{v,t_{i+1}} - m_{v,t_i} = m_{LV} \quad (6.7)$$

The energy equation can be explicated as:

$$dU_{VP} = d(U_l + U_v) = Q\,dt - PdV_{VP} = Q\,dt - Pd(V_l + V_v) \quad (6.8)$$

where $Q = q_{wf,VP}A_{wf,VP}$ is the heat exchanged with the solid wall.

Thus, assuming that liquid is incompressible and accounting for the definition of enthalpy ($H = U + PV$):

$$dU_l + dU_v = Q\,dt - PdV_l - PdV_v$$
$$m_l du_l + u_l\rho_l dV_l + m_v du_v + u_v\rho_v dV_v + u_v V_v d\rho_v = Q\,dt - PdV_l - PdV_v$$
$$m_l du_l + m_v du_v + u_v V_v d\rho_v = Q\,dt - (P + u_l\rho_l)dV_l - (P + u_v\rho_v)dV_v$$
$$m_l du_l + m_v du_v + u_v V_v d\rho_v = Q\,dt - \rho_l h_l dV_l - \rho_v h_v dV_v$$
$$m_l du_l + m_v du_v = Q\,dt - h_l dm_l - \rho_v h_v dV_v - u_v V_v d\rho_v$$
$$m_l du_l + m_v du_v = Q\,dt - h_l dm_l - \rho_v h_v dV_v - (h_v - \frac{P}{\rho_v})V_v d\rho_v \qquad (6.9)$$
$$m_l du_l + m_v du_v = Q\,dt - h_l dm_l - \rho_v h_v dV_v - h_v V_v d\rho_v + \frac{PV_v}{\rho_v}d\rho_v$$
$$m_l du_l + m_v du_v = Q\,dt - h_l dm_l - h_v dm_v + \frac{PV_v}{\rho_v}d\rho_v$$

Thus, introducing Equation (6.6) in Equation (6.9):

$$m_l du_l + m_v du_v = Q\,dt - h_{LV} dm_v + \frac{PV_v}{\rho_v}d\rho_v \qquad (6.10)$$

where h_{LV} is the heat of vaporization.

By integrating between the status in t_i and in t_{i+1}, and assuming that the phase change is isothermal and isobaric (assumption 7):

$$m_{LV} = \frac{Q}{h_{LV}}\Delta t = \frac{q_{wf,VP}A_{wf,VP}}{h_{LV}}\Delta t \qquad (6.11)$$

Since m_{LV} is negative, $q_{wf,VP}$ will exit the domain that is expected during condensation.

At this stage, the vapor sub-domain is containing both liquid and vapor. However, the numerical procedure adopted does not allow the existence of fluidic elements with such characteristic, since the starting thermodynamic state of the vapor plug needs to be always with quality equal to one. Thus the condensed mass will be merged

with the adjacent liquid slices paying attention to conserve energy and mass in CV. In addition, in order to be consistent with Equation (6.4), the remaining vapor will undergo an isothermal expansion ($PV_v = cost$).

By solving the mass balance during the merging operation:

$$\begin{cases} m_{LS1,t_i} + m_{VP,t_i} + m_{LS2,t_i} = m_{LS1,t_i} + m_{VP,t_{i+1}} + m_{LS2,t_i} + |m_{LV}| \\ m_{LV} = m_{LV,1} + m_{LV,2} \end{cases} \qquad (6.12)$$

where $m_{LV,1}$ is the mass that will merge with $m_{LS,1}$, while $m_{LV,2}$ is the mass that will merge with $m_{LS,2}$. Thus:

$$\begin{cases} m_{VP,t_{i+1}} = m_{VP,t_i} - |m_{LV,1}| - |m_{LV,2}| \\ m_{LS1,t_{i+1}} = m_{LS1,t_i} + |m_{LV,1}| \\ m_{LS2,t_{i+1}} = m_{LS2,t_i} + |m_{LV,2}| \end{cases} \qquad (6.13)$$

By solving the energy balance during the merging operation:

$$U_{LS1,t_i} + U_{VP,ac} + U_{LS2,t_i} = U_{LS1,t_i} + \left(|m_{LV}|C_{V,l}T_{VP,t_i} + U_{VP,t_{i+1}}\right) + U_{LS2,t_i} \quad (6.14)$$

where the subscripts ac mean "after condensation". Thus:

$$\begin{cases} T_{VP,t_{i+1}} = T_{VP,t_i} \\ m_{LS1,t_{i+1}}C_{V,l}T_{LS1,t_{i+1}} = m_{LS1,t_i}C_{V,l}T_{LS1,t_i} + |m_{LV,1}|C_{V,l}T_{VP,t_i} \\ m_{LS2,t_{i+1}}C_{V,l}T_{LS2,t_{i+1}} = m_{LS2,t_i}C_{V,l}T_{LS2,t_i} + |m_{LV,2}|C_{V,l}T_{VP,t_i} \end{cases} \qquad (6.15)$$

Finally, imposing an isothermal expansion on the remaining vapor (considered ideal) Equation (6.4)is completely satisfied:

$$P_{VP,t_{i+1}}V_{VP,t_{i+1}} = m_{VP,t_{i+1}}R^*T_{VP,t_{i+1}} \qquad (6.16)$$

where R^* is the gas constant. $V_{VP,t_{i+1}}$ should be chosen to satisfy $dV_{CV} = 0$ and thus:

$$V_{VP,t_{i+1}} = V_{VP,t_i} - \frac{m_{LS1,t_{i+1}}}{\rho_l} - \frac{m_{LS2,t_{i+1}}}{\rho_l} \tag{6.17}$$

After this procedure for all the fluidic elements thermodynamic properties are updated to withstand the new thermodynamic status of liquid and vapor elements at $t' = t + \Delta t$.

Evaporation. Figure 6.5 shows in red the global control volume CV adopted to solve mass and energy balances during heterogeneous evaporation: it is closed, isochoric and diabatic with respect to the pipe walls. It contains the *i*-th and the *i+1*-th vapor plugs (VP) and the *j*-th liquid slugs divided into *N* liquid slices (LS). Vapor sub-domains are closed, mono-phase and adiabatic, while liquid sub-domains are closed, diabatic and allow two-phase changes. Thus, the heterogeneous evaporation will occur, eventually, in each liquid slice.
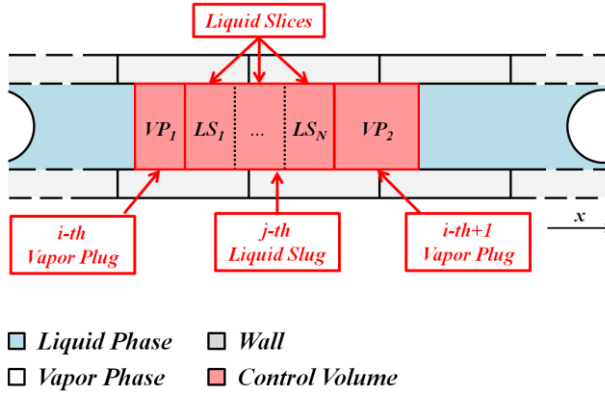
Figure 6.5: Schematic of the fluidic control volumes CV (in red) adopted in case of heterogeneous evaporation.

The mass and the energy balance written on the global control volume VC are:

$$\begin{cases} dm_{CV} = 0 \\ dU_{CV} = \displaystyle\sum_{\xi=1}^{N} q_{wf,LS\xi} A_{wf,LS\xi} dt \\ dV_{CV} = 0 \end{cases} \qquad (6.18)$$

Since it has been assumed that phase changes are always isothermal and isobaric (assumption 7), it cannot be isochoric at the same time. Thus, in order to satisfy Equation (6.18), after evaporation, vapor elements undertake an isothermal compression to guarantee $dV_{CV} = 0$.

The mass and energy balances written for the liquid slug only are:

$$\begin{cases} d \displaystyle\sum_{\xi=1}^{N} m_{LS\xi} = \displaystyle\sum_{\xi=1}^{N} dm_{LS\xi} = 0 \\ d \displaystyle\sum_{\xi=1}^{N} U_{LS\xi} = \displaystyle\sum_{\xi=1}^{N} dU_{LS\xi} = \displaystyle\sum_{\xi=1}^{N} q_{wf,LS\xi} A_{wf,LS\xi} dt - \displaystyle\sum_{\xi=1}^{N} PdV_{LS\xi} \end{cases} \qquad (6.19)$$

Thus:

$$\begin{cases} dm_{LS\xi} = 0 \quad \forall \xi \\ dU_{LS\xi} = q_{wf,LS\xi} A_{wf,LS\xi} dt - PdV_{LS\xi} \quad \forall \xi \end{cases} \qquad (6.20)$$

Since each liquid sub-domain is considered two phase:

$$\begin{cases} dm_{LS\xi} = dm_l + dm_v = 0 \\ dU_{LS\xi} = dU_l + dU_v = Q\, dt - PdV_{LS\xi} = Q\, dt - PdV_l - PdV_v \end{cases} \qquad (6.21)$$

where $Q = q_{wf,LS\xi} A_{wf,LS\xi}$ is the heat exchanged with the solid wall.

Following the same procedure showed for condensation, and assuming incompressible liquid and isothermal and isobaric evaporation, Equation (6.21) yield to:

$$\int_{t_i}^{t_{i+1}} dm_l = m_{l\xi,t_{i+1}} - m_{l\xi,t_i} = m_{LV\xi}$$

$$m_{LV\xi} = -\frac{Q}{h_{LV}}\Delta t = -\frac{q_{wf,LS\xi}A_{wf,LS\xi}}{h_{LV}}\Delta t$$

$$(6.22)$$

This time m_{LV} represents the evaporated liquid mass, thus it is negative. Therefore, $q_{wf,LS\xi}$ enter the domain which is expected during evaporation.

At this stage, each liquid slice is containing both liquid and vapor. However, the numerical procedure adopted does not allow the existence of fluidic elements with such characteristic, since the starting thermodynamic state of the liquid slug needs to be always with quality equal to zero. Thus the evaporated mass will be merged with the adjacent vapor plugs paying attention to conserve energy and mass on CV in this procedure. In addition, in order to make Equation (6.18) true, the vapor elements will undergo an isothermal compression ($PV_v = cost$).

By solving the mass balance during the merging operation, $m_{LS\xi,t_{i+1}}$, $m_{VP1,t_{i+1}}$ and $m_{VP2,t_{i+1}}$ can be inferred:

$$\sum_{\xi=1}^{N} m_{LS\xi,t_i} + m_{VP1,t_i} + m_{VP2,t_i} =$$

$$= \sum_{\xi=1}^{N}\left(m_{LS\xi,t_{i+1}} + |m_{LV\xi,t_{i+1}}|\right) + m_{VP1,t_i} + m_{VP2,t_i}$$

$$(6.23)$$

By solving the energy balance during the merging operation, $T_{VP1,t_{i+1}}$ and $T_{VP2,t_{i+1}}$ can be inferred:

$$\sum_{\xi=1}^{N} U_{LS\xi,ae} + U_{VP1,t_i} + U_{VP2,t_i} =$$
$$= \sum_{\xi=1}^{N} \left[U_{LS\xi,t_{i+1}} + \left(|m_{LV\xi,t_{i+1}}| C_{V,v} T_{LV\xi,t_{i+1}} \right) \right] + U_{VP1,t_i} + U_{VP2,t_i} \tag{6.24}$$

where the subscripts *ae* mean "after evaporation".

Finally, imposing an isothermal compression on the ideal vapor elements Equation (6.18) is completely satisfy:

$$\begin{cases} P_{VP1,t_{i+1}} V_{VP1,t_{i+1}} = m_{VP1,t_{i+1}} R^* T_{VP1,t_{i+1}} \\ P_{VP2,t_{i+1}} V_{VP2,t_{i+1}} = m_{VP2,t_{i+1}} R^* T_{VP2,t_{i+1}} \end{cases} \tag{6.25}$$

where $V_{VP1,t_{i+1}}$ and $V_{VP2,t_{i+1}}$ should be chosen to satisfy $dV_{CV} = 0$. Thus:

$$V_{VP1,t_{i+1}} + V_{VP2,t_{i+1}} = V_{VP1,t_i} + V_{VP1,t_{i+1}} + \frac{\sum_{\xi=1}^{N} m_{LS\xi,t_{i+1}}}{\rho_l} \tag{6.26}$$

After this procedure for all the fluidic elements thermodynamic properties are updated to withstand the new thermodynamic status of the liquid and vapor elements at $t' = t + \Delta t$.

Creation or disappearance of fluidic elements. Heterogeneous evaporation and condensation processes are solved consecutively moving along the fluidic path.

The procedure described above showed mass exchange with the adjacent elements. However, it can occur that a new element is generated if m_{LV} is higher than a minimum value m_{min} computed as the mass of an equivalent sphere which fits perfectly within the tube ($m_{min,eva(cond)} = \frac{1}{6} \pi d_{in}^3 \rho_{v(l)}$); on the other hand, if m_{LV} exceeds the mass of the corresponding element, this one vanishes and the adjacent slugs/plugs merge. The above procedure can be followed

even in these cases, but to guarantee the length conservation, the control volume CV should be chosen adequately (Figure 6.6) to assure that its global dimension does not change during the entire process.
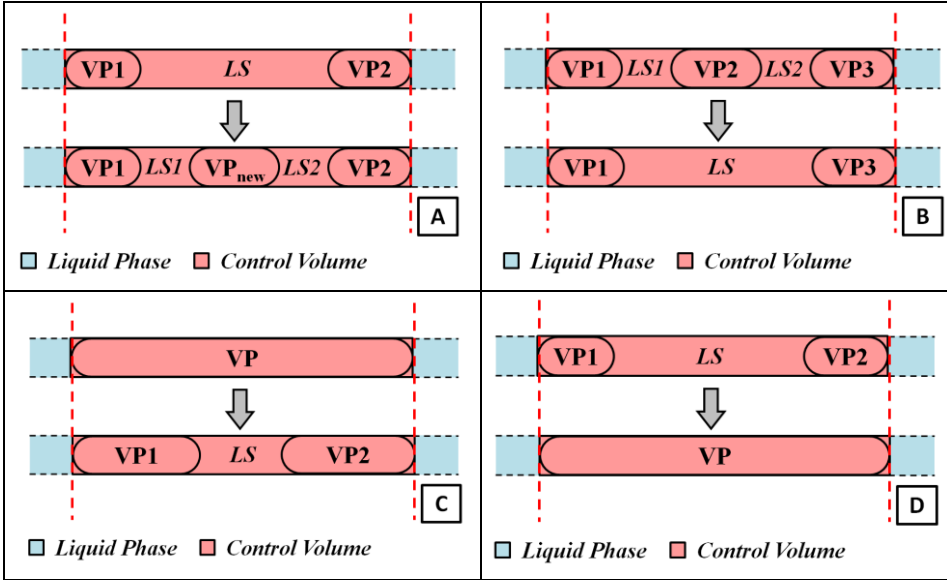
Figure 6.6: Schematic of the fluidic control volumes (in red) adopted in case of heterogeneous evaporation with generation of new a vapor plug (A), heterogeneous condensation with vapor plug disappearance (B), heterogeneous condensation with generation of new a liquid slug (C), heterogeneous evaporation with liquid slug disappearance (D).

Homogeneous Phase Changes on the Interface

Heterogeneous phase changes are computed for all the fluidic elements. Only at this point, on the new fluidic path, evaporation and condensation on the menisci can take place (2nd phase of the hierarchical numerical procedure). In particular, if vapor pressure is higher/lower than the saturation value at its actual temperature, condensation/evaporation on the menisci occurs in the fluidic bulk

without any heat exchange with the solid wall in order to restore the saturation conditions.

$$\begin{cases} P_v > P_{sat} & for\ condensation \\ P_v < P_{sat} & for\ evaporation \end{cases} \tag{6.27}$$

Such kind of condensation likely occurs in the evaporator region where vapor pressure may exceed the saturation point and the wall temperature may be higher than the vapor one, which is a plausible situation in the evaporator region. Similar considerations can be made for evaporation on the menisci.
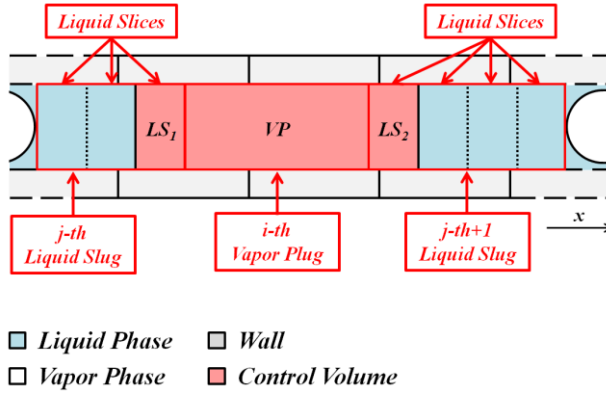
Figure 6.7: Schematic of the fluidic control volumes CV (in red) adopted in case of homogeneous phase changes through the interface.

The procedure adopted in this case is very similar to the one adopted to solve heterogeneous phase changes. The control volume CV (shown in Figure 6.7) is considered closed, adiabatic and isochoric. The two liquid slices (LS) and the vapor plug (VP) are open and adiabatic. However, if the control volume is adiabatic, it cannot be assumed that the phase changes are both isothermal and isobaric, thus only the assumption of $dP = 0$ has been maintained

(assumption 7). As before, in order to assure that $dV_{CV} = 0$, the homogeneous phase changes on the interface must be followed by isothermal expansions or compressions of the vapor sub-domain.

Evaporation. The mass and the energy balances written on the global control volume CV are:

$$
\begin{aligned}
dm_{CV} &= 0 \\
dU_{CV} &= 0 \\
dV_{CV} &= 0
\end{aligned}
\tag{6.28}
$$

Evaporation will take place in the liquid phase, thus the two LSs are considered two-phase. The mass and energy balances written for these two sub-domains therefore are:

$$
\begin{aligned}
dm_{LS\xi} &= -\dot{m}_{out,v,\xi}dt & \xi = 1 \div 2 \\
dU_{LS\xi} &= -PdV_{LS\xi} - h_v\dot{m}_{out,v,\xi}dt & \xi = 1 \div 2
\end{aligned}
\tag{6.29}
$$

Thus for each ξ-th LS:

$$
\begin{cases}
dm_{LS\xi} = d(m_l + m_v) = -\dot{m}_{out,v,\xi}dt \rightarrow dm_v = -dm_l - \dot{m}_{out,v,\xi}dt \\
dU_{LS\xi} = dU_l + dU_v = -PdV_l - PdV_v - h_v\dot{m}_{out,v,\xi}dt
\end{cases}
\tag{6.30}
$$

Following the same procedure shown for heterogeneous evaporation (see Equation (6.9) imposing $Q = 0$), and assuming incompressible liquid and isobaric phase change, Equation (6.30) yield to:

$$
m_l du_l + m_v du_v = -h_l dm_l - h_v dm_v + \frac{PV_v}{\rho_v}d\rho_v - h_v\dot{m}_{out,v,\xi}dt
$$

$$
m_l du_l + m_v du_v = -h_l dm_l + h_v(dm_l + \dot{m}_{out,v,\xi}dt) + \frac{PV_v}{\rho_v}d\rho_v - h_v\dot{m}_{out,v,\xi}dt
$$

$$
m_l du_l + m_v du_v = -h_l dm_l + h_v dm_l + \frac{PV_v}{\rho_v}d\rho_v
\tag{6.31}
$$

$$
m_l du_l + m_v du_v = h_{LV}dm_l + \frac{PV_v}{\rho_v}d\rho_v
$$

$$m_l du_l + m_v du_v = h_{LV} dm_l + R^* T_v V_v d \left(\frac{P_v}{R^* T_v} \right)$$

$$m_l du_l + m_v du_v = h_{LV} dm_l + T_v P_v V_v d \left(\frac{1}{T_v} \right)$$

$$m_l du_l + m_v du_v = h_{LV} dm_l + R^* m_v T_v^2 \, d \left(\frac{1}{T_v} \right)$$

$$m_l du_l + m_v du_v = h_{LV} dm_l + R^* m_v T_v^2 \left(\frac{0 - dT_v}{T_v^2} \right)$$

$$m_l du_l + m_v du_v = h_{LV} dm_l - R^* m_v dT_v$$

$$\int_{u_i}^{u_i+1} (m_l du_l + m_v du_v) + \int_{T_i}^{T_i+1} m_v R^* dT_v = \int_{m_i}^{m_{i+1}} h_{LV} dm_l$$

$$m_{l,t_i} \Delta u_l |_{t_i}^{t_i+1} = h_{LV} \Delta m_l |_{t_i}^{t_i+1}$$

Since $h_{LV} \Delta m_l |_{t_i}^{t_i+1} < 0$, the liquid which undergoes evaporation cools down. $\int_{u_i}^{u_i+1} m_v du_v = m_{v,t_i} \Delta u_v |_{t_i}^{t_i+1} = 0$ since LS_ξ does not contain any vapor at t_i ($m_{v,t_i} = 0$) and $\int_{T_i}^{T_i+1} R^* m_v dT_v = R^* m_{v,t_i} \Delta T_v |_{t_i}^{t_i+1} = 0$ for the same reason.

If the quality of each ξ-th LS liquid slices at the end of the process is zero, $\Delta m_l |_{t_i}^{t_i+1}$ represent the evaporated mass $m_{LV\xi}$, which is still unknown: $m_{l,t_i} \Delta u_l |_{t_i}^{t_i+1} = -h_{LV} |m_{LV\xi}|$.

The evaporated mass, then, flows inside VP. This allows $dm_{CV} = 0$ in Equation (6.28) since $\Delta m_{VP} |_{t_i}^{t_i+1} = \sum_{\xi=1}^{2} |m_{LV\xi}|$. In order to conserve the internal energy on VP, and thus on CV, one should account for:

$$dU_{VP} = d(H_{VP} - PV_v) = -PdV_v + \sum_{\xi=1}^{2} h_{v\xi} dm_{in\xi} \tag{6.32}$$

Assuming, as usual, the process isobaric and integrating between the initial and final status:

$$\int_{H_{t_i}}^{H_{t_{i+1}}} dH_{VP} = \sum_{\xi=1}^{2} h_{v\xi}|m_{LV\xi}| \rightarrow \Delta(m_v h_v)|_{t_i}^{t_i+1} = \sum_{\xi=1}^{2} h_{v\xi}|m_{LV\xi}| \tag{6.33}$$

In addition, in order to make Equation (6.28) true, the vapor element will undergo an isothermal compression ($PV_v = cost$):

$$P_{VP,t_{i+1}} V_{VP,t_{i+1}} = m_{VP,t_{i+1}} R^* T_{VP,t_{i+1}} \tag{6.34}$$

Differently from heterogeneous phase changes, this time the unknown is m_{LV} since $P_{VP,t_{i+1}} = P_{sat}$; $V_{VP,t_{i+1}}$ is chosen, on the other hand, to satisfy $dV_{CV} = 0$ (Figure 6.8):

$$V_{VP,t_{i+1}} = V_{VP,t_i} + \frac{\sum_{\xi=1}^{2}|m_{LV\xi}|}{\rho_l} \tag{6.35}$$

After this procedure for all the fluidic elements thermodynamic properties are updated to withstand the new thermodynamic status of the liquid and vapor elements at $t' = t + \Delta t$.
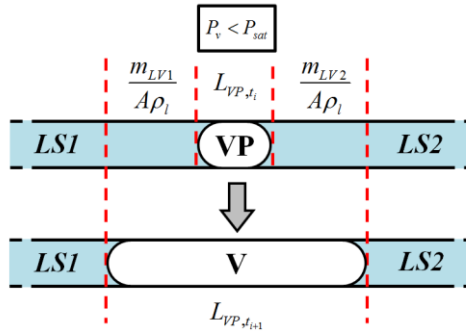
Figure 6.8: Schematic of length conservation during homogenous evaporation through the interface.

One should note that this procedure respects the 2nd principle of thermodynamics on the closed, isochoric and adiabatic global volume CV. Indeed:

$$TdS_{CV} = dU_{CV} + pdV_{CV} - \mu dN \geq 0$$
$$TdS_{CV} = dU_{CV}$$
$$TdS_{CV} = dU_{VP} + \sum_{\xi=1}^{2} dU_{LS\xi}$$
$$TdS_{CV} = \left[-PdV_v + \sum_{\xi=1}^{2} h_{v\xi} dm_{in,\xi} \right] + \left[\sum_{\xi=1}^{2} (m_{l,\xi} du_{l,\xi}) + \sum_{\xi=1}^{2} (u_{l,\xi} dm_{l,\xi}) \right]$$
$$TdS_{CV} = -PdV_v + \sum_{\xi=1}^{2} h_{v\xi} dm_{in,\xi} + \sum_{\xi=1}^{2} (h_{LV,\xi} dm_{l,\xi}) + \sum_{\xi=1}^{2} (u_{l,\xi} dm_{l,\xi})$$
$$\tag{6.36}$$
$$TdS_{CV} = -PdV_v - \sum_{\xi=1}^{2} (h_{l,\xi} dm_{l,\xi}) + \sum_{\xi=1}^{2} (u_{l,\xi} dm_{l,\xi})$$

$$TdS_{CV} = -PdV_v - \sum_{\xi=1}^{2} \left(\frac{P}{\rho_l} dm_{l,\xi} \right)$$
$$TdS_{CV} = -PdV_v - \sum_{\xi=1}^{2} (PdV_{l,\xi})$$
$$TdS_{CV} = 0$$

Condensation. The mass and the energy balances written on the global control volume VC are:

$$\begin{cases} dm_{CV} = 0 \\ dU_{CV} = 0 \\ dV_{CV} = 0 \end{cases} \tag{6.37}$$

Condensation will take place in the vapor phase, thus VP is considered two-phase. The mass and energy balance written for this sub-domain are:

$$\begin{cases} dm_{VP} = -\dot{m}_{out,l}dt \\ dU_{VP} = -PdV_{VP} - h_l\dot{m}_{out,l}dt \end{cases} \tag{6.38}$$

where $m_{out,l}$ is the condensed mass outgoing VP. Thus:

$$\begin{cases} dm_{VP} = d(m_l + m_v) = -\dot{m}_{out,l}dt \rightarrow dm_l = -dm_v - \dot{m}_{out,l}dt \\ dU_{VP} = dU_l + dU_v = -PdV_l - PdV_v - h_l\dot{m}_{out,l}dt \end{cases} \tag{6.39}$$

Following the same procedure previously shown (see Equation (6.9) imposing $Q = 0$), an assuming incompressible liquid and isobaric condensation, Equation (6.39) yield to:

$$m_l du_l + m_v du_v = -h_l dm_l - h_v dm_v + \frac{PV_v}{\rho_v}d\rho_v - h_l\dot{m}_{out,l}dt$$

$$m_l du_l + m_v du_v = h_l(dm_v + \dot{m}_{out,l}dt) - h_v dm_v + \frac{PV_v}{\rho_v}d\rho_v - h_l\dot{m}_{out,l}dt$$

$$m_l du_l + m_v du_v = h_l dm_v - h_v dm_v + \frac{PV_v}{\rho_v}d\rho_v \tag{6.40}$$

$$m_l du_l + m_v du_v + m_v R^* dT_v = -h_{LV} dm_v$$

$$\int_{u_i}^{u_i+1} (m_l du_l + m_v du_v) + \int_{T_i}^{T_i+1} m_v R^* dT_v = -\int_{t_i}^{mt_{i+1}} h_{LV} dm_v$$

$$m_{v,t_i}\Delta u_v|_{t_i}^{t_i+1} + R^* m_{v,t_i}\Delta T_v|_{t_i}^{t_i+1} = -h_{LV}\Delta m_v|_{t_i}^{t_i+1}$$

Since $-h_{LV}\Delta m_v|_{t_i}^{t_i+1} > 0$, the vapor that is condensing undergoes a heating process. $\int_{u_i}^{u_i+1} m_l du_l = m_{l,t_i}\Delta u_l|_{t_i}^{t_i+1} = 0$ since VP does not contain any liquid at t_i.

If the quality of the vapor plug at the end of the process is one, $\Delta m_v|_{t_i}^{t_i+1}$ represent the mass of the condensed vapor m_{LV}, which is still unknown: $m_{v,t_i}\Delta u_l|_{t_i}^{t_i+1} + R^* m_{v,t_i}\Delta T_v|_{t_i}^{t_i+1} = h_{LV}|m_{LV}|$.

The condensed mass, then, flows inside the two LSs. This allows $dm_{CV} = 0$ since $\sum_{\xi=1}^{2}\Delta m_{LS\xi}|_{t_i}^{t_i+1} = \sum_{\xi=1}^{2}|m_{LV\xi}| = |m_{LV}|$. In order to

conserve the internal energy on each *LS*, and thus on *CV*, one should account for:

$$dU_{LS\xi} = d(H_{LS\xi} - PV_{l\xi}) = -PdV_{l\xi} + h_{l\xi}dm_{in\xi} \qquad \xi = 1 \div 2 \qquad (6.41)$$

Assuming, as usual, the process isobaric and integrating between the initial and final status, for each LS:

$$\int_{H_{t_i}}^{H_{t_{i+1}}} dH_{LS\xi} = h_{l\xi}|m_{LV\xi}| \rightarrow \Delta(m_l h_l)|_{t_i}^{t_i+1} = h_{l\xi}|m_{LV\xi}| \qquad (6.42)$$

In addition, in order to make Equation (6.37) true, the vapor element will undergo an isothermal expansion ($PV_v = cost$):

$$P_{VP,t_{i+1}}V_{VP,t_{i+1}} = m_{VP,t_{i+1}}R^*T_{VP,t_{i+1}} \qquad (6.43)$$

Differently from heterogeneous phase changes, this time the unknown is m_{LV} since $P_{VP,t_{i+1}} = P_{sat}$; $V_{VP,t_{i+1}}$ is chosen, on the other hand, to satisfy $dV_{CV} = 0$ (Figure 6.9):

$$V_{VP,t_{i+1}} = V_{VP,t_i} - \frac{|m_{LV}|}{\rho_l} \qquad (6.44)$$
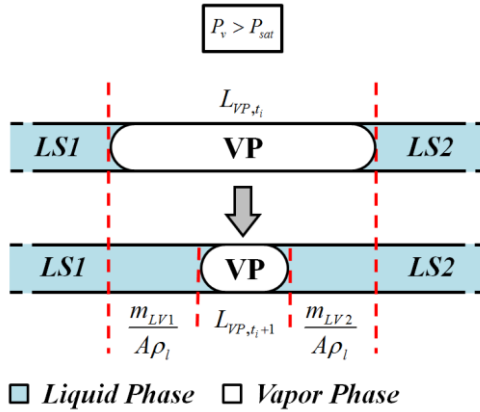
Figure 6.9: Schematic of length conservation during homogenous evaporation through the interface.

After this procedure for all the fluidic elements thermodynamic properties are updated to withstand the new thermodynamic status of the liquid and vapor elements at $t' = t + \Delta t$.

One should note that this procedure respects the 2nd principle on the closed, isochoric and adiabatic global volume CV. Indeed:

$$TdS_{CV} = dU_{CV} + pdV_{CV} - \mu dN \geq 0$$

$$TdS_{CV} = dU_{VP} + \sum_{\xi=1}^{2} dU_{LS\xi}$$

$$TdS_{CV} = [m_v du_v + u_v dm_v] + \left[-\sum_{\xi=1}^{2}(PdV_{l\xi}) + \sum_{\xi=1}^{2}(h_{l\xi} dm_{in\xi}) \right]$$

$$TdS_{CV} = -m_v R^* dT_v - h_{LV} dm_v + u_v dm_v - \sum_{\xi=1}^{2}(PdV_{l\xi}) + \sum_{\xi=1}^{2}(h_{l\xi} dm_{in\xi})$$

$$TdS_{CV} = \frac{PV_v}{\rho_v} d\rho_v - (h_v dm_v - h_l dm_v) + u_v dm_v - \sum_{\xi=1}^{2}(PdV_{l\xi}) + \sum_{\xi=1}^{2}(h_{l\xi} dm_{in\xi}) \quad (6.45)$$

$$TdS_{CV} = \frac{PV_v}{\rho_v} d\rho_v - \frac{P}{\rho_v} dm_v - \sum_{\xi=1}^{2}(PdV_{l\xi})$$

$$TdS_{CV} = -\frac{P\rho_v}{\rho_v} dV_v - \sum_{\xi=1}^{2}(PdV_{l\xi})$$

$$TdS_{CV} = -PdV_v - \sum_{\xi=1}^{2}(PdV_{l\xi})$$

$$TdS_{CV} = 0$$

Fluidic Mass and Energy Balance after Phase Changes

In order to complete mass and energy balances for each time step, after having taken into account heterogeneous phase changes and homogeneous evaporation/condensation through the interface, all the other physical phenomena (e.g. sensible heat exchange with the

wall, axial conduction, etc.) should be considered. To be noticed that the three steps of the procedure are occurring in sequence during the same time step Δt. The control volumes adopted this time consist of single vapor plugs or single liquid slices (see Figure 6.10). These represent closed domains. A Lagrangian approach has been adopted.
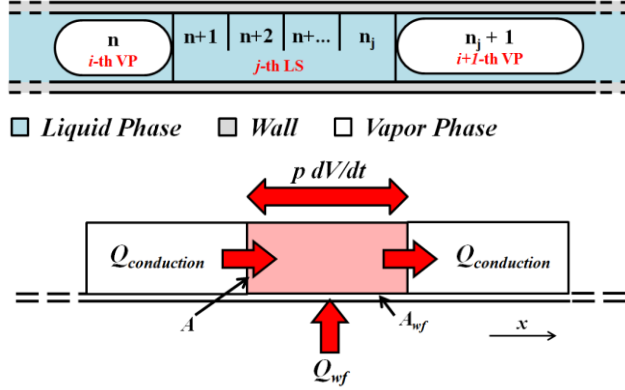
Figure 6.10: Schematic of the liquid/vapor energy balance for the n-th domain.

Mass Balance. Since phase changes do not occur anymore, for both liquid and vapor elements the mass balance is automatically verified.

$$dm_{f,n} = 0 \tag{6.46}$$

Energy Balance. Both liquid slices and vapor plugs are closed volumes. Thus the energy balance can be explicated as in the following and allows the calculation of the final temperature for each fluidic element in the inner channel. The energy equation is integrated making use of the 1st Adams–Bashforth integration scheme if new elements have been previously generated or old ones have disappeared in the time step, the 2nd Adams–Bashforth integration scheme otherwise.

All the fluidic elements are moving, but in a Lagrangian system, total time derivatives match ordinary time derivatives; thus the energy equation for the n-th domain is:

$$c_{V,f} m_{f,n} \frac{dT_{f,n}}{dt} = \left(q_{wf,f} A_{wf}\right)\big|_n + \left(k_f A \frac{\partial T_f}{\partial x}\Big|_n^{n-1} - k_f A \frac{\partial T_f}{\partial x}\Big|_{n+1}^{n}\right) - P_{f,n} \frac{dV_{f,n}}{dt} \quad (6.47)$$

where the subscript f stands for fluidic, alternatively vapor or liquid and A is the cross sectional area (Figure 6.10).

As shown in Figure 6.10, the first term on the right side of Equation (6.47) accounts for the sensible heat transferred between the wall and the fluid when no phase changes have occur previously; the second term is the axial conduction within the fluid; the last term is the compression work computed only for vapor plugs.

Momentum Equation. The momentum equation has been solved directly for the global time step Δt without accounting separately for phase changes; thus $dm \neq 0$ if evaporation or condensation has occurred; however it is a known quantity for all the liquid slugs.

Since the friction between vapor plugs and wall elements is neglected (Assumption 3), it is assumed that vapor plugs are dragged along the tube by the liquid motion. Thus, the momentum equation is calculated for the liquid elements only: Störmer-Verlet algorithm [100] [101] has been applied to compute the velocity and the position at each time step adopting a Lagrangian approach.

The momentum equation integrated along the j-th liquid slug length is:

$$\frac{d(mw)|_{l,j}}{dt} = [mg cos(\vartheta)]|_{l,j} + A\left(P_{v,i} - P_{v,i+1}\right) - \left(0.5 f_\tau \frac{m}{d_{in}} w|w|\right)\Big|_{l,j} \quad (6.48)$$

where w is the liquid slug velocity and d_{in} the tube internal diameter.

The first term on the right side is the gravity force: g is the gravity acceleration and ϑ is the local angle between the gravity vector and

the flow direction. The second and the third terms are the forces respectively due to adjacent vapor expansion/compression (for the subscripts refer to Figure 6.1) and friction (viscous shear and minor losses due to bends and turns). Pressure drop due to capillary forces has been neglected because of the constant cross section along the tube length and because liquid menisci maintain spherical shape with zero contact angle at the wall (Assumption 4).

Viscous shear is treated semi-empirically. The friction coefficient f_τ is evaluated either for fully developed laminar (Hagen-Poiseuille, [102]) o turbulent flow (Haaland equation, [103]):

$$f_\tau = \frac{64}{Re} \qquad\qquad\qquad\qquad Re < 2000$$

$$\frac{1}{\sqrt{f_\tau}} = -1.8log_{10}\left[\left(\frac{\varepsilon}{3.7d_{in}}\right)^{1.11} + \frac{6.9}{Re}\right] \qquad Re \geq 2000$$

$$(6.49)$$

where ε is the tube internal surface roughness and Re the local Reynolds number.

As suggested by Mameli et al. [74], minor losses are computed only if the liquid slug passes through at least a turn or a bend. The corresponding friction coefficient is evaluated according to Darby 3K method [104] which empirical parameters (K_{Re}, K_d and K_r) are listed in Table 6.1:
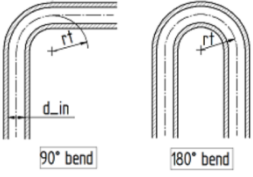
$$f_\tau = \frac{K_{Re}}{Re} + K_r\left[1 + K_d\left(\frac{0.0254}{d_{in}}\right)^{0.3}\right] \tag{6.50}$$

The velocity of each liquid slug is calculated by solving the momentum equation (Equation (6.48)), while their new position $x_{t_{i+1}}$ can be estimated as:

$$dx|_{l,j} = \left(wdt + \frac{a}{2}dt^2\right)\Big|_{l,j} \tag{6.51}$$

where a is acceleration defined as the ratio between the applied forces and the slug mass.

Fitting type	r_t/d_{in}	K_{Re}	K_r	K_d
Bend 90°	1.25	800	0.091	4
Turn 180°	1.25	1000	0.1	4

Table 6.1: Friction coefficients for bends and turns according to Darby 3K method.

6.1.3   Solid/Fluid coupling

Solid and fluidic domains are related by means of the heat exchanged between the wall and the fluid, q_{wf}, which appears in the energy balances (Equation (6.1) and (6.47), and in section 6.1.2). The wall domains are fixed in time (Eulerian approach), while the fluidic elements are moving (Lagrangian approach). Thus, a fluidic element may face different wall domains at each time step; in addition a wall element may face more than one fluidic element and vice versa (Figure 6.11). Accounting for Assumption 6, q_{wf} is defined as:

$$\begin{cases} q_{wf,w} = \frac{1}{A_{wf}} \sum_{n=1}^{N_f} htc(T_w - T_n)A_{wf,n} \\ q_{wf,f} = \frac{1}{A_{wf}} \sum_{k=1}^{N_w} htc(T_{w,k} - T_f)A_{wf,k} \end{cases} \tag{6.52}$$

where h is an appropriate heat transfer coefficient, A_{wf} is the total area between the wall and the fluidic domains, while $A_{wf,n}$ and $A_{wf,k}$ represent the area in common between the k-th wall element and the n-th fluidic element.

The heat transfer coefficient h should account for sensible or latent heat, depending if heterogeneous phase changes are occurring or not in the time step.
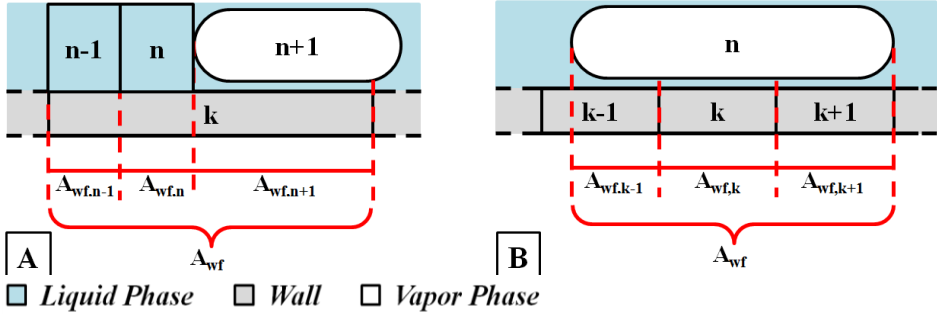
Figure 6.11: Definition of A_{wf}, $A_{wf,n}$ and $A_{wf,k}$ from the wall point of view (A) and from the fluid point of view (B).

Sensible heat transfer coefficient. If no heterogeneous phase changes occur, only sensible heat is transferred between solid and fluidic domains ($q_{wf,f}A_{wf} = 0$ in section 6.1.2).

In the case of liquid slugs, classical semi-empirical formula have been adopted even if they have not been developed for oscillating flow in mini-channels: Shah and London [105] correlation is implemented for the laminar flow thermally developing region (Equation (6.53)), the Gnielinski correlation [102] is used for the transient/turbulent flow (Equation (6.54)) while Dittus-Boelter correlation [102] is applied for the fully developed turbulent flow (Equation (6.55)).

$$htc = \begin{cases} 1.953 \frac{k}{d_{in}} \left(RePr \frac{d_{in}}{L_x} \right)^{\frac{1}{3}} & \left(RePr \frac{d_{in}}{L_x} \right) \geq 33.3 \\ \frac{k}{d_{in}} \left(4.364 + 0.0722 RePr \frac{d_{in}}{L_x} \right) & \left(RePr \frac{d_{in}}{L_x} \right) < 33.3 \end{cases} \qquad Re \leq 2000 \qquad (6.53)$$

$$htc = \frac{k}{d_{in}} \left[\frac{\left(\frac{f_T}{8} \right)(Re - 1000)Pr}{1 + 12.7 \left(\frac{f_T}{8} \right)^{\frac{1}{2}} \left(Pr^{\frac{2}{3}} - 1 \right)} \right] \qquad 2000 < Re < 10000 \qquad (6.54)$$

$$htc = 0.023 \frac{k}{d_{in}} Re^{0.8} Pr^n \qquad \begin{array}{l} T_w > T \rightarrow n = 0.4 \\ T_w \leq T \rightarrow n = 0.3 \end{array} \qquad Re \geq 10000 \qquad (6.55)$$

where Pr is the Prandtl number and L_x is the thermal entry length which has been set equal to the evaporator/adiabatic/condenser extent depending on the location of the j-th liquid slug.

On the other hand, the sensible heat exchanged between wall and vapor domains cannot be estimated by mean of the above reported classical correlations. The reason of that lies in the presence of the liquid film. Since the proposed model is mono-dimensional, it considers the liquid film constant in space and time (Assumption 8). Actually, some authors [71] [72] report that the film dynamic may deeply influence the heat transferred by vapor plugs. Thus a fitting correlation has been adopted to fix the lack of modelling improving the calculation of the vapor sensible heat. Assuming that both forced and natural convection are involved in the heat transfer process and making use of the Buckingham theorem, the vapor-wall heat transfer coefficient has been described as function of both Reynolds and Rayleigh (Ra) numbers. The four fitting coefficients are estimated by comparison with experimental results in different operative conditions and under various gravity levels[14]; a is defined at 293K for a hypothetic film thickness δ of 50μm[15].

---

[14] Equation (6.56) has been validated against experimental data from FC-72, 0.5% volumetric filling ratio. Further comparisons are needed to extend the use of the above correlation for other fluids and filling ratios.

[15] The last available measurements by Han et al [107] performed on micro-tubes filled with different fluids in adiabatic conditions show that a valid range for the film thickness is between 1μm and 100μm. However, δ should be at least equal or higher than the roughness of the inner surface of the tube, which, for the tested cases, has been assumed of 50μm.

$$htc = htc_0 + aRe^b Ra^c \qquad \begin{array}{ll} htc_0 = 200\,\frac{W}{m^2K} & b = 0.25 \\ a = 70\,\frac{W}{m^2K} & c = 0.4 \end{array} \tag{6.56}$$

Phase change heat transfer coefficients. If phase change phenomena occur, then latent heat must be comprised and proper boiling/condensing heat transfer coefficients must be defined $(q_{wf,f}A_{wf} = 0$ in Equation (6.47)). Since experimental correlations are missing, constant heat transfer coefficients have been assumed:

$$htc = \begin{cases} 10000\,\frac{W}{m^2K} & condensation \\ 20000\,\frac{W}{m^2K} & evaporation \end{cases} \tag{6.57}$$

A sensitivity analysis (section 6.3) has been performed to understand the influence of the chosen values on the model results: the maximum steady state temperature deviation was less than 0.5K for boiling/condensing heat transfer coefficient ranging from $4000/2000 W/m^2K$, [4], to $30000/15000\ W/m^2K$. This happens because most part of the heat is transferred by sensible ways only, as underlined by Shafii et al. [45]. The latent heat is prevalently the mechanical motor of the system, inducing phase change phenomena and strong oscillations/circulation of the fluid within the channel.

6.2 Numerical implementation

The ordinary differential equations (ODE) system describing the physical model has been implemented and solved making use of the open source software GNU Octave.

The computational time step is generally constant but if new elements are generated or old elements disappear, it is reduced of a magnitude in order to damp any possible unstable numerical

oscillations; then it is gradually restored following a slope increment after 10 iterations.

A sensitivity analysis (section 6.3) underlined that once the time step is small enough to guarantee numerical stability, the results are independent on the chosen value. Thus, for each simulation, Δt is taken as the maximum allowable in order to minimize the total simulation time.

6.3   Sensitivity analysis on assumed inputs

The proposed numerical model requires inputs in order to account for the geometrical, physical and thermal properties of the device which is going to be simulated.

Few of the required information, however, do not have a simple definition (i.e. boiling/condensing heat transfer coefficients, liquid film thickness, $\Delta T_{super-heating/cooling}$, htc_∞). The boiling/condensing heat transfer coefficients, for example, cannot be derived from empirical correlations and few studies (e.g. [4]) report qualitative measurements for oscillating two-phase flow in capillary channels. The same thing happens for the liquid film thickness as well as for the temperature difference linked to boiling or condensing retardation. The environmental heat transfer coefficient in forced convection, on the other hand, might be derived from experimental correlations, but it strictly depends on the condenser assessment; in addition the velocity of the cooling medium has to be guessed since it is usually not measured or reported in most part of the experimental works. Thus, the correct estimation of this parameter is very complicated.

Moreover, other inputs required by the model are merely numerical parameters used for spatial and temporal discretization (e.g. initial number of liquid slugs, initial position of the liquid slugs, discretization at $t = 0$ of each liquid domain, Δt).

For all these unknown data, a sensitivity analysis has been performed in feasible ranges in order to verify the influence of the chosen values on the model predictions. The geometrical characteristics of the bottom heated mode PHP tested during the experimental campaigns (section 3 and 4) have been used to define the known inputs for all the performed simulations (Table 6.2); 50W have been provided at the evaporator zone for all the cases.
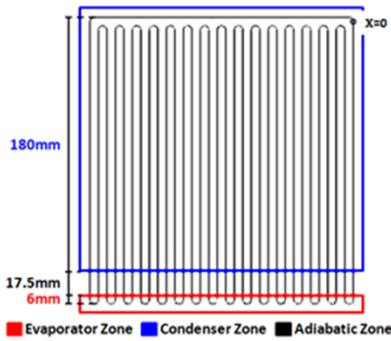
Input parameter	Value
Working fluid	FC-72
Volumetric filling ratio	0.5
Tube material	Copper
Inner/Outer diameter	1.1/2.0mm
Surface roughness	50μm
Total length	6.62m
N° of evaporator bends	16
Gravity	1g
External temperature	21 °C

Table 6.2: Principal features of the tested bottom heated mode PHP. Geometrical and physical inputs.

6.3.1   Physical parameters

This section presents the sensitivity analysis performed on the five unknown physical parameters: boiling/condensing heat transfer coefficients, liquid film thickness, $\Delta T_{super-heating}$, $\Delta T_{cooling}$, htc_{∞}.

Results are presented in the following, in term of local, temporal average, wall temperature recorded in each one of the three PHP macro-zones. The red line represents the evaporator section, the grey line the adiabatic zone, while the blue line describes the condenser.

Figure 6.12 excludes any influence of the imposed boiling/condensing heat transfer coefficient on the model results: the maximum steady state temperature deviation is less than 0.5K for inputs ranging from $4000/2000 W/m^2K$, [4], to $30000/15000 W/m^2K$. This happens because most part of the heat is transferred by sensible ways only [45]. The latent heat is prevalently the driving motor of the system, inducing phase change phenomena and, thus, fluid motion within the channel.
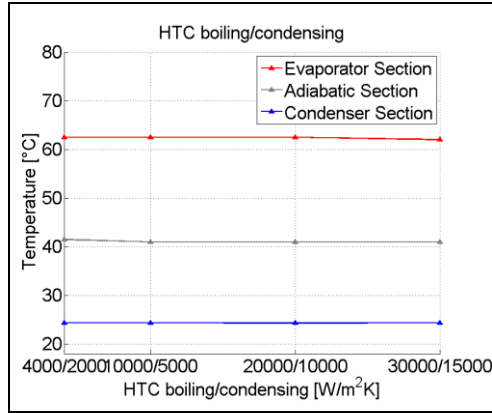
Figure 6.12: Local, temporal average, wall temperature at varying of the boiling/condensing heat transfer coefficients.

Since the model does not account for the liquid film thermo-dynamic[16], the influence of the liquid film thickness on the final results is negligible (deviation < 2.5K as shown in Figure 6.13). Tests have been performed ranging from 50μm to 100μm; film thicknesses smaller than 50μm are not feasible since this is the value of the internal tube surface roughness. The feasibility of this range has, also, been confirmed applying the empirical correlation proposed by Aussillous et al. [106], or its correction from Han et al. [107], for the

---

[16] Eq. (6.55) is computed for a conventional film thickness of 50μm.

estimation of the liquid film thickness: assuming an average fluid velocity[17] of 1m/s, the computed δ lies between 50 μm and 90μm.
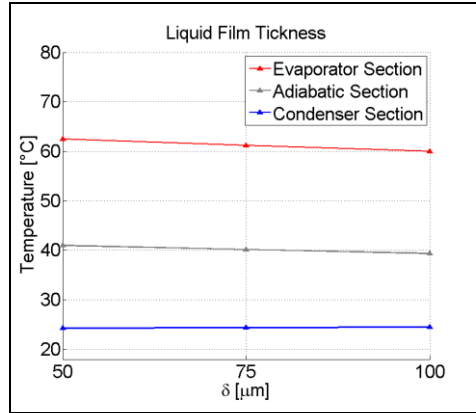
Figure 6.13: Local, temporal average, wall temperature at varying of the liquid film thickness.
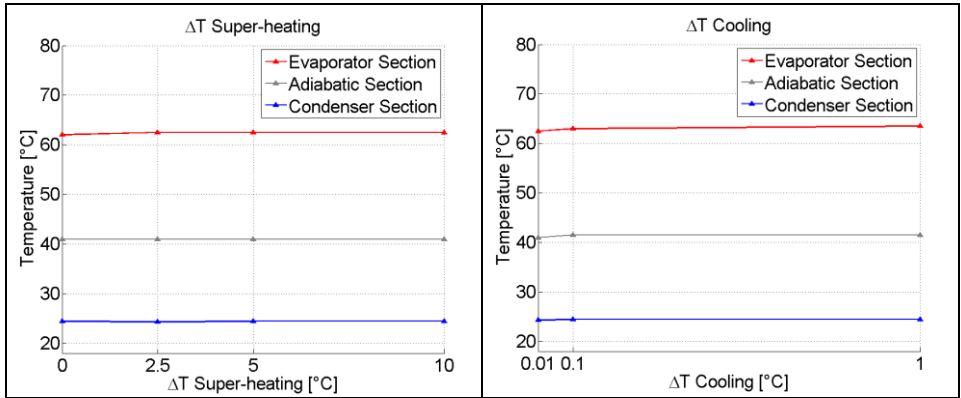
Figure 6.14: Local, temporal average, wall temperature at varying of the $\Delta T_{super-heating}$ (left) and $\Delta T_{cooling}$ (right).

---

[17] The average liquid velocity results, a posteriori, from the performed numerical simulations.

Figure 6.14 shows respectively, on the left, the influence of the $\Delta T_{super-heating}$ and, on the right, $\Delta T_{cooling}$ on the model results. Their influence is negligible since the temperature deviation is less than 1K.
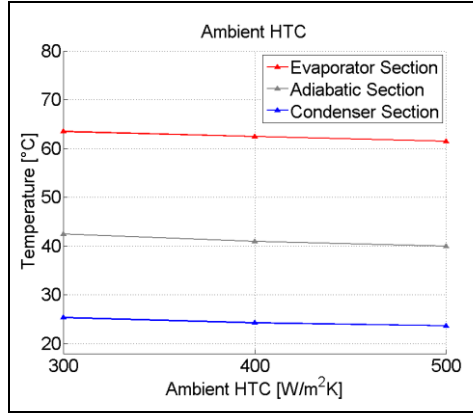
Figure 6.15: Local, temporal average, wall temperature at varying of the environmental heat transfer coefficient.

The last physical parameter tested was the environmental heat transfer coefficient; htc_∞ was the most delicate unknown input since it regulates the rate of heat exchanged between the condenser and the external cooling medium (i.e. air in forced convection). It has been estimated from experimental data at equilibrium. The real htc_∞, however, should be evaluated considering the presence of the experimental heat sink (of area A) which is a finned aluminum plate. However, since the heat sink has not been modeled, from a numerical point of view the htc_∞ should be to corrected accounting for a lower area $A^* < A$, the one on which the numerical boundary has been actually applied (serpentine to air area). Depending on the power, the calculated parameter lay between 300 W/m²K and 500W/m²K. With such conditions, the computed maximum temperature deviation was less than 2.5K (Figure 6.15). Thus the influence of the chosen value is

small enough to consider the model results independent on it for the tested range.

6.3.2   Numerical parameters

This section presents the sensitivity analysis performed on the three unknown numerical inputs: initial number and position of each liquid slug, discretization at $t = 0$ of each liquid domain, integration time. Again results are reported mainly in form of local, temporal average, wall temperature recorded in the evaporator, adiabatic and condenser zone.
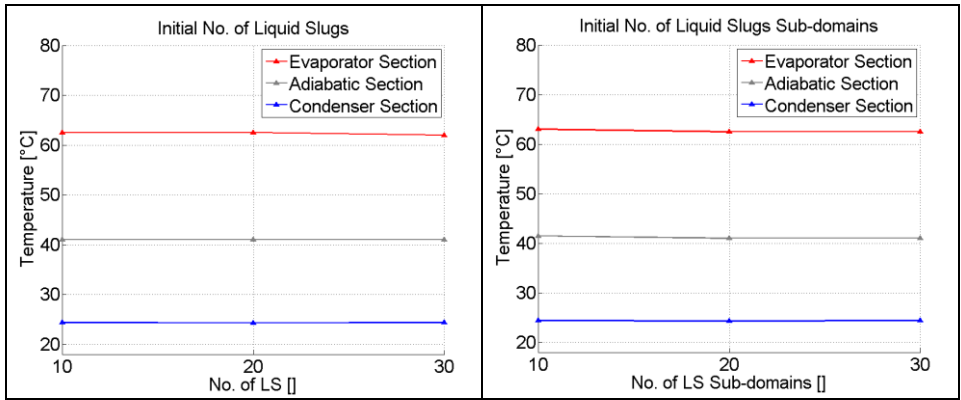
Figure 6.16: Local, temporal average, wall temperature at varying of the initial number of liquid slugs (left) and their initial discretization.

Figure 6.16 shows, respectively, on the left, the influence on the model results of the number of liquid domains and, on the right, their discretization at $t = 0$. In both cases, the temperature deviation is less than 0.5K and, thus, negligible. In addition, even the steady state number of liquid slugs for all the conditions sets around 10 independently on the chosen starting scenario. Note that changes in the initial number of liquid domains mean changes, at the same time, in the initial location of all the liquid slugs. Thus it can be concluded

that even the influence of the initial location of the liquid domains is unimportant for the results of the model.

Finally, the sensitivity analysis performed on the integration time underlined that once Δt is small enough to guarantee numerical stability ($\Delta t < 0.5s$), the results are independent on the chosen value (Figure 6.17).
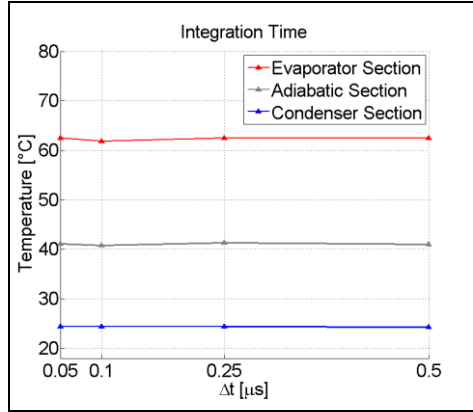
Figure 6.17: Local, temporal average, wall temperature for different integration times; 0.5ms is the maximum allowable Δt.

6.3.3   Chosen unknown inputs

All the analyses reported in the following chapters have been obtained assuming the inputs listed in Table 6.3.

Input	Value	Input	Value
$h_{boiling/condensing}$	Eq. (6.57)	N_{LS} at $t = 0$	20
h_∞	400W/m²K	No. of liquid sub-domains at $t = 0$	20
δ	50µm		
$\Delta T_{super-heating}$	2.5K	N_w	400
$\Delta T_{cooling}$	0.01K	Δt	≤ 0.5ms

Table 6.3: Unknown inputs parameters guessed in feasible ranges. Sensitivity analyses showed independency of the model results.

Chapter 7
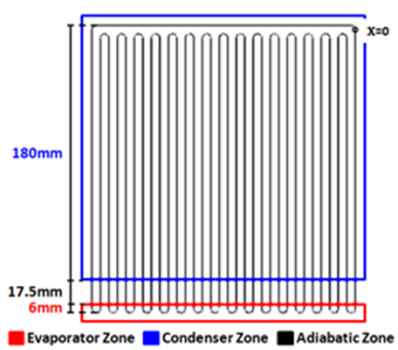
7. Numerical model validation

The model described in the previous chapter has been validated in several operative conditions and under various gravity levels by comparisons with experimental data achieved on ground, in hyper (chapter 3) and micro-gravity (chapter 4).

The results are presented mainly in terms of local spatial average wall temperature and pressure time evolutions since the experimental apparatus is equipped with a pressure transducer and

14 T-thermocouples. For transient operative conditions, power inputs and/or gravity levels are shown together with the pressure/temperature trends on the secondary y-axis or are reported directly over the plot line. Note that the experimental evaporator thermocouples are not exactly located in the hot section, but just 6mm above it, actually in the adiabatic zone, because of the presence of the electrical heating wire (chapter 3 and 4). In order to be coherent with the model described in chapter 6, the temperatures recorded by these thermocouples should be compared with the ones computed in the above mentioned adiabatic region. Therefore, experimental evaporator temperatures will be referred from now on as adiabatic temperatures.

The geometrical features and the physical properties of the tested device are listed in Table 7.1. These are the main inputs required to set up all the numerical simulations performed in the following sections.

Input parameter	Value
Working fluid	FC-72
Volumetric filling ratio	0.5 - 0.7*
Tube material	Copper
Inner/Outer diameter	1.1/2.0 mm
Surface roughness	50 μm
Total length	6.62 m
N° of evaporator bends	16
Gravity	0.01g - 2g

* only for the 59th Parabolic Flight campaign

Table 7.1: Principal features of the tested PHP. Geometrical and physical inputs.

7.1 Ground tests

Normal gravity tests have been performed on ground imposing a constant environmental temperature of 294K and increasing the heat input from 50W to 100W with an intermediate step at 70W. The starting heat input level is kept for 16 minutes while the following are kept for 8 minutes.

7.1.1 Bottom Heated Mode configuration

Figure 7.1 shows the comparison in term of local spatial average wall temperature between the experimental and the numerical results. The red line indicates the mean temperature in the evaporator zone, the gray line in the adiabatic region and the blue line in the condenser. The standard deviation at each time step of the experimental results is also reported as a colored range over the solid line.
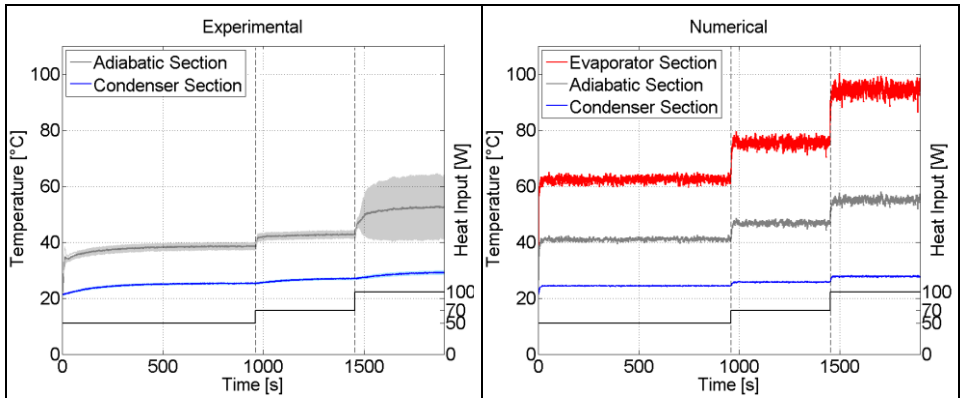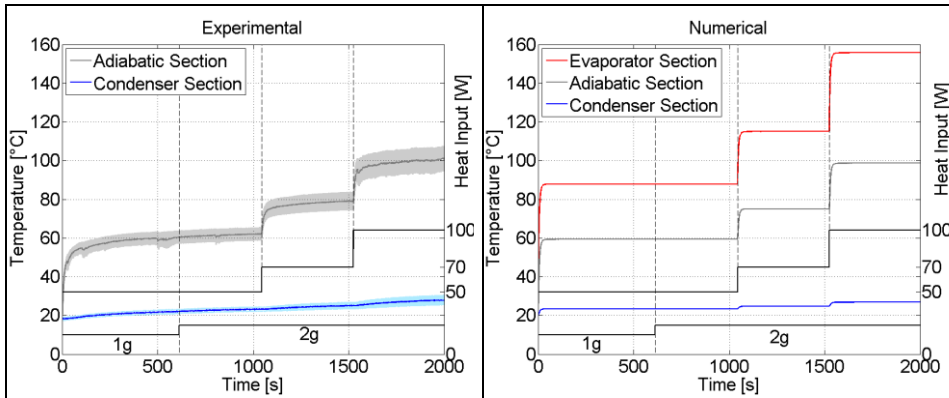

Figure 7.1: Comparison between experimental (left) and numerical (right) wall temperatures for a bottom heated mode PHP at different heat inputs in normal gravity. Solid lines represent the local spatial average wall temperature; colored ranges on the experimental results indicate the standard deviation on the recorded data.

It is clearly visible that the model is able to reproduce the experimental data for all the tested conditions. The maximum error in term of wall temperature is less than 6%; in addition the numerical temperatures fit within the experimental dispersion range, a part for the 70W results that are little over-estimated.

The model is also able to reproduce the transition of about 10s between the different operative conditions (power levels) clearly visible for the adiabatic temperatures; the dynamic of the condenser, on the other hand, seems to not be correctly reproduced. However this was expected since the experimental results are influenced by the presence of the heat sink, with high heat capacity, and, thus, high thermal inertia, while the model is not accounting for the heat sink presence and considers only the PHP serpentine. Thus the numerical dynamic at the condenser is, obviously, more rapid. For the same reason, an under-prediction of the start up time appears in the predicted results.
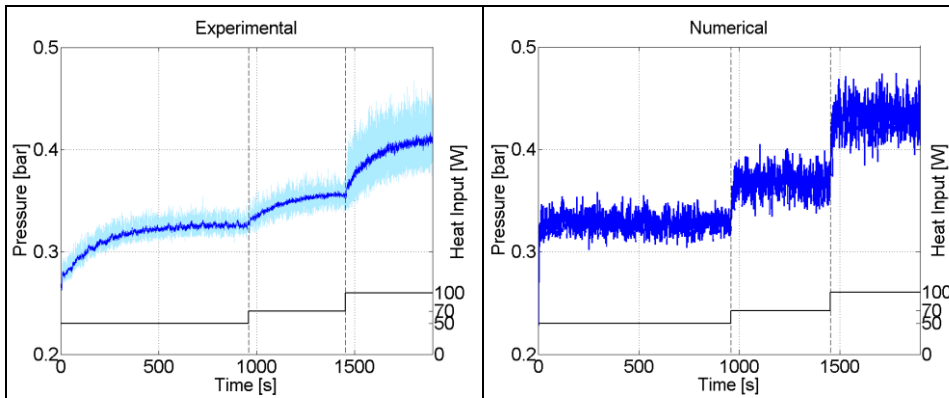
Figure 7.2: Comparison between experimental (left) and numerical (right) pressure for a bottom heated mode PHP at different heat inputs in normal gravity. Solid lines represent the filtered data, while colored ranges on the experimental results indicate the non filtered recorded pressure.

Figure 7.2 shows the comparison between experimental and numerical data in term of pressure. Again the model is able to reproduce the experimental results in steady state: the maximum error[18] on the computation is less than 1.5%; also the oscillations are reproduced. The transient time is, on the other hand, strongly underestimated. Since the fluid and the thermal dynamic are strictly connected, a so evident error appears not justifiable. Experimental issues may have influenced the results: first of all the position of the pressure sensor is not completely appropriate, since being the sensor plugged outside the condenser section, the pressure signals may be damped and/or delayed; secondly, the recorded pressure is influenced by the temperatures at the condenser, $p = f(\rho, T)$, which dynamics is influenced by the heat sink not directly modeled.

In addition, the Fast Fourier Transform (FFT) analysis performed on both the experimental and numerical pressure signals does not indicate any dominant frequency, underling that the model is not introducing spurious neither artificial dynamics (Figure 7.3).
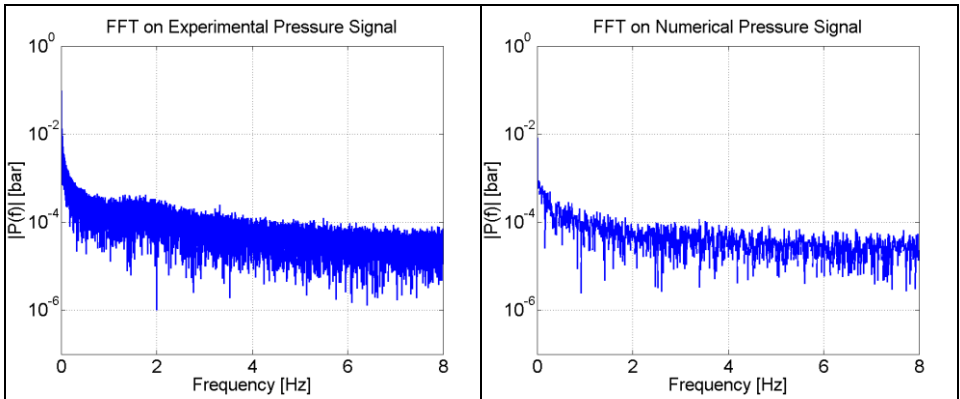
Figure 7.3: FFT analysis performed on experimental (left) and numerical (right) pressure signal.

---

[18] evaluated at steady state as $100 \dfrac{|\bar{p}_{exp} - \bar{p}_{num}|}{\bar{p}_{exp}}$.

Finally, a check has been performed in order to assure the conservation of mass (m), length (L), and energy.

Figure 7.4, on the left, shows the variation of the total fluidic mass contained within the PHP tube in time, while, on the right, it reports the temporal deviation of the fluid total length from a proper constant value. In both cases, the model guarantees the conservation of the two physical constraints being null the variation in time.

$$\Delta m(t) = \left| \left(\sum_{i=1}^{N_{VP}} m_i + \sum_{j=1}^{N_{LS}} m_j \Bigg|_t \right) - \left(\sum_{i=1}^{N_{VP}} m_i + \sum_{j=1}^{N_{LS}} m_j \Bigg|_{t=0} \right) \right| \qquad (7.1)$$

$$\Delta L(t) = \left| \left(\sum_{i=1}^{N_{VP}} L_i + \sum_{j=1}^{N_{LS}} L_j \Bigg|_t \right) - L_w \right| \qquad (7.2)$$

L_w is the PHP tube length; LS and VP stand for liquid slugs and vapor plugs; for the sub-scripts i and j refer to Figure 6.1.
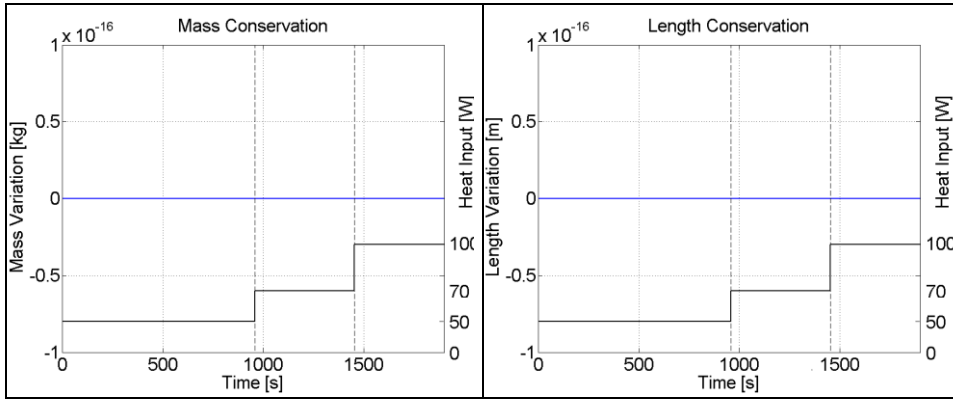
Figure 7.4: Temporal variation of the total fluidic mass, on the left, and the total fluidic length, on the right.

Figure 7.5 assures the energy conservation. The model, indeed, must guarantee that, after a transition time, the power provided at

the evaporator section is equal to the power rejected to the external environment in the condenser zone (Figure 7.5 on the left). At the same time it must conserve the fluidic internal energy, (U), in steady state when the ingoing and the outgoing energy are alike: Figure 7.5 on the right, actually, shows a negligible percentage variation of U in time ($|\Delta U| < 0.1\%$).
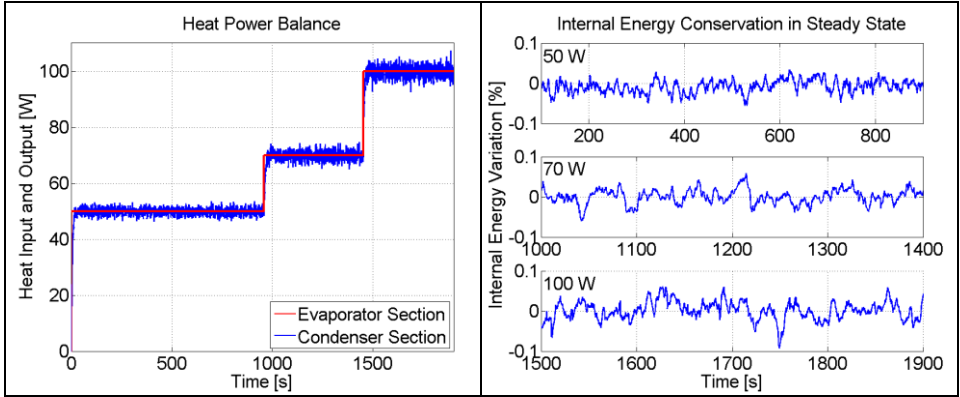
Figure 7.5: On the left, heat input at the evaporator section and output at the condenser; on the right, percentage variation in time of the fluidic internal energy.

7.1.2 Horizontal configuration

Figure 7.6 shows the comparison in term of pressure signals between the experimental and numerical results when the PHP is in horizontal configuration and the gravity force is not acting anymore along the fluid path direction. The reported figure shows that, unfortunately, the model is not able to reproduce the dynamic of the pressure data in steady state when the PHP is placed in horizontal position. Specifically, the numerical signal is not oscillating, a part for few sporadic events during the power transitions.
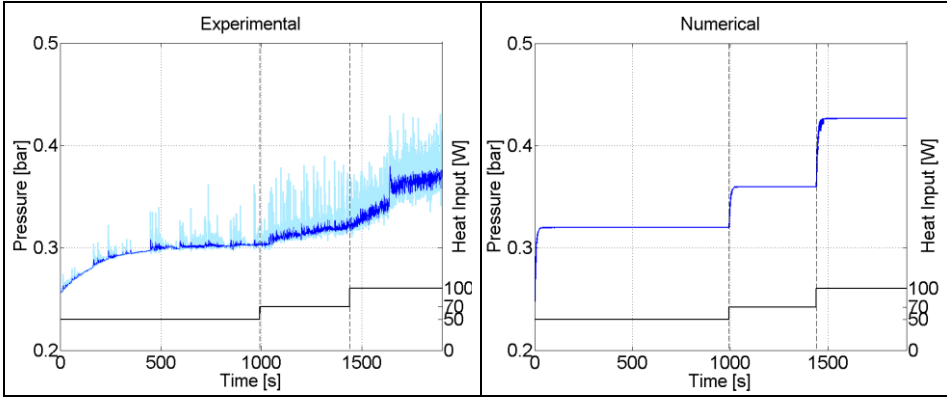
Figure 7.6: Comparison between experimental (left) and numerical (right) pressure for the horizontal PHP at different heat inputs in normal gravity. Solid lines represent the filtered data, colored ranges on the experimental results the non filtered recorded pressure.
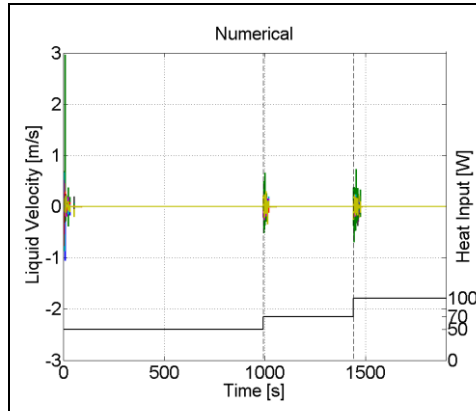
Figure 7.7: Numerical liquid slugs computed velocities; different colors indicate different fluidic elements. The instabilities originated by modifications in the operative conditions are quickly recovered inducing equilibrium state of the fluid.

The same behaviour is detectable in the computed velocities (Figure 7.7): the fluid within the horizontal device, indeed, starts

moving, but after some time it stops reaching an equilibrium condition. Although the experimental velocities have not been measured, as well as no visualization of the internal motion is available, it can be believed that if the fluid within the tube does not oscillate the recorded temperature should be much higher that the recorded data (Figure 7.8), since the heat would be transferred only by conduction mainly in the wall domain. Therefore, the model is not able to simulate the steady state dynamic of the fluid when the PHP is horizontal.
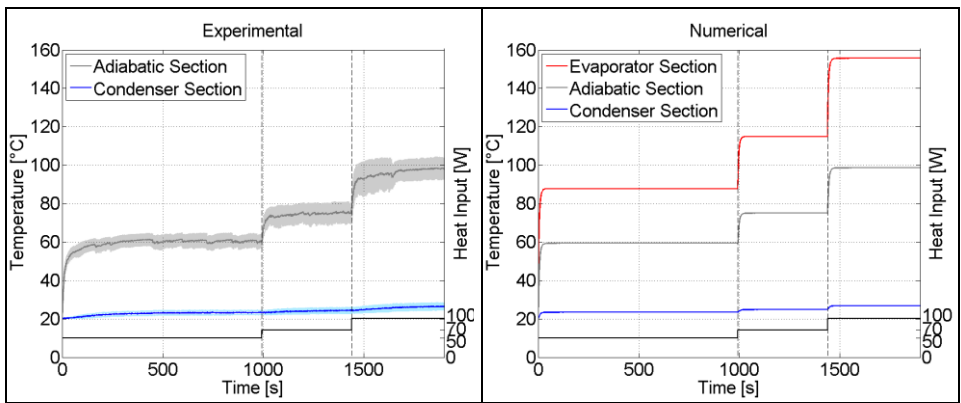
Figure 7.8: Comparison between experimental (left) and numerical (right) wall temperatures for the horizontal PHP at different heat inputs in normal gravity. Solid lines represent the local spatial average wall temperature, while colored ranges on the experimental results indicate the standard deviation on the recorded data.

The numerical damping is probably too high avoiding any instability at the base of the real fluid oscillations; the vertical configuration does not suffer this problem since the presence of gravity opposes such kind of numerical stabilization. The damping effects may derive both from the numerical method adopted for the computation of the liquid momentum (Verlet algorithm) chosen for

its ability to capture the long term system dynamics in an accurate and stable way and from the hierarchical numerical procedure used to implement evaporation and condensation processes. In particular the homogeneous phase changes computed after the heterogeneous ones soften the localized pressure picks experimentally observed for a horizontal PHP which are responsible of the fluid oscillations (gravity is, instead, the principal actor when the PHP is placed in vertical mode).

Nevertheless, since a tuning parameter has been introduce to overcome the theoretical lack of empirical formulas to compute the sensible heat transfer coefficient between vapor elements and wall domains (Equation (6.56)), the fitting operation has allowed to gain, also for the horizontal configuration, the correct temperature trends (Figure 7.8) even if the internal dynamic is wrongly computed. This means that the term h_0 has been over-estimated while the multiplier a has been, proportionally, under-estimated in order to allow the temperature prediction at all gravity levels whit respect to the real case.

7.2 Hyper-gravity tests

The numerical results in hyper-gravity conditions have been compared with the experimental data obtained on the ESA ESTEC LDC during the ESA Educational program SpinYourThesis!2013 [26] [27] (chapter 3).

Experiments have been conducted both on horizontal and vertical bottom heated mode configuration. However, even if data are available up to 20g, in the following 2g is the maximum simulated hyper-gravity level. The proposed numerical model is, indeed, applicable to a confined operating regime (i.e. slug flow). In order to satisfy this assumption, the Bond number (Bo) fluid confinement

criterion [24] should be satisfied (see section 3.4.2). For the tested PHP, theoretically, the transition between confined and unconfined flow should occur between 2g and 3g.

7.2.1   Bottom Heated Mode configuration

Taking the PHP in vertical position, tests have been carried out by changing both the heat input and the gravity level: the device is started up at 50W in normal gravity conditions till steady state is reached, then the gravity level is increased and the same heating cycle (50, 70 and 100W) of the ground test is performed; finally the device is shut down. The comparison between experimental and numerical results is reported in Figure 7.9 and Figure 7.10 in term of wall temperature and pressure respectively.
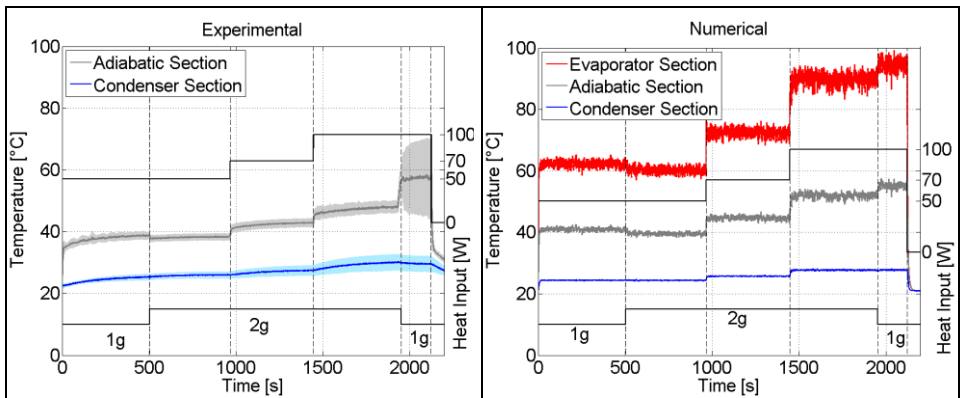
Figure 7.9: Comparison between experimental (left) and numerical (right) wall temperatures for the bottom heated mode PHP at different heat inputs and gravity levels. Solid lines represent the local spatial average wall temperature; colored ranges on the experimental results indicate the standard deviation on the recorded data.
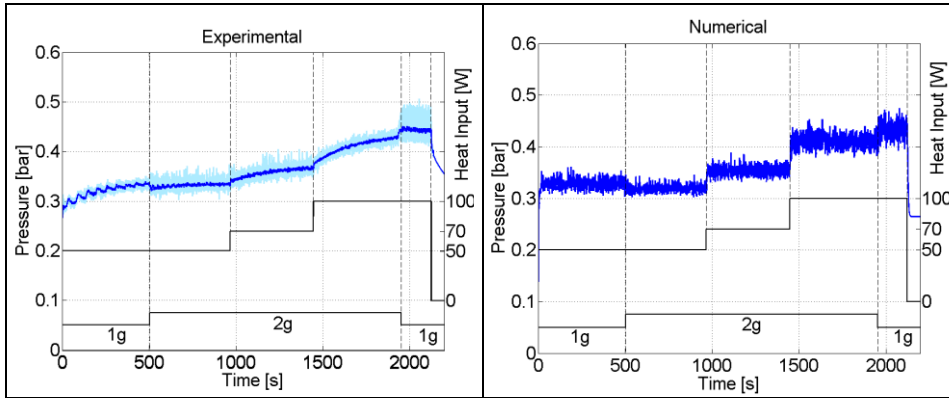
Figure 7.10: Comparison between experimental (left) and numerical (right) pressure for the bottom heated mode PHP at different heat inputs and gravity levels. Solid lines represent the filtered data, colored ranges on the experimental results the non filtered pressure.

When the PHP is oriented in vertical bottom heated position, the acceleration vector is parallel to the flow path, from the condenser to the evaporator zone. Thus, gravity helps the liquid flowing back from the condenser to the evaporator section; this, theoretically, enhances the whole fluidic motion. The experimental data, indeed, show that the PHP is working with slightly better thermal performance at 2g: the average evaporator temperature can be directly compared between 1g and 2g for 50W and 100W and in both cases the temperature is evidently lower.

The same behavior, both in term of temperature levels and transient time, is successfully predicted by the numerical model. The maximum error on the temperature calculation is less than 6%. The same trend can be observed also looking at the pressure signal (Figure 7.10).

Figure 7.11 shows the temperature transition from an already stationary situation at normal gravity to hyper-gravity (2g) conditions for 50W, 70W and 100W. The fluidic element are moving

within the PHP oscillating and circulating. If the circulation velocity increases, the performances of the PHP are enhanced because of the higher efficiency in transporting heat from the hot to the cold zone. Theoretically, the increment of gravity should enhance the circulation of the fluid for a bottom heated PHP.
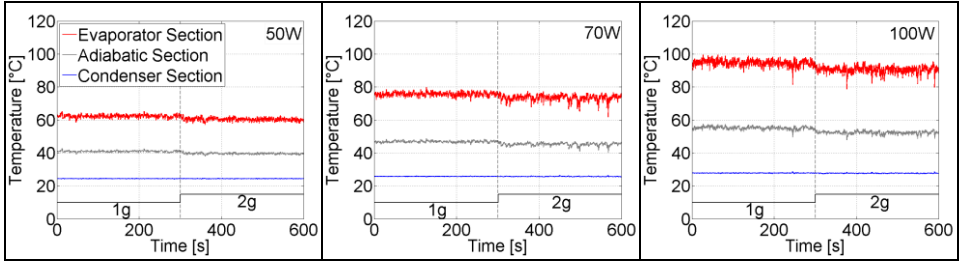
Figure 7.11: Bottom heated mode PHP, spatial average wall temperature at 50 W, 70 W and 100 W. Effects of the gravity change from 1g to 2g.
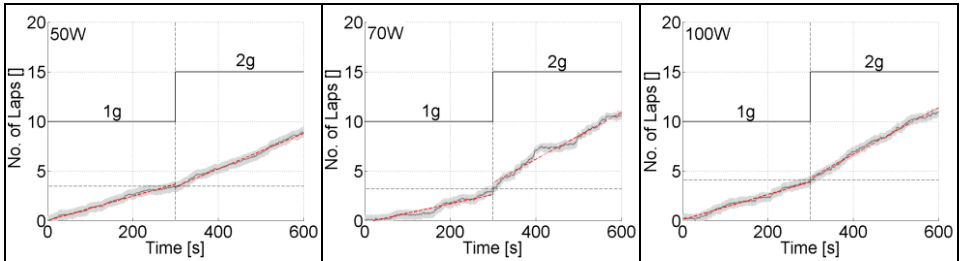
Figure 7.12: Number of round in time at 50W, 70W and 100W in term of mean value (solid line) and dispersion (colored range). Red dotted lines report the linear interpolation curves. Effects of the gravity change from 1g to 2g.

The number of full laps travelled by the fluidic elements and calculated from $t = t0$ (0 in the graphs) is plotted versus time in Figure 7.12, both in term of mean value (solid line) and dispersion (colored range). For example at 50W, on average, the fluidic elements

perform 3.5 full laps between 0s and 300s. The slope associated to each interpolating red curve reported in Figure 7.12 represents the circulation frequency of the fluid in the analyzed conditions. For example, taking the case at 50W, at normal gravity the mean circulation frequency of the fluid is about 0.73rpm. As expected, in all the three tested cases, the circulation frequency, and thus the velocity, increases when passing from 1g to 2g: the frequency value varies from 0.73rpm to 1.07rpm in the case of 50W, from 0.56rpm to 1.41rpm at 70W and from 0.76rpm to 1.41rpm at 100W.

7.2.2 Horizontal configuration

In the case of horizontal configuration, the gravity vector is perpendicular to the flow path, thus the flow motion does not sense directly the increased acceleration. Hence, the performances of the device are not affected by the modification of the gravity level as shown by the experimental data (Figure 7.13).

Figure 7.13: Comparison between experimental (left) and numerical (right) wall temperatures for the horizontal PHP at different heat inputs and gravity levels. Solid lines represent the local spatial average wall temperature; colored ranges on the experimental results indicate the standard deviation on the recorded data.

The same outcome can be observed for the numerical results: since the model is mono-dimensional, indeed, the modification of a force acting perpendicular to the flow path, like gravity, is not accounted for.

7.3   Micro-gravity tests

During the 58th and 59th Parabolic Flight campaigns several experimental tests have been performed on a planar, bottom heated mode PHP partially filled with FC-72 under different operative conditions [31] [32] (chapter 4). Specifically, two different filling ratios (see Table 7.1) and six different power levels have been analyzed, from 50W to 100W with step of 10W.

A parabolic flight allows testing a device under various gravity levels in transient conditions. During each flight, indeed, the plane performs thirty-one parabola which are subdivided into three parts: 20s at 1.8g (hyper-gravity) followed by 22s at 0.01g (micro-gravity) followed again by 20s at 1.8g. A 90s pause of normal gravity is before and after each parabola.

As always, the results are presented mainly in terms of pressure and local spatial average wall temperature evolutions. The grey solid line marks the temperature in the adiabatic zone, the blue line characterizes the condenser region and the green line indicates the temperature of the external environment. The numerical graphs report also a red line for the mean temperature in the evaporator region. The light colored regions on the experimental temperatures represent the standard deviation on the recorded data.

Since the experimental results are repeatable, only one parabola for condition is shown.

7.3.1 58th Parabolic Flight campaign

On flight experiments

Figure 7.14 - Figure 7.17 report the comparison between numerical and experimental data showing the very high prediction capacity of the model both in steady and transient conditions.

The temperatures in all the PHP regions are correctly evaluated in terms of mean values, as well as in terms of temporal trend for all the gravity levels and heat inputs (from 50W to 80W). Hence, the model not only is able to reproduce the stead state performance of the PHP in different gravity levels and under various operative conditions, but at the same time, it is able to reproduce the transient behaviour of the device with high accuracy.
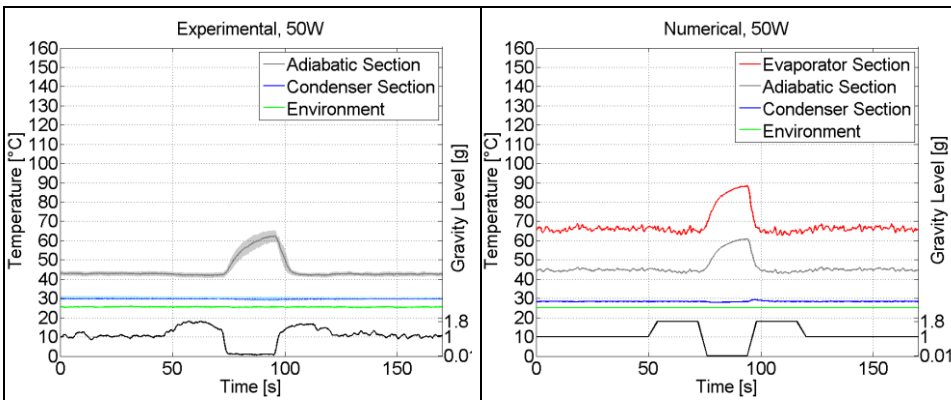
Figure 7.14: Experimental and numerical trend of the local spatial average temperature for a bottom heated mode PHP at 50W. Solid lines represent the mean temperatures, colored region indicate the standard deviation on the recorder data.
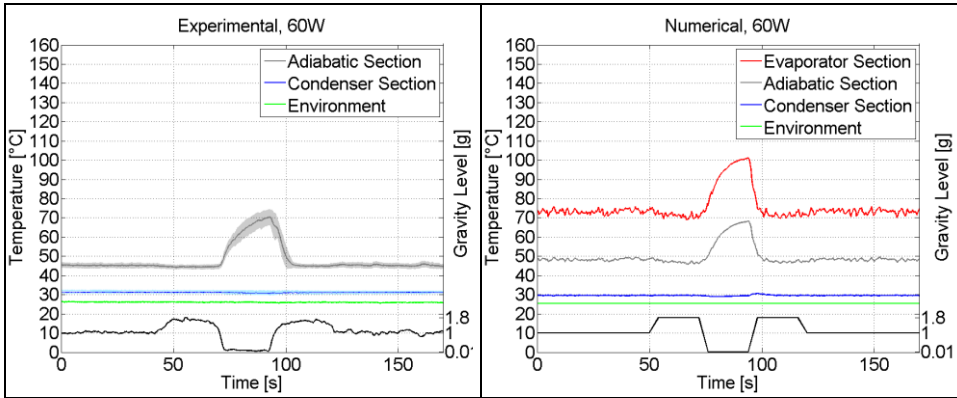
Figure 7.15: Experimental and numerical trend of the local spatial average temperature for a bottom heated mode PHP at 60W. Solid lines represent the mean temperatures, colored region indicate the standard deviation on the recorder data.
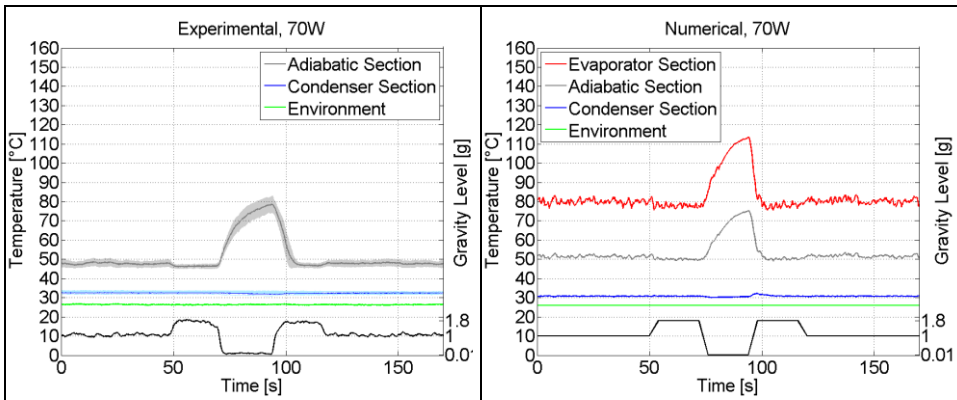
Figure 7.16: Experimental and numerical trend of the local spatial average temperature for a bottom heated mode PHP at 70W. Solid lines represent the mean temperatures, colored region indicate the standard deviation on the recorder data.
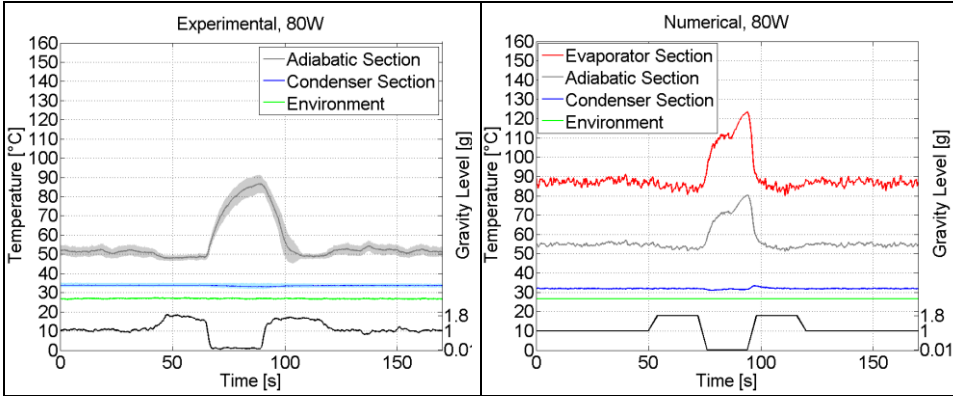
Figure 7.17: Experimental and numerical trend of the local spatial average temperature for a bottom heated mode PHP at 80W. Solid lines represent the mean temperatures, colored region indicate the standard deviation on the recorder data.

At 90W and 100W (Figure 7.18 and Figure 7.19), on the other hand, the error on the mean temperature increases, even if the temporal evolution is followed. The reason of that is twofold: firstly, since slug flow is assumed a priori, the code is not able to model the flow pattern transition in case of high heat fluxes; secondly, liquid film dynamics has been neglected. Experimentally, at high power levels, some PHP branches undergo dry-out, worsening the whole device performances. Figure 7.20 shows an example of this unstable condition reporting all the recorded temperatures for the 100W parabola: dry-out is clearly visible in most part of the PHP branches.
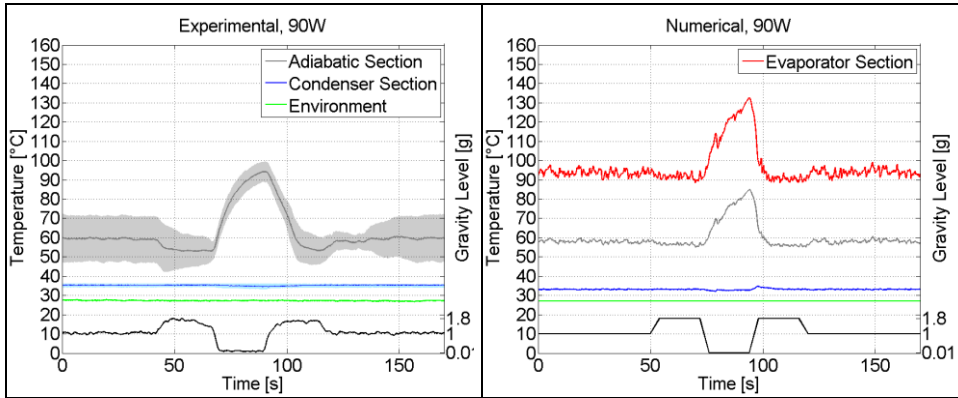
Figure 7.18: Experimental and numerical trend of the local spatial average temperature for a bottom heated mode PHP at 90W. Solid lines represent the mean temperatures, colored region indicate the standard deviation on the recorder data
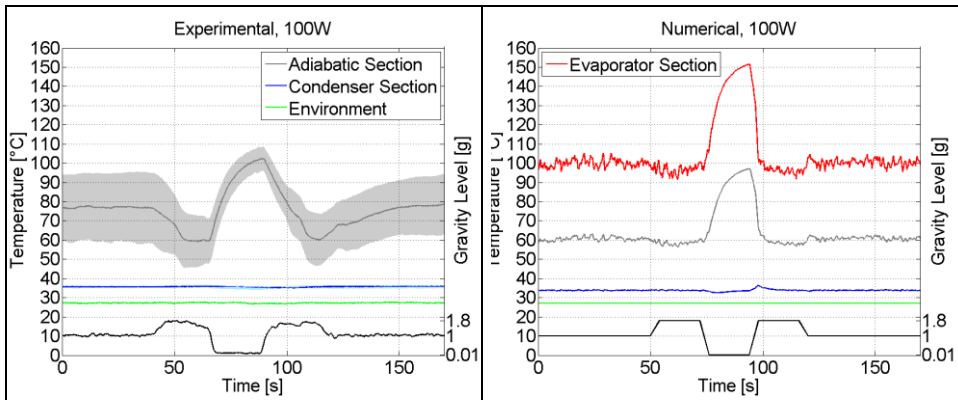
Figure 7.19: Experimental and numerical trend of the local spatial average temperature for a bottom heated mode PHP at 100W. Solid lines represent the mean temperatures, colored region indicate the standard deviation on the recorder data
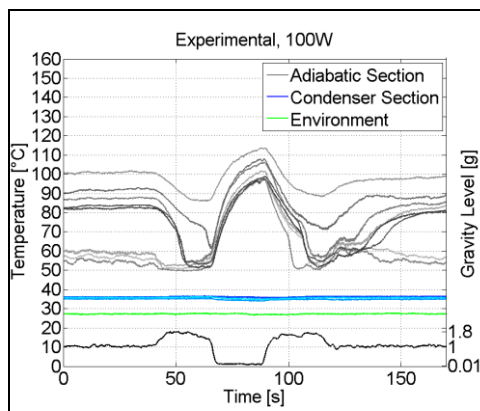
Figure 7.20: Experimental wall temperatures for a bottom heated mode PHP at 100 W. The grayish colors represent the adiabatic zone, the bluish indicate the condenser section.

This sudden thermal crisis is originated by local complete evaporation of the liquid film and consequently reduction of the vapor/wall heat transfer coefficient in the corresponding regions. This instability reduces at high g-levels, since the boosted gravity force slightly improve the whole PHP performances when a bottom heated mode configuration is accounted for, as shown in section 7.2.1 [26] [27]. The circulation of the fluid within the channel, indeed, is promoted because liquid slugs are energetically pushed from the condenser back to the evaporator section; in addition the enhanced gravity induce a downward motion of the liquid film, creating a sort of small pool in the hotter region and, thus, reducing the possibility of local dry-out. Since, the model assumes constant film thickness (assumption 7), this kind of behaviour cannot be detected and, therefore, the simulated temperature may be lower than the experimental data (e.g. 1g at 100W); at the same time, the numerical temperature improvements at 1.8g may be smaller than the real ones (e.g. 1.8g at 90W).

The experimental results show that both the occurring of the hyper and the micro-gravity conditions affect the PHP thermal response. Since the gravity vector is parallel to the flow path and oriented from the condenser to the evaporator zone, it gives a net contribution to the fluid momentum. The effect of micro-gravity is evident for all the heat input levels: temperatures in the evaporator increase because the fluid motion is no more assisted by gravity, pressure oscillations are less frequent (see, for example, Figure 7.21 on the left for the 50W parabola, same results for the other heat inputs) and consequently the heat transfer rate is less efficient. The occurring of the second hyper-gravity period assists the fluid motion bringing back the device to the previous thermal regime. This explanation is also confirmed by the numerical results. Figure 7.21, on the right, shows the fluid pressure for the PHP simulated at 50W. Similar results have been achieved for the other power levels.
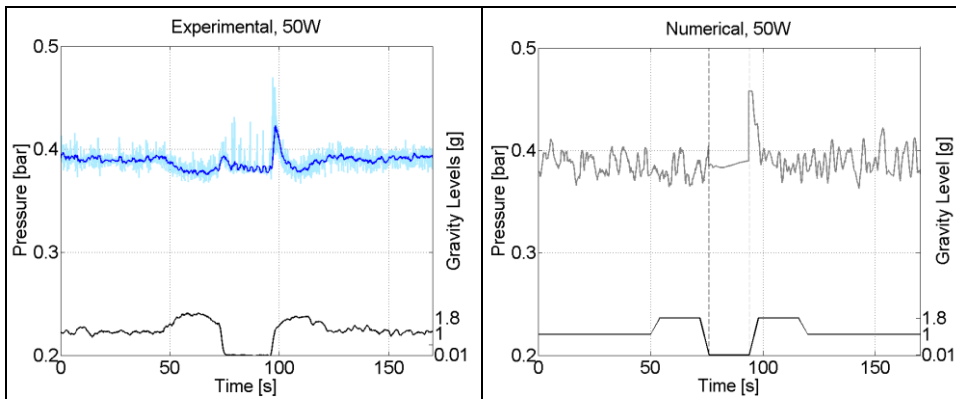
Figure 7.21: Experimental (left) and numerical (right) pressure signal for the 50W parabola. Solid lines represent the filtered data, while colored ranges on the experimental results indicate the non filtered recorded pressure.

Although the pressure signal is damped with respect to the experimental one, in both cases the oscillations of the signal reduce when micro-gravity conditions are established; then they are restored with an high isolated pick when 1.8g are applied on the PHP again.
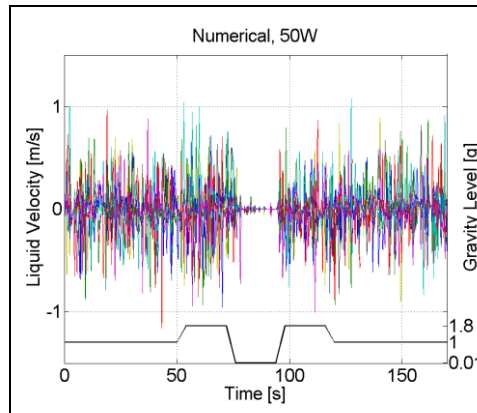
Figure 7.22: Numerical computed liquid slugs velocities for the 50 W parabola. Different colors indicate different elements.

It is worth to note that the internal motion does not stop during these 20s: Figure 7.22 shows the velocity of the liquid elements within the channel. During the micro-gravity phase, the velocity suddenly decreases but small oscillations are still present.

Liquid elements move within the micro-channel. The total velocities reported in Figure 7.22 account for both oscillation and circulation. During the micro-gravity phase, only the circulating velocity reduces to zero, while the oscillating one is still present even if it is strongly reduced. This can be easily inferred from Figure 7.23. It shows the number of laps performed, on average, by the fluidic elements during the simulation time. The slope associated to each interpolating red curve represents the mean circulation frequency of the fluid in the analyzed conditions. The fluctuations on the gray

curve underline that the fluid is strongly oscillating when gravity is acting. As expected the circulation frequency, and thus the circulation velocity, increases when passing from 1g to 1.8g and from 0.01g to 1.8g. This enhances the PHP performances. During the micro-gravity period, instead, the circulation of the fluid stops, being the red curve horizontal.
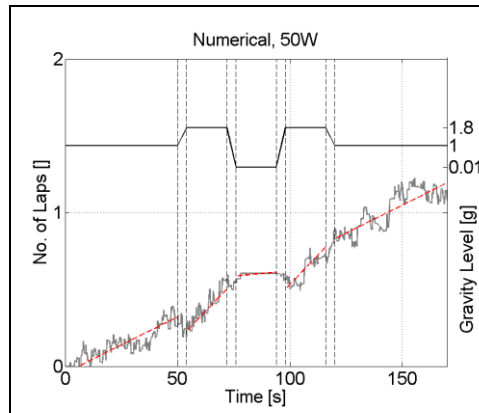
Figure 7.23: Numerical computed liquid slugs velocities for the 50 W parabola. Different colors indicate different elements.

Ground tilting experiments

Mameli et al. [31] reported that the dynamic response of the PHP during a parabola test is comparable with the behavior of the PHP on ground during one "Vertical to Horizontal to Vertical" maneuver. The maximum temperatures reached during micro-gravity and during the horizontal period on ground were comparable for all the heat inputs.
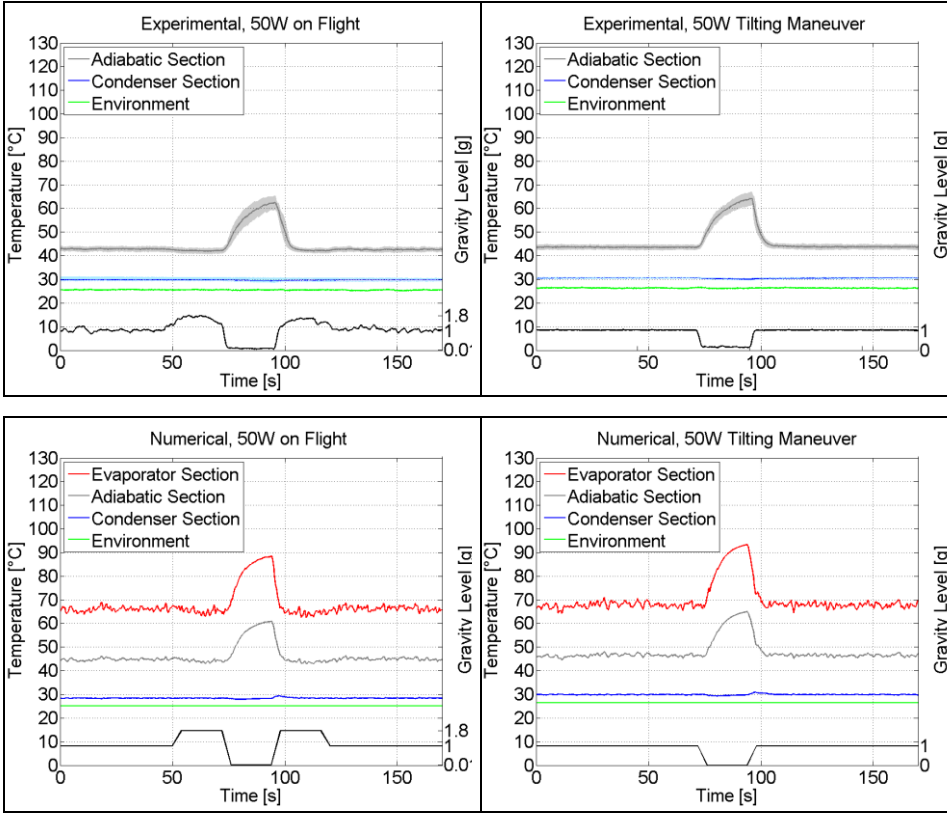
Figure 7.24: Experimental (top) and numerical (bottom) trend of the local spatial average temperature for the 50 W parabola (on the left) and the 50 W tilting maneuver (on the right). Solid lines represent the mean temperatures, colored region indicate the standard deviation on the recorder data.

The same happens when this tilting "Vertical to Horizontal to Vertical" maneuver is numerically simulated; see, for example, Figure 7.24 corresponding to the 50W test. Similar results have been achieved for the other heat inputs.
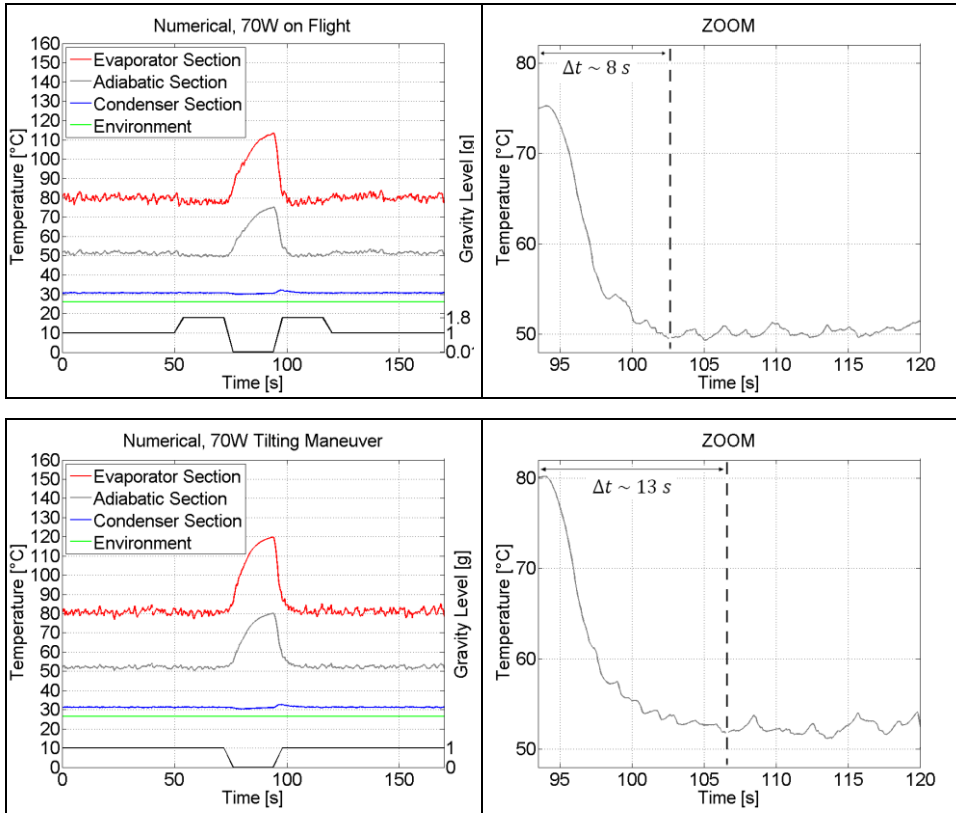
Figure 7.25: Numerical trend of the local spatial average wall temperature for the 70 W parabola (top) and the 70W tilting maneuver (bottom). On the right, zoom of the adiabatic temperature in the transition zone.

The numerical simulations, as well as the experimental test, observe a small temperature increment during the micro-gravity phase for the ground tests with respect to the flight trials. In the reported case of 50W this deviation is less than 4%. However this temperature gap is easily explainable: the lack of the first hyper-gravity phase fastens the degradation of the PHP performance during the 20s of micro-gravity.

155

In addition, as experimentally observed, due to the lack of the second hyper-gravity phase, the device is not able to recover the previous thermal regime as fast as during the flight. This happen at all the power levels, however it is more evident for high heat input values. The comparison of the results achieved at 70W is reported here as an example to support this last statement (Figure 7.25).

7.3.2   59th Parabolic Flight campaign

On flight experiments

During the 59th Parabolic Flight campaign, the same PHP tested in a bottom heated mode position during the previous experimental works has been tested again with a different filling ratio, 70%.
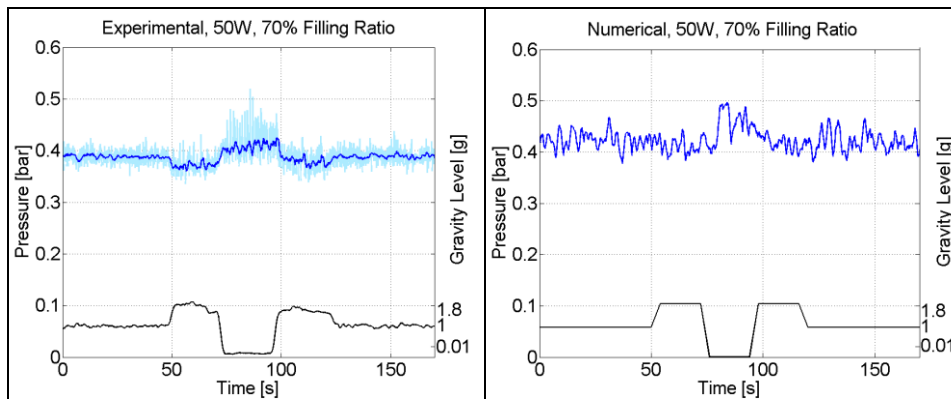
Figure 7.26: Experimental (left) and numerical (right) pressure signal for the 50W parabola; 70% filling ratio PHP. Solid lines represent the filtered data, while colored ranges on the experimental results indicate the non filtered recorded pressure.

This means that a 20% more of liquid is present within the capillary tube. This modification has effects on both the dynamic of the system

(Figure 7.26), which is less influenced by micro-gravity, and on the thermal performance of the whole device (Figure 7.27).
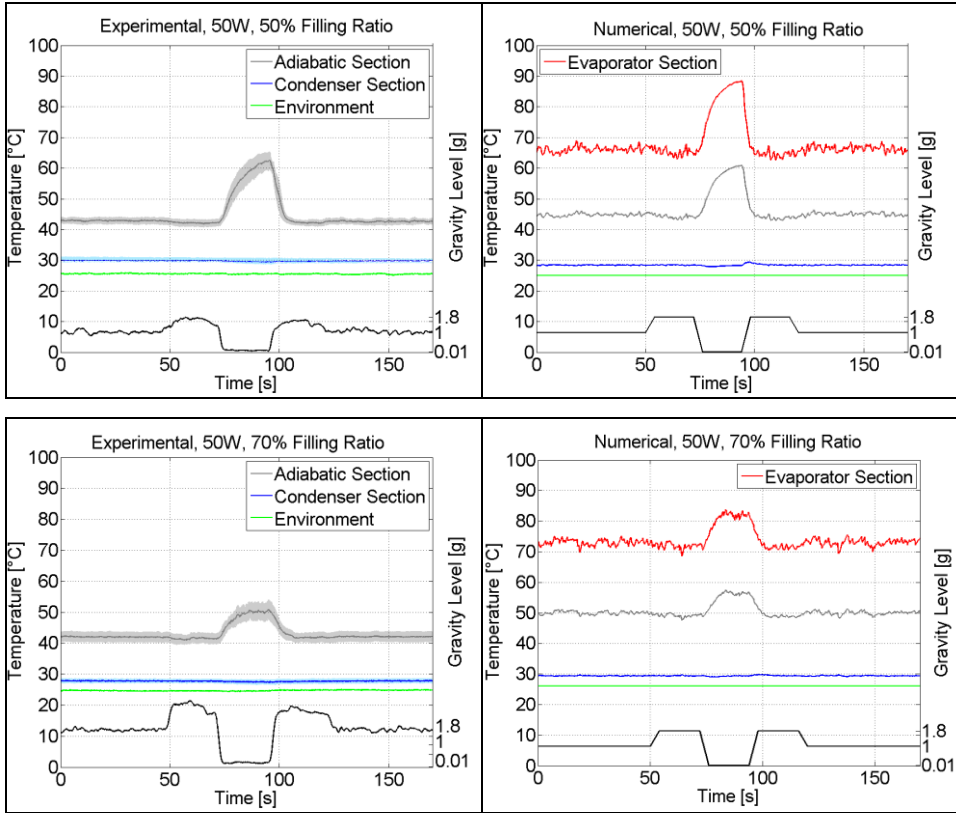
Figure 7.27: Experimental and numerical wall temperatures for a bottom heated mode PHP at 50W; 50% filling ratio (top), 70% filling ratio (bottom). Solid lines represent the mean temperatures, colored region indicate the standard deviation on the recorder data.

Since liquid has better heat transfer properties than vapor, the global wall/fluid heat transfer coefficient is enhanced slightly improving the behaviour of the entire system. During the normal gravity phase, indeed, the mean temperature reached in the adiabatic zone is 1 or

2K lower with respect the same test performed with the 50% of filling ratio.

The numerical model is able to correctly reproduce the dynamic of the system. Figure 7.27 shows a comparison between the 50% (top) and 70% (bottom) filling ratio PHP, in term of experimental and numerical temperatures for the 50W parabola. Same results have been achieved for all the other power inputs. It is clearly visible that, during the micro-gravity phase, the temperature level in the adiabatic zone for the 70% PHP reaches a sort of equilibrium plateau characterized by a higher temperature with respect normal gravity, but evidently lower and more stable with respect the 50% PHP. At the same time, the pressure signal (Figure 7.26), which was damped for the 50% PHP, continues to oscillate for the 70% PHP meaning that the fluid is still circulating even if gravity has been reduced, as indicated also by the computed velocities (Figure 7.28).
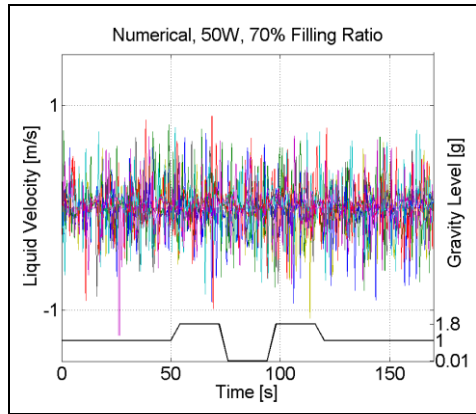
Figure 7.28: Numerical computed liquid slugs velocities for the 50 W parabola; 70% filling ratio PHP. Different colors indicate different elements.

This happens because, statistically, it is more probable for the 70% PHP to have liquid in the evaporator turns during micro-gravity and thus generation of new vapor elements. The disequilibrium linked to evaporation processes guarantees the fluidic motion. The same trend is correctly reproduced by the numerical model both for pressure and temperature.

Unfortunately, the model over estimates the temperature level in the hotter region of about 7 K. Since the inner dynamic of the device is well predicted, the problem should lie in the definition of the sensible heat transfer coefficients between fluidic and wall domains. Specifically, since the model cannot catch the improved performance of a PHP filled with more liquid, it is plausible that the application of the classical empirical formula for the estimation of the wall/liquid sensible heat transfer coefficients (i.e. Shah and London, Gnielinski, and Dittus-Boelter correlations) should be revised and improved with a fitting correlation as already done for the vapor/wall case. Actually, the definition of the correct heat transferred between the wall and the fluid remains a critical and delicate point: since literature does not report any specific formula derived for a two-phase flow oscillating in mini/micro channels, the use of fitting correlations is the best that can be done to developed validated numerical tool for PHPs simulation. Similarly, it is also probable that the definition of the vapor/wall heat transfer coefficient should account directly for the liquid film thickness, while, at the present, Eq. (6.55) is computed for a conventional film thickness of 50 μm. The augmented filling ratios, indeed, lead to bigger δ; since $Ra \propto \delta$, augmented filling ratios lead also to bigger Ra and thus higher heat transfer coefficients. Therefore, the computed temperatures should decrease proportionally, bettering the predictions of the model.

Chapter 8

8. Sensitivity analysis: influence of the tube features

PHPs are the last frontier of the two-phase passive heat transfer devices; however in order to spread their application, the present knowhow must be enlarged through experimental researches or simulating various possible scenari by means of numerical codes. In this prospective, the model proposed in the previous chapters gains a crucial importance. Indeed, it represents a validated, powerful tool able to complete and support experimental studies, helping the

design of new and better performing devices with limited requires in term of time, working force and resources.

To provide the readers an evidence of what asserted right now, in the following, the novel numerical tool will be used to study the influence of the tube characteristics (i.e. materials, diameters, no. of turns) on the global thermal performance of the lab-scale PHP experimentally analyzed in chapter 3 and 4 (Table 8.1 and Table 8.2).
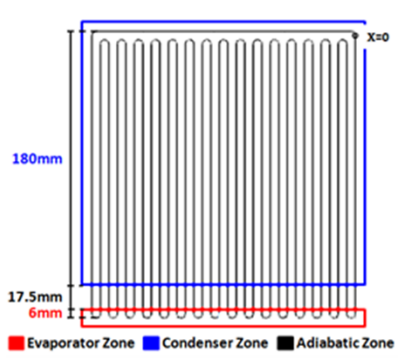
Input fixed parameter	Value
Working fluid	FC-72
Volumetric filling ratio	0.5
Configuration	BHM*
Surface roughness	50μm
Total length	6.62m
Gravity	0.01g - 2g
External temperature	294K

* Bottom Heated Mode

Table 8.1: Principal fixed features of the analyzed PHP.

Input variable parameter	Value
Wall material	Copper, PET, Aluminum, Steel, Silicon
Inner/Outer diameter	0.5/1.4, 0.8/1.7, 1.1/2.0, 1.3/2.2, 1.6/2.5mm
No. of evaporator bends	2, 4, 8, 16
Heat flux	3.5, 4.5, 6.5 W/cm²

Table 8.2: Inputs changed during the performed sensitivity analysis.

8.1   Wall materials

The first analysis focuses on the effects of the wall material on the PHP thermal performances. Table 8.3 resumes the principal thermo-

physical properties of copper, aluminum, PET, silicon and steel. Among them, copper shows the maximum thermal conductivity and high heat capacity per unit volume ($C = \rho C_v$), while PET is a good insulator and presents the minimum thermal inertia. Steel, instead, represents a peculiar material: it shows the maximum thermal inertia, because of the high density and specific heat, but it is characterized by poor conductive properties.

	Cu	Al	Si	Steel	PET
k_w, [Wm^{-1}K^{-1}]	390	237	148	13.8	0.2
ρ, [kgm^{-3}]	8920	2700	2330	7900	1370
C_V, [Jkg^{-1}K^{-1}]	385	910	700	500	1000
ρC_V, [Jcm^{-3}K^{-1}]	3.43	2.46	1.63	3.95	1.37

Table 8.3: Wall material principal properties.

Three different heat fluxes have been analyzed: 3.5, 4.5 and 6.5W/cm². Results are presented in terms of local average temperature for a PHP with inner/outer diameter of, respectively, 1.1/2.0mm and 16 turns in the evaporator zone (Figure 8.1). The other tested configurations show similar trends and will not be reported. Blue lines represent the condenser section, red lines the evaporator zone. The start-up time (presented in form of characteristic time, 3τ) is also indicated above each graph: it represent the time requested by the ideal device to reach the 95% of the steady state mean temperature. Ideal device refers to the PHP serpentine only: the thermal inertia of the peripheral elements (i.e. cooling and heating systems) is not accounted for.
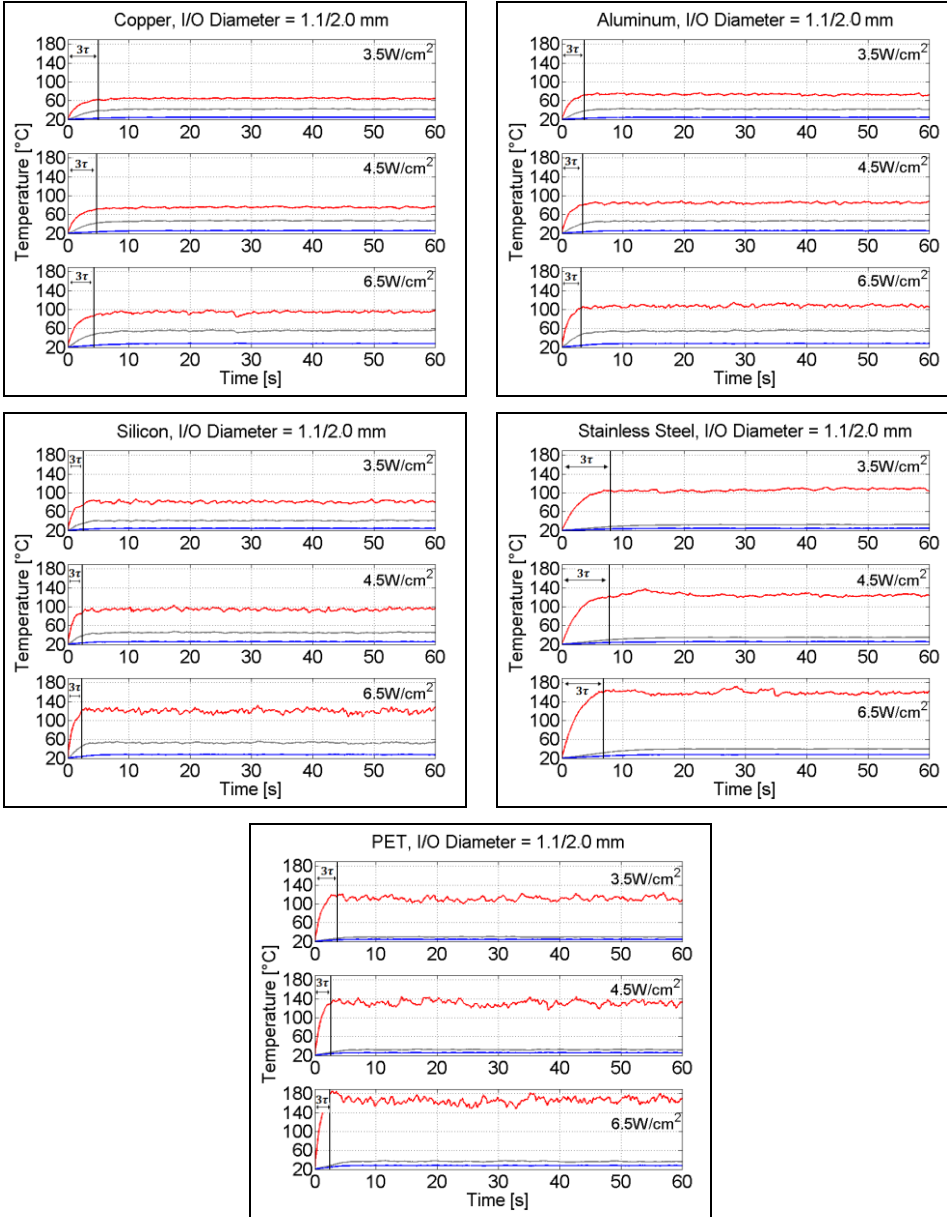
Figure 8.1: Local mean temperatures in the evaporator (red line) and condenser (blue line) for different materials and heat fluxes. Inner/outer (I/O) diameter = 1.1/2.0mm.

It is important to note that even if the melting temperature of PET is 260°C, it starts softening at 90°C; in addition the gas permeability of polymers increases with the temperature level. Therefore the results hereby shown for the plastic device are a merely numerical effort to point out the influence of the wall properties on the PHP performance. The real application of PET for such high heat fluxes, indeed, could be problematic since the temperature in the evaporator region overcome 100°C.

Figure 8.1 clearly shows that higher wall conductivities improve the thermal performances of the system; high wall conductivities, indeed, mean that not only the fluid is transporting heat, but part of the energy provided in the evaporator zone move through the wall thickness towards the condenser making the axial temperatures more uniform.
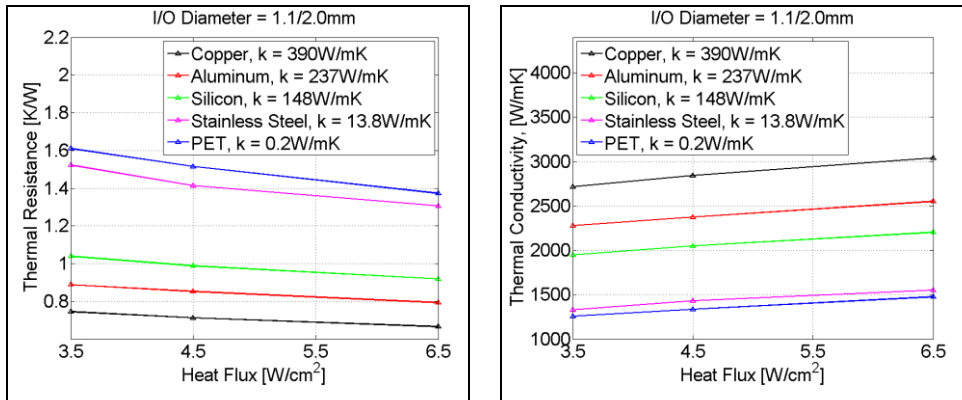
Figure 8.2: Equivalent thermal resistance (on the left) and conductivity (on the right) for different heat fluxes at the evaporator region and different wall materials. Inner/outer (I/O) diameter = 1.1/2.0mm, 16 turns.

The same conclusion can be inferred from the analysis of the equivalent thermal resistance, $R_{eq} = (T_{max} - T_{min})/Q_{ex}$, and

conductivity, $k_{eq} = L/(N_{turns}\pi r_{ex}^2 R_{eq})$, reported in Figure 8.2: the copper, the aluminum and the silicon PHP are the best performing ones, while PET and stainless steel behaves as insulating means doubling the global thermal resistance of the system.

Moreover, one can point out that the presence of the internal two-phase flow within the device strongly enhances the thermal performance of the empty system. Figure 8.3 reports the ratio between the PHP k_{eq} and the nominal conductivity of the bulk material: one can see that the fluidic motion within the PHP may increase the conductivity of copper[19], aluminum and silicon of a factor ~10, for stainless steel of a factor ~100, while for the polymeric device the increment is of about 7000 times!
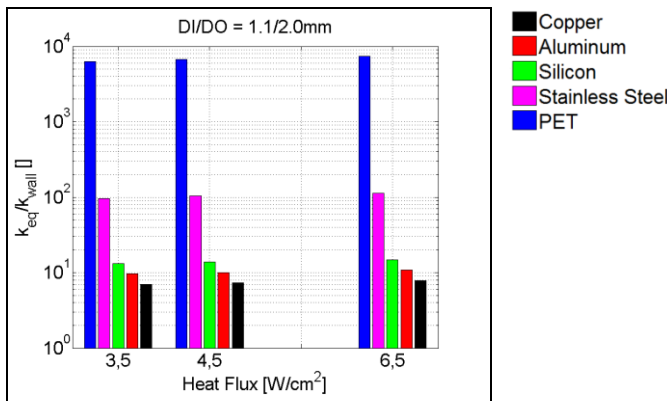
Figure 8.3: PHP k_{eq} over wall k at various heat fluxes at the evaporator region for different wall materials. Inner/outer (I/O) diameter = 1.1/2.0mm, 16 turns.

---

[19] Note that this increment (~10) may seem higher than the one pointed one in Chapter 1 comparing a block copper and a PHP (~2.5). However these results are non contradictory because the equivalent conductivity in Figure 8.2 has not been calculated over a rectangular area (like in Chapter 1), but over the equivalent area of the 32 circular channels which is ~4 times lower.

Figure 8.2 also shows that the performances of the device are improved if higher heat fluxes are provided at the evaporator zone. This is also proven by several experimental studies (e.g. Charoensawan et al. [25], Karthikeyan et al [108]). The heat provided at the evaporator is actually the driving motor of the system inducing oscillations and circulation of the fluid within the capillary channel: thus, higher the thermal load is, higher the fluidic motion is and thus the PHP global heat transfer capability. For the same reason, the start-up time of the ideal PHP reduces when the heat flux increases from 3.5W/cm² to 6.5W/cm² (Figure 8.4).
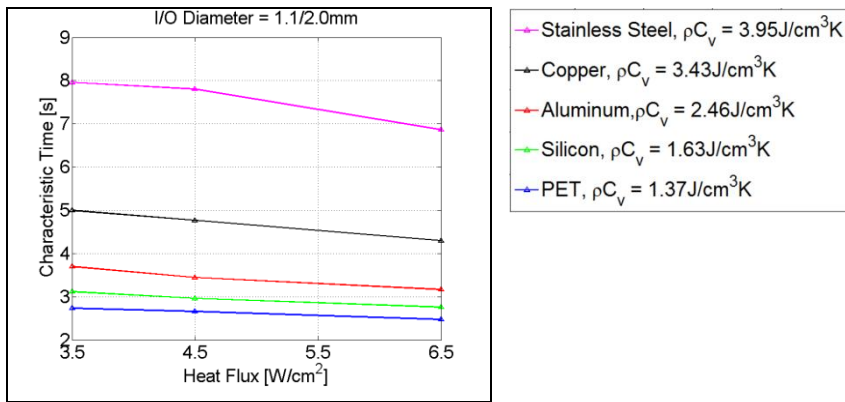
Figure 8.4: Ideal PHP star-up time vs. heat flux at the evaporator region for different wall materials. Inner/outer (I/O) = 1.1/2.0mm, 16 turns.

Figure 8.1 and Figure 8.4 underline also that the wall properties condition the dynamic response of the device. The start-up time and the temperature oscillations established during the steady state are, indeed, influenced by the thermal inertia of the tube material. Specifically, since the thermal inertia of a system is proportional to its heat capacity, a smaller ρC_V (i.e. Silicon or PET) fastens the temporal response.

Therefore, if copper is the best choice in terms of temperature levels and stable trends in steady state (low oscillations), PET is preferable, if quick start-ups are requested. Since silicon and aluminum shows intermediate characteristics, they represent the best compromise between these two needs. On the other hand, stainless steel behaves as insulator and has the lengthy star-up time.

8.2   Internal and external diameter

The second analysis focuses on the influence of the internal and external diameters on the PHP thermal performances. Results are shown for five simulated PHPs characterized by inner/outer diameters respectively of 0.5/1.4mm, 0.8/1.7mm, 1.1/2.0mm, 1.3/2.2mm and 1.6/2.5mm. The first one is representative of a micro-channel PHP, while the last one simulates a PHP near its capillary limit; the internal diameter of 1.6mm, indeed, is closed to the critical value calculated with the fluid confinement criterion [24] for FC-72 at temperatures ranging from 20°C to 100°C. For all the analyzed cases, the tube wall thickness has been kept constant (0.45mm) and 16 evaporator turns are accounted for.

Figure 8.5 shows, on the left, the thermal resistance of the PHP when 4.5W/cm² are provided at the evaporator region. The other tested configurations ($q^{"}$= 3.5W/cm² and 6.5W/cm²) have similar trends. Again, coherently with the results presented in the previous section, copper shows the best thermal performance, while PET is associated to the maximum thermal resistance. In addition, Figure 8.5 underlines a monotonic reduction of R_{eq} when the tube diameter is enlarged, as reported by several experimental results (e.g. Charoensawan et al. [25], Sangiamsuk et al. [109]). This is expected since R_{eq} is inversely proportional to evaporator area, and, therefore, to the tube diameter:

$$\begin{cases} R_{eq} = \dfrac{(T_{max}-T_{min})}{Q_{ex}} \\ Q_{ex} = q_{ex}(2\pi r_{ex} N_{turns} L_{ev}) \end{cases} \rightarrow \quad R_{eq} = \dfrac{(T_{max}-T_{min})}{q_{ex}(2\pi r_{ex} N_{turns} L_{ev})} \qquad (8.1)$$
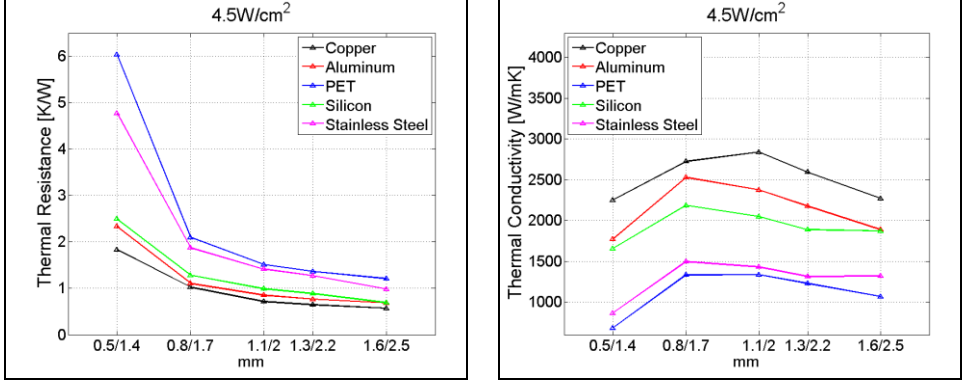
Figure 8.5: Equivalent thermal resistance (on the left) and conductivity (on the right) for different inner/outer diameters and different wall materials. q_{ex} = 4.5W/cm², 16 turns.

However, if the equivalent thermal conductivity is taken as quality factor of the system, the things are slightly different, as pointed out by Figure 8.5 on the right. An optimum combination of inner/outer diameters exists between the two extreme tested conditions[20] (i.e. micro-channel and critical diameter).

When the channel is too small, indeed, the shear friction is remarkable damping the motion of the fluid (see the example of the copper PHP in Figure 8.6, similar results for the other materials) and, thus, lowering the thermal performance of the device. This is confirmed also by ground experiments carried out by Qu et al. [110] with a silicon-based micro-PHP: the authors assert that the bulk

---

[20] For the tested configurations, the best combination lays between 0.8/1.7 and 1.1/2.0mm.

circulation disappears when the PHP internal diameter reduces below a critical value.
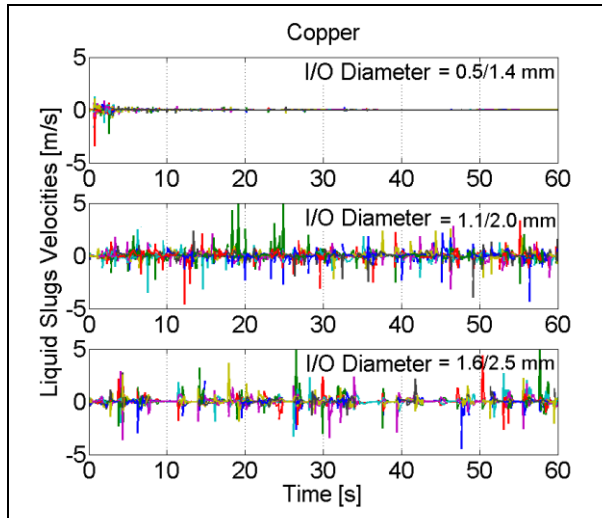
Figure 8.6: Liquid slug velocities in time for three different diameters (minimum, medium and maximum values). Copper PHP, q_{ex} = 4.5W/cm², 16 turns. Different colours describe different slugs

On the other hand, if the diameter is too large, at the same heat flux, the generation of new plugs is limited since a big amount of vapor is requested to fulfill the entire channel; again, the reduced number of vapor elements damps the global motion and worsens the thermal performance of the system (Figure 8.7). Note that, when the channel is very small, bubbles are generated near the evaporator turns; since the fluid is not moving, vapor elements are not driven away from their birth positions; thus, after an assessment time, the number of bubbles remains constant and closed to the number of evaporator bends.
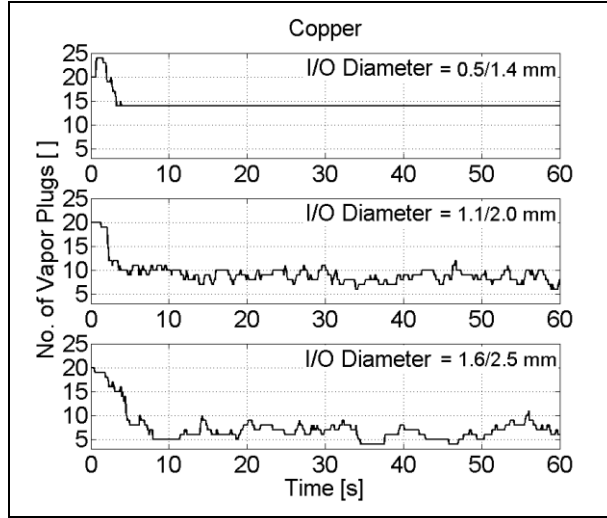
Figure 8.7: Number of vapor plugs in time for three different diameters (minimum, medium and maximum values). Copper PHP, q_{ex} = 4.5W/cm², 16 turns.

8.3 Number of turns

The last analysis focuses on the number of turns in the PHP serpentine. Devices with 2, 4, 8 and 16 bends in the evaporator region have been simulated to point out the differences in their thermal response. The PHP configuration characterized by inner/outer diameters of 1.1/2.0mm has been accounted for providing 4.5W/cm² at the evaporator region. Different materials have been taken into account.

Figure 8.8 shows the equivalent thermal resistance and the equivalent thermal conductivity of the system respectively.

R_{eq} reduces monotonically with the number of turns [25], [108]. As for the diameter case (see section 8.2), this is quite expected since R_{eq} is inversely proportional to the total evaporator area which increases if the system has a higher number of bends, Eq. (8.1).

On the other hand, an optimum number of turns exists if the attention is paid on the conductivity. Two opposite effects are, actually, related to the turns increment: 1) the intensification of the minor friction losses and thus the damping of the fluid motion; 2) the boost of the level of internal perturbations [25] and consequently of the fluid motion. Thus, the desirable design criterion may be searched between these two opposite effects, but generally, a higher number of turns is preferable. This kind of behavior is quite independent on the wall material.
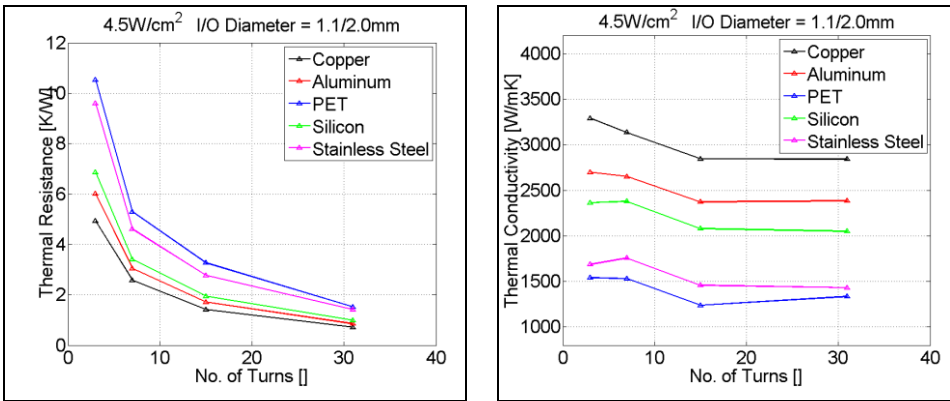
Figure 8.8: Equivalent thermal resistance (on the left) and conductivity (on the right) for different number of turns and wall materials. q_{ex} = 4.5W/cm², inner/outer (I/O) diameters = 1.1/2.0mm.

Chapter 9

9. Conclusions and future developments

The work proposed in the previous chapters has a twofold porpoise: first of all it aims to provide information about the influence that gravity has on PHPs performance; on the other hand, it heads for the development of a numerical tool able to simulate the thermal-hydraulic behaviour of PHPs in steady as well as in transient operative conditions.

9.1 Experimental activity

In order to fulfil the first aim, experimental campaigns have been conducted in various gravity conditions on a multi-turn, closed loop PHP. The ESA ESTEC LDC allowed reproducing augmented gravity fields (ESA Educational project Spin Your Thesis! 2013, [26] [27]), while reduced gravity has been recreated on board of the ESA-NoveSpace Airbus A300 Zero-G flying parabolic trajectories (58th and 59th ESA Parabolic Flight Campaigns, [31] [32]). For the first time, a planar PHP with circular cross section channels, equipped with 14 thermocouples and a pressure transducer has been fully, thermally characterized in several operative conditions from 0.01g to 20g both in bottom heated and horizontal configurations.

The temporal trend of the wall temperature in several locations and the local fluid pressure signal showed that the thermal response of a planar PHP is strongly and rapidly affected by variations of the gravity field, especially if gravity acts along the fluid path direction. In particular:

- During parabolic flights, only the vertical operation was affected by gravity variations: hyper-gravity (1.8g) slightly assisted the flow motion, while during micro-gravity (0.01g) the PHP sensed a sudden temperature increase in the evaporator zone recovered by the following hyper-gravity phase. Higher filling ratios slightly mitigated this performance detriment. Comparisons with ground experiments underlined that the thermal dynamic response to the occurrence of micro-gravity resembles the thermal dynamic response of tilting maneuvers (vertical-horizontal-vertical) carried out on ground. Finally, because of the planar layout, horizontal responses in normal gravity perfectly resembled micro-gravity operations.

– The LDC experiments showed that the effects of hyper-gravity on PHPs performance depends on the combined effect of gravity and heat input. Hyper-gravity could produce stratifications, and consequent thermal crises, on the horizontal PHP. During vertical operations, instead, lower hyper-gravity levels slightly improved the whole thermal performance, while further enhancement drove to two different local thermal crises. If the fluid pumping forces, resulting from the heating power, were able to compete with the acceleration forces, the system only sensed local frequent stopover phenomena, while increasing with the acceleration level, the pumping forces were completely damped in some channels, the relative wall temperatures increased and settled to higher levels.

9.2 Numerical model

In order to fulfill the second goal, a new, advance, mono-dimensional, lumped parameter code has been proposed. It consists of a two-phase separated flow model applicable to a confined operating regime, meaning that capillary slug flow is assumed a priori. A complete set of balance differential equations (mass, momentum and energy) accounts for thermal and fluid-dynamic phenomena. The main originalities lay in the suppression of the standard assumption of saturated vapor plugs as well as in the consequent embedding of heterogeneous and homogeneous phase changes directly evaluated in the ODE system. In addition, to account for the influence of the liquid film on the conjugate heat transfer, a novel correlation for the estimation of the wall/vapor heat transfer coefficients has been introduced and tuned up by comparison with experimental data.

The model has been validated in several operative conditions and under various gravity levels (from 0.01g to 2g) against data achieved during the previous experimental campaigns. The results emphasize the high prediction capability of the tool, which represents a step forward in PHPs modeling. The numerical code is able to reproduce with high accuracy both the stationary values and the transient evolution of the wall temperature experienced by the PHP during its operation as well as the internal fluidynamic.

In the case of vertical operations, the thermal performance of the PHP, both in term of temperature value and transient time, have been well reproduced for all the gravity levels. The model is able to catch the performance improvement during hyper-gravity, as well as the detriment during micro-gravity. The maximum error on the temperature prediction is less than 6% when the filling ratio is 0.5, while higher errors (~15%), probably connected to a wrong estimation of the wall/vapor or wall/liquid heat transfer coefficients, appear for the 70% PHP. In addition, for both the 50% and 70% PHPs, the model is able to predict the internal dynamic of the fluid as confirmed by the simulated pressure trends which are aligned with the experimental data. The FFT analysis performed on experimental and numerical signals does not indicate any dominant frequency, underling that the model is not introducing artificial dynamics.

Also in case of horizontal operations, the temperature trends predicted by the numerical model match with the experimental data. Nevertheless, the model damps pressure oscillations when steady-state is reached: the damping effects may derive both from the numerical method adopted for the computation of the liquid momentum (Verlet algorithm) and from the hierarchical numerical procedure used to implement phase changes processes. The vertical configuration does not suffer this problem since the presence of gravity opposes such kind of numerical stabilization.

9.3   Future developments

Concerning the numerical activity, although the proposed model represents a promising advanced tool for designing a capillary closed loop PHPs, there are still possible improvements.

From the modeling point of view, the numerical stability of the code, for example, should be mitigated in order to reduce the artificial damping of the fluidynamic detected in horizontal mode. Moreover, up to now, the film thickness has been neglected introducing a very strong assumption. Since the liquid film dynamic is essential to correctly reproduce the vapor conjugate heat transfer coefficients, as well as dry-out phenomena, it should be modeled and compared with experimental results. In addition the correlation used for the estimation of vapor/wall heat transfer coefficients has been tuned against experimental data from FC-72 only; comparisons with other working fluids should be performed. Finally the start up phase should be improved and the transition between different flow patterns should be implemented in order to surpass the strong common simplification of slug flow. In fact, after the start-up phase, the Bond number criterion alone may not be sufficient to define the fluid confinement: when the fluid motion is activated, inertial and viscous effects may be dominant over the capillarity depending on the liquid and vapor interfacial velocity. The Garimella criterion [111] applied, for example, to the tested PHP states that, if gravity acts, perfect slug flow is not anymore vouched for as soon as the fluid starts moving, underling the criticality of the above mentioned assumption.

From the numerical optimization point of view, instead, further actions should be undertaken in order to reduce the computational running time making the tool even more interesting for parametrical analyses directed to industrial designs. An example above the other is

177

the possible implementation of an adaptive time step which may strongly increase the numerical efficiency of the whole code.

Finally, in order to surpass the limitations of lumped parameter codes, a VOF approach may be accounted for. However, literature evidences that, up to now, the requested computational costs are excessive if one aims to model the entire PHP in 3D. Nevertheless, one can try 2D approaches or focus only on single branches, or even part of them, using a 3D modelling. This allows reproducing and studying micro-scale phenomena (e.g. bubble dynamics, liquid film dynamics) which are difficult to be characterized experimentally, but, at the same time, are fundamental for PHPs performances and operative limits. The comprehension of all these phenomena is of particular importance if the final goal is the design of better performing PHPs able to work even in critical conditions.

Regarding the experimental activity, further analyses should be performed in modified gravity changing the experimental set-up (e.g. working fluids, wall materials, internal and external diameters) in order to study the effect of these constructive parameters on the device thermal performance and to provide extra data to validate the proposed lumped parameter model. In addition, experiments on transparent or partially transparent PHPs should be performed to characterize the flow patterns in various gravity environments and capture micro-scale phenomena, as well as peculiarities of the device in several operating conditions. The recorded data should be use to validate VOF codes, as well as to provide evidences for the specific response that PHPs show during gravity transitions. Finally, experiments able to measure the heat transfer coefficients for liquid and vapor elements in oscillating capillary flow could be interesting since classical correlations difficulty are applicable to two-phase oscillating systems, such as PHPs, where a preferable direction of motion cannot be easily identify.

Acknowledgements

List of publications

International journals

1. <u>Manzoni, M.</u>, Mameli, M., de Falco, C., Araneo, L., Filippeschi, S., and Marengo, M. (2016). Advanced numerical method for a thermally induced slug flow: application to a capillary Closed Loop Pulsating Heat Pipe. *Accepted for publication in Int. Journal of Numerical Methods in Fluids*, 2016.
2. <u>Manzoni, M.</u>, Mameli, M., de Falco, C., Araneo, L., Filippeschi, S., and Marengo, M. (2016). Non equilibrium lumped parameter model for Pulsating Heat Pipe: validation in normal and hyper-gravity conditions. *Accepted for publication in Int. Journal of Heat and Mass Transfer*, 2016.
3. Mameli, M., <u>Manzoni, M.,</u> Araneo, L., Filippeschi, S., & Marengo, M. (2015) Pulsating Heat Pipe in hyper-gravity conditions, *Accepted for publication in Heat Pipe Science and Technology.*

4. Creatini, F., Guidi, G.M., Belfi, F., Cicero, G., Fioriti, D., Di Prizio, D., Piacquadio, S., Becatti, G., Orlandini, G., Frigerio, A., Fontanesi, S., Nannipieri, P., Rognini, M., Morganti, N., Filippeschi, S., Di Marco, P., Fanucci, L., Baronti, F., Mameli, M., <u>Manzoni, M.</u>, and Marengo, M. (2015). Pulsating Heat pipe Only for Space (PHOS): results of the REXUS 18 sounding rocket campaign. *Journal of Physics: Conference Series*, vol. 655.

Conference proceedings

1. <u>Manzoni, M.</u> and Mameli, M. (2015). Spin Your Thesis! 2013: a Pulsating Heat Pipe on the large diameter centrifuge. *Proc. of the 1st Symposium on space educational activities*, Padova, Italy, 9-12 December 2015.
2. Creatini, F., Bacatti, G., Belfi, F., Cicero, G., Fioriti, D., Di Prizio, D., Piacquadio, S., Guidu, G.M., Orlandini, G., Frigerio, A., Fontanesi, S., Nannipieri, P., Rognini, M., Morganti, N., Filippeschi, S., Di Marco, P., Fanucci, L., Baronti, F., Mameli, M., <u>Manzoni, M.</u>, and Marengo, M. (2015). PHOS experiment: implemantation and test of a large diameter Pulsating Heat Pipe on board REXUS-18. *Proc. of the 1st Symposium on space educational activities*, Padova, Italy, 9-12 December 2015.
3. <u>Manzoni, M.</u>, Mameli, M., de Falco, C., Araneo, L., Filippeschi, S., and Marengo, M. (2015). Numerical simulation of a capillary Pulsating Heat Pipe in various gravity conditions. *Proc. of the 14th UK Heat Transfer Conference*, Edinburgh, UK, 7-8 September 2015.
4. <u>Manzoni, M.</u>, Mameli, M., Andromidas, S., de Falco, C., Araneo, L., Filippeschi, S., Nikas, K-S., and Marengo, M. (2015). Sensitivity analysis of a capillary Pulsating Heat Pipe: influence of the tube characteristics. *Proc. of the 14th UK Heat Transfer Conference*, Edinburgh, UK, 7-8 September 2015.

5. Creatini, F., Guidi, G.M., Belfi, F., Cicero, G., Piacquadio, S., Di Prizio, D., Fioriti, D., Becatti, G., Orlandini, G., Frigerio, A., Fontanesi, S., Nannipieri, P., Rognini, M., Morganti, N., Pasqui, A., Filippeschi, S., Di Marco, P., Fanucci, L., Baronti, F., <u>Manzoni, M.</u>, Mameli, M., and Marengo, M. (2015). Thermal response of a Pulsating Heat Pipe on board the Rexus 18 sounding rocket: PHOS experiment chronicles. *Proc. of the 14th UK Heat Transfer Conference*, Edinburgh, UK, 7-8 September 2015.

6. <u>Manzoni, M.</u>, Mameli, M., DeFalco, C., Araneo, L., Filippeschi, S., and Marengo, M. (2015). Effects of variable accelerations on a PHP-based cooling system, *Proc. of the Vehicle Thermal Management Systems Conference and Exhibition VTMS 12*, Nottingham, UK, 10-13 May2015.

7. <u>Manzoni, M</u>., Mameli, M., DeFalco, C., Araneo, L., Filippeschi, S., and Marengo, M. (2014). Toward a design of a micro pulsating heat pipe. *Proc. of 4th European Conference on Microfluidics*, Limerick, Ireland, 10-12 December 2014.

8. Mameli, M., Marelli, L., <u>Manzoni, M.</u>, Araneo, L., Filippeschi, S., and Marengo, M. (2014). Closed loop pulsating heat pipe: ground and microgravity experiments, *Proc. of 9th International Conference on Two-phase systems for ground ad space applications*, Baltimore, USA, 22-26 September 2014.

9. Mameli, M., <u>Manzoni, M.</u>, Araneo, L., Filippeschi, S., and Marengo, M. (2014) Experimental investigation on a Closed Loop Pulsating Heat Pipe in hyper-gravity conditions, *Proc. of the 15th International Heat Transfer Conference IHTC*, Kyoto, Japan, 10-15 August 2014, DOI: 10.1615/IHTC15.tpa.009100.

10. <u>Manzoni, M.</u>, Mameli, M., DeFalco, C., Araneo, L., Filippeschi, S., and Marengo, M. (2014). Towards a numerical simulation of a closed loop pulsating heat pipe in different gravity levels, *Proc. of the 32nd UIT Conference*, Pisa, Italy, 23-25 June 2014.

List of figures

193

List of tables

Bibliography

[1]   Y. Zhang and A. Faghri, "Advances and unsolved issues in Pulsating Heat Pipes," *Heat Transfer Engineering,* vol. 29, no. 1, pp. 22-44, 2008.

[2]   H. Akachi, "Structure of a heat pipe". USA Patent 4921041. 1990, 1 May 1990.

[3]   H. Akachi, "Structure of micro-heat pipe". USA Patent 5219020. 1993, 15 June 1993.

[4]   M. Mameli, M. Marengo and S. Khandekar, "Local heat transfer measurement and thermo-fluid characterization of a pulsating heat pipe," *International Journal of Thermal Sciences,* vol. 45, pp. 140-152, 2014.

[5]   G. Karimi, "Review and assessment of pulsating heat pipe mechanism for high heat flux electronic cooling," *Thermal and*

Thermomechanical Phenomena in Electronic Systems, vol. 2, pp. 52-59, 2004.

[6] M. Groll and S. Khandekar, "Pulsating Heat Pipes: progress and prospects," in *International Conference on Energy and Environment*, Shanghai, China, 2003.

[7] V. M. Kiseev and K. A. Zolkin, "The influence of acceleration on the performance of oscillating heat pipe," in *Proceedings of 11th International Heat Pipe Conference*, Tokyo, Japan, 1999.

[8] A. A. M. Delil, "Microgravity two-phase flow and heat transfer," Nationaal Lucht- en Ruimtevaartlaboratorium, 1999.

[9] A. A. M. Delil, "Thermal-gravitational modelling and scaling of heat transport systems for applications in different gravity environments: super-gravity levels & oscillating heat transfer devices," ationaal Nationaal Lucht- en Ruimtevaartlaboratorium, 2000.

[10] A. A. M. Delil, "Issues of various two-phase heat transfer devices in gravity environments ranging from micro-gravity to super-gravity," Nationaal Nationaal Lucht- en Ruimtevaartlaboratorium Lucht- en Ruimtevaartlaboratorium, 2000.

[11] J. van Es and A. A. Woering, "High-acceleration performance of the Flat Swinging Heat Pipe," Nationaal Nationaal Lucht- en Ruimtevaartlaboratorium Lucht- en Ruimtevaartlaboratorium, 2000.

[12] A. A. Delil, "Pulsating & oscillating heat transfer devices in acceleration environments from microgravity to supergravity," Nationaal Lucht- en Ruimtevaartlaboratorium, 2001.

[13] M. Kawaji, "Studies of vibration-induced multi-phase fluid phenomena and pulasating heat pipe performance under

microgravity," in *Proceeding of the ASME FEDSM'03 - 4th ASME_JSME Joint Fluids Engineering Conference*, Honolulu, Hawaii, USA, 2003.

[14] J. Gu, M. Kawaji and R. Futamata, "Effects of gravity on the performance of Pulsating Heat Pipes," *Journal of Thermophysics and Heat Transfer,* vol. 18, no. 3, pp. 370-378, 2004.

[15] J. Gu, M. Kawaji and R. Futamaca, "Microgravity performance of micro pulsating heating pipe," *Microgravity Science and Technology,* vol. 16, no. 1, 2005.

[16] K. V. de Paiva, M. B. H. Mantelli, L. K. Slongo and S. J. Burg, "Experimental tests of mini Heat Pipe, Pulsating Heat Pipe and Heat Spreader under microgravity conditions aboard suborbital rockets," in *Proceedings of the 15th International Heat Pipe Conference*, Clemson, South Carolina, USA, 2010.

[17] M. Maeda, A. Okamoto, H. Kawasaki and H. Sugita, "Development of Flat Plate Heat Pipe and the project of on-orbit experiment," in *Proceedings of the 41st International Conference on Environmental Systems*, Portland, Oregon, USA, 2011.

[18] H. Ma, S. M. Thompson, A. A. Hathaway, C. D. Smoot, C. A. Wilson, R. M. Young, L. Greenberg, B. R. Osick, S. van Campen, B. C. Morgan, D. Sharar and N. Jankowski, "Experimental investigation of a Flat-Plate Oscillating Heat Pipe during high-gravity loading," in *Processing of the ASME 2011 International Mechanical Engineering Congress & Exposition IMECE2011-64821*, Denver, Colorado, USA, 2011.

[19] H. Ma, S. M. Thompson, A. A. Hathaway, C. D. Smoot, C. A. Wilson, R. M. Young, L. Greenberg, B. R. Osick, S. van Campen, B. C. Morgan, D. Sharar and N. Jankowski, "Robust thermal performance of a Flat-Plate Pulsating Heat Pipe during high-

gravity loading," *Journal of Heat Transfer,* vol. 133, 2011.

[20] M. Mameli, M. Marengo and S. Zinna, "Numerical investigation of the effects of orientation and gravity in a closed loop pulsating heat pipe," *Microgravity Science and Technology,* vol. 24, no. 2, pp. 79-92, 2012.

[21] V. Ayel, F. Thevenot, Y. Bertin and C. Romestant, "Analyse thermo-hydraulique expérimentale d'un caloduc oscillantsous champ de gravité variable," in *Proceedings of the Congrès Français de Thermique SFT 2013*, Gerardmer, France, 2013.

[22] V. Ayel, L. Araneo, A. Scalambra, M. Mameli, C. Romestant, A. Piteau, M. Marengo, S. Filippeschi and Y. Bertin, "Experimental study of a closed loopflat plate pulsating heat pipe under a varying gravity force," *International Journal of Thermal Sciences,* vol. 96, pp. 23-34, 2015.

[23] D. Mangini, M. Mameli, A. Georgoulas, L. Araneo, S. Filippeschi and M. Marengo, "A pulsating heat pipe for space applications: Ground and microgravity experiments," *International Journal of Thermal Sciences,* vol. 95, pp. 53-63, 2015.

[24] C. Baldassari and M. Marengo, "Flow Boiling in Microchannels and Microgravity," *Progress in Energy and Combustion Science Volume,* vol. 39, no. 1, pp. 1-36, 2013.

[25] P. Charoensawan, S. Khandekar, M. Groll and P. Terdtoon, "Closed Loop Pulsating Heat Pipes - Part A: parametric experimental investigations," *Applied Thermal Engineering,* vol. 23, no. 16, pp. 2009-2020, 2003.

[26] M. Mameli, M. Manzoni, L. Araneo, S. Filippeschi and M. Marengo, "Experimental investigation on a closed loop Pulsating Heat Pipe in hyper-gravity conditions," in *Proceedings of 15th International Heat Transfer Conference IHTC*, Kyoto, Japan, 2014.

[27] M. Mameli, M. Manzoni, L. Araneo, S. Filippeschi and M. Marengo, "Pulsating heat pipe in hyper-gravity conditions," *Heat Pipe Science and Techonology, an International Journal,* vol. ACCEPTED FOR PUBLICATION, 2014.

[28] J. J. W. A. Van Loon, J. Krouse, U. Kunha, J. Goncalves, H. Almeida and P. Schiller, "The Large Diameter Centrifuge, LDC, for life and physical sciences and technology," in *Proceedings of the Life in Space for Life on Earth Symposium*, Angers, France, 2008.

[29] J. Krause, A. Dowson and S. A. Zeugma, "Large Diameter Centrifuge. Experimenter users manual," ESA, 2011.

[30] C. D. Henry, J. Kim and B. Chamberlain, "Heater size and heater aspect ratio effects on sub-cooled Pool boiling heat transfer in low-g," in *Proceedings of the 3rd International Symposium on Two-Phase Flow Modeling and Experimentation*, Pisa, Italy, 2004.

[31] M. Mameli, L. Araneo, S. Filippeschi, L. Marelli, R. Testa and M. Marengo, "Thermal response of a closed loop pulsating heat pipe under variable gravity field," *International Journal of Thermal Sciences,* vol. 80, pp. 11-22, 2014.

[32] M. Mameli, L. Marelli, M. Manzoni, L. Araneo, S. Filippeschi and M. Marengo, "Closed loop pulsating heat pipe: ground and microgravity experiments," in *Proceedings of the 9th International Conference on two-phase systems for ground and space applications*, Baltimore, USA, 2014.

[33] Novespace, "A300 Zero-G Rules and Guidelines, RG-2009-2," France, 2009.

[34] S. Khandekar, M. Schneider and M. Groll, "Mathematical modeling of pulsating heat pipes: state of the art and future challenges," in *Proceedings of 5th ISHMT-ASME- joint International Conference on Heat and Mass Transfer*, Kolkata,

India, 2002.

[35] X. Tang, L. Sha, H. Zhang and Y. Ju, "A review of recent experimental investigations and theoretial analyses for pulasating heat pipes," *Frontiers in Energy,* vol. 7, no. 2, pp. 161-173, 2013.

[36] Y. Miyazaki and H. Akachi, "Heat transfer characteristics of looped capillary heat pipe," in *Proceeding of 5th International Heat Pipe Symposium*, Melbourne, Australia, 1996.

[37] Y. Miyazaki and H. Akachi, "Self excited oscillation of slug flow in a micro channel," in *Proceedings of 3rd International Conference on Multiphase Flow*, Lyon, France, 1998.

[38] M. Hosoda, S. Nishio and R. Shirakashi, "Meandering closed loop heat transport tube (propagation phenomena of vapor plug)," in *Proceedings of 5th ASME/JSME Joint Thermal Engineering Conference*, San Diego, California, USA, 1999.

[39] Z. J. Zuo, M. T. North and L. Ray, "Combined pulsating and capillary heat pipe mechanism for cooling of high heat flux electronics," in *Proceedings of ASME Heat Transfer Device Conference*, Nashville, Tennessee, USA, 1999.

[40] T. N. Wong, B. Y. Tong, S. M. Lim and K. T. Ooi, "Theoretical modeling of Pulsating Heat Pipe," in *Procdings of 11th International Heat Pipe Conference*, Tokyo, Japan, 1999.

[41] R. T. Dobson and T. M. Harms, "Lumped parameter analysis of closed and open oscillatory heat pipes," in *Procddings of 11th International Heat Pipe Conference*, Tokyo, Japan, 1999.

[42] G. Swanepoel, A. B. Taylor and R. T. Dobson, "Theoretical modeling of Pulsating Heat Pipes," in *Proceedings of 6th International Heat Pipe Symposium*, Chiang Mai, Thailand, 2000.

[43] S. Maezawa, F. Sato and k. Gi, "Chaotic dynamics of looped

oscillating heat pipes (theoretical analysis on single loop)," in *Proceedings of 6th International Heat Pipe Symposium*, Chiang Mai, Thailand, 2000.

[44] Z. J. Zuo, M. T. North and K. L. Wert, "High heat flux heat pipes for cooling of electronics," *IEEE Transactions on Components and Packaging Technologies,* vol. 24, no. 2, p. 220–225, 2001.

[45] M. B. Shafii, A. Faghri and Y. Zhang, "Thermal modeling of unlooped and looped pulasating heat pipes," *Journal of Heat Transfer,* vol. 123, pp. 1159-1172, 2001.

[46] M. B. Shafii, A. Faghri and Y. Zhang, "Analysis of heat transfer in unlooped and looped Pulsating Heat Pipes," *International Journal of Numerical Methods for Heat & Fluid Flow,* vol. 12, no. 5, p. 585–609, 2002.

[47] Y. Zhang and A. Faghri, "Heat transfer in a Pulsating Heat Pipe with open end," *International Journal of Heat and Mass Transfer,* vol. 45, p. 755–764, 2002.

[48] S. Khandekar, X. Cui and M. Groll, "Thermal performance modeling of Pulsating Heat Pipes by Artificial Neural Network," in *Proceedings of 12th International Heat Pipe Conference*, Moscow, Russia, 2002.

[49] H. B. Ma, M. R. Maschmann and S. B. Liang, "Heat transport capability in a Pulsating Heat Pipe," *American Institute of Aeronautics and Astronautics (AIAA),* p. 2002–2765, 2002.

[50] Y. Zhang, A. Faghri and M. B. Shafii, "Analysis of liquid-vapor pulsating flow in a U-shaped miniature tube," *International Journal of Heat and Mass Transfer,* vol. 45, p. 2501–2508, 2002.

[51] R. T. Dobson, "An open oscillatory heat pipe steam-powered boat," *International Journal of Mechanical Engineering Education,* vol. 31, no. 4, pp. 339-358 , 2003.

[52] Y. Zhang and A. Faghri, "Oscillatory flow in Pulsating Heat Pipes with arbitrary numbers of turns," *AIAA Journal of Thermophysics and Heat Transfer,* vol. 17, no. 3, p. 755–764, 2003.

[53] P. Sakulchangsatjatai, P. Terdtoon, T. Wongratanaphisan, P. Kamonpet and M. Murakami, "Operation modeling of closed-end and closed-loop oscillating heat pipes at normal operating condition," *Applied Thermal Engineering,* vol. 24, p. 995–1008, 2004.

[54] R. T. Dobson, "Theoretical and experimental modeling of an open oscillatory heat pipe including gravity," *International Journal of Thermal Science ,* vol. 43, p. 113–119, 2004.

[55] S. B. Liang and H. B. Ma, "Oscillating motions of slug flow in capillary tubes," *International Communications in Heat and Mass Transfer,* vol. 31, p. 365–375, 2004.

[56] R. T. Dobson, "An open oscillatory heat pipe water pump," *Applied Thermal Engineering,* vol. 25, p. 603–621, 2005.

[57] B. Holley and A. Faghri, "Analysis of Pulsating Heat Pipe with capillary wick and varying channel diameter," *International Journal of Heat and Mass Transfer,* vol. 48, p. 2635–2651, 2005.

[58] J. S. Kim, Y. B. Im and N. H. Bui, "Numerical analysis of pulsating heat pipe based on separated flow model," *Journal of Mechanical Science and Technology,* vol. 19, no. 9, pp. 1790-1800, 2005.

[59] H. B. Ma, M. A. Hanlon and C. L. Chen, "An investigation of oscillating motions in a miniature Pulsating Heat Pipe," *Journal of Microfluidics and Nanofluidics,* vol. 2, p. 171–179, 2006.

[60] Y. X. Ma and H. Zhang, "Analysis of heat transfer performance of oscillating heat pipes based on a central composite design,"

Chinese Journal of Chemical Engineering, vol. 14, no. 2, p. 223–228, 2006.

[61] S. Khandekar and A. Gupta, "Embedded Pulsating Heat Pipe radiators," in *Proceedings of 14th International Heat Pipe Conference*, Florianopolis, Brazil, 2007.

[62] W. Qu and B. H. Ma, "Theoretical analysis of startup of a pulsating heat pipe," *International Journal of Heat and Mass Transfer,* vol. 50, no. 11-12, p. 2309–2316, 2007.

[63] P. Sakulchangsatjatai, P. Chareonsawan, T. Waowaew, P. Terdtoon and M. Murakami, "Mathematical modeling of closed-end pulsating heat pipes operating with a bottom heat mode," *Heat Transfer Engineering,* vol. 29, no. 3, p. 239–254, 2008.

[64] S. Khandekar and M. Groll, "Roadmap to realistic modeling of closed loop Pulsating Heat Pipes," in *Proceedings of 9th International Heat Pipe Symposium*, Kuala Lumpur, Malaysia, 2008.

[65] R. C. Givler and M. J. Martinez, "Modeling of Pulsating Heat Pipes," Sandia National Laboratories, Albuquerque, New Mexico and Livermore, California, USA, 2009.

[66] Y. X. Song and J. L. Xu, "Chaotic behavior of pulsating heat pipes," *International Journal of Heat and Mass Transfer,* vol. 52, no. 13-14, p. 2932–2941, 2009.

[67] Y. W. Lee and T. L. Chang, "Application of NARX neural networks in thermal dynamics identification of a pulsating heat pipe," *Energy Conversion and Management,* vol. 50, no. 4, p. 1069–1078, 2009.

[68] P. H. Chen, Y. W. Lee and T. L. Chang, "Predicting thermal instability in a closed loop pulsating heat pipe system," *Applied Thermal Engineering,* vol. 29, no. 8-9, p. 1566–1576, 2009.

[69] X. Liu and Y. Hao, "Numerical simulation of vapor-liquid two-phase flow in a closed loop oscillating heat pipe," in *Proceedings of ASME 2009 International Mechanical Engineering Congress & exposition*, Lake Buena Vista, Florida, USA, 2009.

[70] D. Z. Yuan, W. Qu and T. Z. Ma, "Flow and heat transfer of liquid plug and neighboring vapor slugs in a pulsating heat pipe," *International Journal of Heat and Mass Transfer,* vol. 53, no. 7-8, p. 1260–1268, 2010.

[71] S. Das, V. S. Nikolayev, F. Lefèvre, B. Pottier and J. Bonjour, "Thermally induced two-phase oscillating flow inside a capillary tube," *International Journal of Heat and Mass Transfer,* vol. 53, pp. 3905-3913.

[72] V. S. Nikolayev, "A dynamic film model of the pulsating heat pipe," *Journal of Heat Transfer,* vol. 133, no. 8, 2011.

[73] V. A. Hemadri, A. Gupta and S. Khandekar, "Thermal radiators with embedded pulsating heat pipes: infra-red thermography and simulations," *Applied Thermal Engineering,* vol. 31, no. 6-7, pp. 1332-1346, 2011.

[74] M. Mameli, M. Marengo and S. Zinna, "Numerical model of a multi-turn closed loop pulsating heat pipe: effect of the local pressure losses due to meanderings," *International Journal of Heat and Mass Transfer,* vol. 55, pp. 1036-1047, 2012.

[75] M. Mameli, M. Marengo and S. Zinna, "Thermal simulation of a pulsating heat pipe: effects of different liquid properties on a simple geometry," *Heat Transfer Engineering,* vol. 33, pp. 1177-1187, 2012.

[76] D. Xu, T. Chen and Y. Xuan, "Thermo-hydrodynamics analysis of vapor–liquid two-phase flow in theflat-plate pulsating heat pipe," *International Communications in Heat and Mass Transfer,* vol. 39, p. 504–508, 2012.

[77] C. M. Chiang, K. H. Chien, H. M. Chen and C. C. Wang, "Theoretical study of oscillatory phenomena in a horizontal closed-loop pulsating heat pipe with asymmetrical arrayed minichannel," *International Communications in Heat and Mass Transfer,* vol. 39, p. 923–930, 2012.

[78] V. Nikolayev and S. Senthilkumar, "Oscillating menisci and liquid films at evaporation/condensation," in *Proceedings of 17th International Heat Pipe Conference*, Kanpur, India, 2013.

[79] V. Nikolayev, "Oscillatory instability of the gas–liquid meniscus in a capillary under the imposed temperature difference," *International Journal of Heat and Mass Transfer,* vol. 64, p. 313–321, 2013.

[80] M. Dilawar and A. Pattamatta, "A parametric study of oscillatory two-phaseflows in a single turn Pulsating Heat Pipe using a non-isothermal vapor model," *Applied Thermal Engineering,* vol. 51, pp. 1328-1338, 2013.

[81] M. Rao, F. Lefèvre, S. Khandekar and J. Bonjour, "Understanding transport mechanism of a self-sustained thermally driven oscillating two-phase system in a capillary tube," *International Journal of Heat and Mass Transfer,* vol. 65, p. 451–459, 2013.

[82] R. K. Sarangi and M. V. Rane, "Numerical modeling of a Pulsating Heat Piep with heating from the top," *Heat Transfer Research,* vol. 44, no. 6, pp. 535-559, 2013.

[83] R. Senjaya and T. Inoue, "Oscillating heat pipe simulation considering bubble generation Part I: presentation of the model and effects of a bubble generation," *International Journal of Heat and Mass Transfer,* vol. 60, p. 816–824, 2013.

[84] Z. Lin, S. Wang, R. Shirakashi and L. W. Zhang, "Simulation of a miniature oscillating heat pipe in bottom heating mode Simulation of a miniature oscillating heat pipe in bottom

heating mode," *International Journal of Heat and Mass Transfer,* vol. 57, p. 642–656, 2013.

[85] S. Y. Nagwase and P. R. Pachghare, "Experimental and CFD analysis of closed loop Pulsating Heat Pipe with DI-water," in *Proceedings of the International Conference on Energy Efficient Technologies for Sustainability (ICEETS)*, Chunkankadai, India, 2013.

[86] S. Kim, Y. Zhang and J. Choi, "Effects offluctuations of heating and cooling section temperatures on performance of a pulsating heat pipe," *Applied Thermal Engineering,* vol. 58, pp. 42-51, 2013.

[87] G. H. Kwon and S. J. Kim, "Operational characteristics of pulsating heat pipes with a dual-diameter tube," *International Journal of Heat and Mass Transfer,* vol. 75, p. 184–195, 2014.

[88] S. Rudresha and K. Vijee, "CFD analysis and experimental investigation on thermal performance of closed loop Pulsating Heat pipe using different nanofluids," *International Journal of Advanced Research,* vol. 2, no. 8, pp. 753 -760, 2014.

[89] R. Senjaya and T. Inoue, "Effects of non-condensable gas on the performance of oscillating heat pipe, part I: theoretical study," *Applied Thermal Engineering,* vol. 73, no. 1, p. 1387–1392, 2014.

[90] D. Yin, H. Rajab and H. B. Ma, "Theoretical analysis of maximum filling ratio in an oscillating heat pipe," *International Journal of Heat and Mass Transfer,* vol. 74, p. 353–357, 2014.

[91] X. S. Yang, M. Karamanoglu, T. Luan and S. Koziel, "Mathematical modelling and parameter optimization of pulsating heat pipes," *Journal of Computational Science ,* 2014.

[92] M. Mameli, "Pulsating Heat Pipes. Numerical Modeling and

Experimental Assessment," in *PhD Thesis*, 2012.

[93] Y. Miyazaki and M. Arikawa, "Oscillatory flow in the oscillating heat pipe," in *Proceeding of 11th International Heat Pipe Conference*, Tokyo, Japan, 1999.

[94] B. Holley and A. Faghri, "Analysis of pulsating heat pipes with capillary wick and varying channel diameter," *International Journal of Heat and Mass Transfer,* vol. 48, pp. 2635-2651, 2005.

[95] V. S. Nikolayev, "Comment on ''Flow and heat transfer of liquid plug and neighboring vapor slugs in a pulsating heat pipe'' by Yuan, Qu, & Ma," *International Journal of Heat and Mass Transfer,* vol. 54, p. 2226–2227, 2011.

[96] E. W. Lemmon, M. L. Huber and M. O. Mclinden, "NIST standard reference database 23: reference fluid thermodynamic and transport properties-refprop," national institute of standards and technology, standard reference data program, gaithersburg, 2007.

[97] E. Hairer and G. Wanner, Solving Ordinary Differential Equations II. Stiff and Differential-Algebraic Problems, vol. 14, Springer, 1996.

[98] Y. J. Youn, K. Muramatsu, Y. Han and N. Shikazono, "The effect of initial flow velocity on the liquid film thickness in micro tube accelerated slug flow," *International Journal of Multiphase Flow,* vol. 73, p. 108–117, 2015.

[99] N. Chauris, V. Ayel, Y. Bertin and C. Romestant, "Evaporation of a liquid film deposited on a capillary heated tube: experimental analysis by infrared thermography of its thermal footprint," *International Journal of Heat and Mass Transfer,* vol. 86, p. 492–507, 2015.

[100] E. Hairer, C. Lubich and G. Wanner, "Geometric numerical

integration illustrated by the Störmer–Verlet method," *Acta Numerica,* vol. 12, pp. 399-450, 2003.

[101] E. Hairer, G. Wanner and C. Lubich, Geometric Numerical Integration. Structure-Preserving Algorithms for Ordinary Differential Equations, vol. 31, Springer, 2006.

[102] F. P. Incropera and D. P. DeWitt, "Chapter 8: internal flow," in *Fundamentals of Heat and Mass Transfer*, Wiley, 2007, pp. 485-558.

[103] S. Haaland, "Simple and explicit formulas for the friction factor in turbulent flow," *Journal of Fluids Engineering,* vol. 103, pp. 89-90, 1983.

[104] R. Darby, "Correlate pressure drop through fittings," *Chemical Engineering,* vol. 104, pp. 127-130, 2001.

[105] R. K. Shah and A. L. London, "Laminar flow forced convection in ducts," *Advanced in Heat Transfer,* 1978.

[106] P. Aussillous and D. Quere, "Quick deposition of a fluid on the wall of a tube," *Physics of Fluids,* vol. 12, no. 10, pp. 2367-2371, 2000.

[107] Y. Han and N. Shikazono, "Measurement of the liquid film thickness in micro tube slug flow," *International Journal of Heat and Fluid Flow,* vol. 30, p. 842–853, 2009.

[108] V. K. Karthikeyan, K. Ramachandran, B. C. Pillai and B. A. Solomon, "Effect of the number of turns on the temperature pulsations and corresponding thermal performance of pulsating heat pipe," *Journal of Enhanced Heat Transfer,* vol. 20, pp. 443-452, 2013.

[109] S. Sangiamsuk, B. Bubphachot, O. Watanabe and S. Rittidech, "Effects of working fluids, working temperatures and inner diameters on internal pressure and heat transfer rate of a

closed-loop oscillating heat-pipe with check valves (CLOHP/CV)," in *Proceedings of the 2nd TSME International Conference on Mechanical Engineering 2011*, Krabi, Thailandia, 2011.

[110] J. Qu and H. Wu, "Flow visualizzation of silicon-based micro pulsating heat pipes," *Science China Technological Sciences,* vol. 53, pp. 984-990, 2010.

[111] T. Harichian and S. Garimella, "A comprehensive flow regime map for microchannel flow boiling with quantitative transition criteria," *International Journal of Heat and Mass Transfer,* vol. 53, pp. 694-702, 2012.

Nomenclature

Latin symbols

A	Cross flow area, [m²]
A_{ex}	External lateral area, [m²]
A_{wf}	Internal lateral area, [m²]
a	Acceleration, [ms⁻²]
Bo	Bond criterion number, []
c_V	Specific heat constant volume, [Jkg⁻¹K⁻¹]
d_{in}	Diameter, [m]
f_τ	Friction coefficient, []
g	Gravity acceleration, [ms⁻²]
H	Enthalpy, [J]
h	Specific enthalpy, [J]
htc	Convection coefficient, [Wm⁻²K⁻¹]
h_{LV}	Latent heat of vaporization, [Jkg⁻¹]
K_{Re}, K_d, K_r	Darby 3K coefficients, []

Nomenclature

k	Thermal conductivity, [Wm^{-1}K^{-1}]
k_{eq}	Equivalent thermal conductivity, [Wm^{-1}K^{-1}]
L	Length, [m]
L_x	Thermal entry length, [m]
m	Mass, [kg]
$\dot{m}$	Mass flux, [kg/s]
m_{LV}	Evaporated/Condensed mass, [kg]
N	Number of elements, []
P	Pressure, [Pa]
Pr	Prandtl, []
Q	Heat power, [W]
q_{ex}	External heat flux, [Wm^{-2}]
q_{wf}	Heat flux between wall and fluid, [Wm^{-2}]
R^*	Gas constant, [Jkg^{-1}K^{-1}]
Ra	Rayleigh number, []
Re	Reynolds number, []
R_{eq}	Equivalent thermal resistance, [KW^{-1}]
r_{ex}	External Radius, [m]
S	Entropy, [JK^{-1}]
T	Temperature, [K]
t	Time, [s]
U	Internal energy, [J]
u	Specific internal energy, [Jkg^{-1}]
V	Volume, [m^3]
w	Velocity, [ms^{-1}]
x	Axial coordinates, [m]
y	Axial coordinates, [m]

Greek symbols

Δt	Time step, [s]
δ	Film thickness, [m]

ε Surface roughness, [m]

ϑ Inclination between gravity and flow path,

μ Chemical potential, [Jmol^{-1}]

ρ Density, [kgm^{-3}]

σ Surface tension, [Pa s]

Subscripts

f Fluid

l Liquid

sat Saturated conditions

v Vapor

w Wall

∞ Environmental

Acronyms

ANN   Artificial Neural Network

CFD   Computational Fluid Dynamics

CV   Control Volume

DAQ   Data Acquisition System

ESA   European Space Agency

ESTEC   European Space Research and Technology

FFT   Fast Fourier Transform

HTC   Heat Transfer Coefficient

I/O   Inner/Outer

ISS   International Space Station

JAXA   Japan Aerospace Exploration Agency

LDC   Large Diameter Centrifuge

LS   Liquid Slug or Slice

PEEK   PolyEtherEtherKetone

PET   PolyEthylene Terephthalate

Nomenclature

PHP   Pulsating Heat Pipe
TRL   Technological Readiness Level
VOF   Volume of Fluid
VP   Vapor Plug